Multi-Objective Particle Swarm Optimization for the Structural Design of Concentric Tube Continuum Robots for Medical Applications

Dipl.-Ing. Josephine Granna

2019

KURZFASSUNG

Tubuläre Kontinuumsroboter gehören zur Familie der Roboter, deren tangentiale Krümmungsvektoren eine kontinuierliche Kurve beschreiben. Sie bestehen aus mehreren ineinander verschachtelten Röhrchen und zeichnen sich durch ihre inhärente Flexibilität aus. Durch die Ausstattung mit Werkzeugen am distalen Ende sind sie prädestiniert für den Einsatz in der minimal invasiven Chirurgie. Aufgrund ihres morphologischen Aufbaus ist es ihnen zudem möglich in Bereiche im Körper vorzudringen, die mit kommerziellen Werkzeugen nicht zugänglich sind oder große Schnitte erfordern. Darüber hinaus können sie durch kleine Öffnungen inseriert werden oder nichtlinearen Pfaden folgen.

Um den Einsatz dieser Roboter in der Medizin zu ermöglichen, wurden in den letzten Jahren grundlegende Forschungsansätze entwickelt. Es bestehen jedoch noch immer Herausforderungen, die gelöst werden müssen. Eine davon ist die Struktursynthese von tubulären Kontinuumsrobotern, welche nicht trivial ist, da sich diese Roboter durch einen großen Parameterraum auszeichnen. Dies ist einerseits von Vorteil, da sie patientenübergreifend und für unterschiedliche Anwendungen eingesetzt werden können. Andererseits ist die Komposition der Röhrchen und ihr Design komplex und erfordert Wissen über Anatomie und Strukturverhalten. Vor dem Einsatz solcher Roboter muss die Zusammensetzung der Röhrchen (d.h. die Auswahl von Designparametern und anwendungsspezifischen Einschränkungen) gelöst werden, deren Design anwendungs- und patientenspezifisch ist. Kinematische Modelle, die die Morphologie und Bewegung der Roboter beschreiben, erhöhen die Komplexität dieser Synthese, da ihre mathematische Beschreibung nicht linear ist.

Stand der Forschung ist daher die strukturelle Maßsynthese von tubulären Kontinuumsrobotern. Die Anwendung von Optimierungsalgorithmen ermöglicht die Designkonzeptionierung für ein bestimmtes Anwendungsszenario oder einen Patientendatensatz. Bestehende Ansätze berücksichtigen jedoch nicht den gesamten Parameterraum, können nicht mit der Nichtlinearität des Modells umgehen oder mehrere Zielfunktionen gleichzeitig berücksichtigen (wobei die meisten medizinischen Anwendungen und Aufgaben durch multiple Zielfunktionen definiert sind).

Ziel dieser Arbeit ist es, diese grundlegende Herausforderung zu lösen, indem das Problem der Parameteroptimierung durch die Anwendung eines multiplen Optimierungsalgorithmus gelöst wird. Das Hauptaugenmerk dieser Arbeit liegt auf einer allgemeinen Methode zur Lösung des patienten- und anwendungsspezifischen Designs der tubulären Kontinuumsroboter. Die vorgeschlagene Methode basiert auf der Anwendung von evolutionären Algorithmen, die mehrere konkurrierende Zielfunktionen berücksichtigen können, wobei der zu optimierende Parametersatz eine variable Länge aufweisen kann. Globale Optimierungsalgorithmen zielen speziell auf den beschränkten Suchraum von tubulären Kontinuumsrobotern ab. Eine nicht lineare Optimierung ermöglicht die Einbindung des Elastizitätsmodells zur kinematischen Modellierung.

Der hier vorgeschlagene Optimierungsansatz wird anhand unterschiedlicher Anwendungen evaluiert. Dies beinhaltet die Kooperation zweier Roboterarme, die strukturelle Steifigkeitsoptimierung unter Berücksichtigung von Arbeitsraumbeschränkungen und externen Kräften, und die laser-induzierte Thermoablation zur Entfernung von Tumoren im Gehirn.

Die wissenschaftlichen Beiträge dieser Arbeit sind 1) die Entwicklung eines Optimierungsansatzes, der die wichtigsten Parameter, Zielfunktionen und Beschränkungen im Hinblick auf die Auslegung der tubulären Kontinuumsroboter beschreibt, 2) die Auswahl eines geeigneten Optimierungsalgorithmus, der den multidimensionalen Suchraum und mehrere Zielfunktionen berücksichtigt und 3) die Bewertung des vorgeschlagenen Optimierungsansatzes, sowie strukturelle Synthese auf der Grundlage von drei realen Anwendungen.

Schlagwörter: Tubuläre Kontinuumsroboter, Designoptimierung, Minimal-invasive Chirurgie

ABSTRACT

Concentric tube robots belong to the class of continuum robotic systems whose morphology is described by continuous tangent curvature vectors. They are composed of multiple, interacting tubes nested inside one another and are characterized by their inherent flexibility. Concentric tube continuum robots equipped with tools at their distal end have high potential in minimally invasive surgery. Their morphology enables them to reach sites within the body that are inaccessible with commercial tools or that require large incisions. Further, they can be deployed through a tight lumen or follow a nonlinear path.

Fundamental research has been the focus during the last years bringing them closer to the operating room. However, there remain challenges that require attention. The structural synthesis of concentric tube continuum robots is one of these challenges, as these types of robots are characterized by their large parameter space. On the one hand, this is advantageous, as they can be deployed in different patients, anatomies, or medical applications. On the other hand, the composition of the tubes and their design is not a straightforward task but one that requires intensive knowledge of anatomy and structural behavior. Prior to the utilization of such robots, the composition of tubes (i.e. the selection of design parameters and application-specific constraints) must be solved to determine a robotic design that is specifically targeted towards an application or patient. Kinematic models that describe the change in morphology and complex motion increase the complexity of this synthesis, as their mathematical description is highly nonlinear.

Thus, the state of the art is concerned with the structural design of these types of robots and proposes optimization algorithms to solve for a composition of tubes for a specific patient case or application. However, existing approaches do not consider the overall parameter space, cannot handle the nonlinearity of the model, or multiple objectives that describe most medical applications and tasks.

This work aims to solve these fundamental challenges by solving the parameter optimization problem by utilizing a multi-objective optimization algorithm. The main concern of this thesis is the general methodology to solve for patient- and application-specific design of concentric tube continuum robots and presents key parameters, objectives, and constraints. The proposed optimization method is based on evolutionary concepts that can handle multiple objectives, where the set of parameters is represented by a decision vector that can be of variable dimension in multidimensional space. Global optimization algorithms specifically target the constrained search space of concentric tube continuum robots and nonlinear optimization enables to handle the highly nonlinear elasticity modeling.

The proposed methodology is then evaluated based on three examples that include cooperative task deployment of two robotic arms, structural stiffness optimization under the consideration of workspace constraints and external forces, and laser-induced thermal therapy in the brain using a concentric tube continuum robot.

In summary, the main contributions are 1) the development of an optimization methodology that describes the key parameters, objectives, and constraints of the parameter optimization problem of concentric tube continuum robots, 2) the selection of an appropriate optimization algorithm that can handle the multidimensional search space and diversity of the optimization problem with multiple objectives, and 3) the evaluation of the proposed optimization methodology and structural synthesis based on three real applications.

Keywords: concentric tube continuum robots, design optimization, minimally invasive surgery

PUBLICATIONS

The following publications emerged in the scope of this doctoral thesis:

Granna, J., M. T. Chikhaoui, J. Starke, and J. Burgner-Kahrs (2018). "Towards Motion Coordination Control and Design Optimization for Dual-Arm Concentric Tube Continuum Robots." In: *IEEE Robotics and Automation Letters* 3.3, pp. 1793–1800.

Granna, J., I. S. Godage, R. Wirz, K. D. Weaver, R. J. Webster III, and J. Burgner-Kahrs (2016). "A 3-D Volume Coverage Path Planning Algorithm with Application to Intracerebral Hemorrhage Evacuation." In: *IEEE Robotics and Automation Letters* 1.2, pp. 876–883.

Granna, J., Y. Guo, K. D. Weaver, and J. Burgner-Kahrs (2017). "Comparison of Optimization Algorithms for a Tubular Aspiration Robot for Maximum Coverage in Intracerebral Hemorrhage Evacuation." In: *Journal of Medical Robotics Research* 02.01, p. 1750004.

Granna, J., A. Nabavi, and J. Burgner-Kahrs (2017). "Toward Computer-Assisted Planning for Interstitial Laser Ablation of Malignant Brain Tumors using a Tubular Continuum Robot." In: *International Conference on Medical Image Computing and Computer Assisted Intervention*. Part II, LNCS 10434, pp. 557–565.

Granna, J., A. Nabavi, and J. Burgner-Kahrs (2019). "Computer-Assisted Planning for a Concentric Tube Robotic System in Neurosurgery." In: *International Journal of Computer Assisted Radiology and Surgery* 14.2, pp. 335–344.

CONTENTS

NOMENCLATURE

ABBREVIATIONS

CTCR	concentric tube continuum robots
DOF	degrees of freedom
LITT	laser-induced thermal therapy
MOPSO	multi-objective particle swarm optimization
NiTi	nickel titanium
NSGA	non-dominated sorting genetic algorithm
NSGA-II	fast and elitist multi-objective genetic algorithm
PCL	polycaprolactone
PLA	polylactide
PSO	particle swarm optimization
SPEA	strength Pareto evolutionary algorithm
SPEA2	improved strength Pareto evolutionary algorithm

LIST OF SYMBOLS

Concentric Tube Continuum Robots

n	number of tubes
i	tube index
A	area of cross section
E	elastic modulus
G	shear modulus
I	moment of inertia
ϵ	recoverable strain rate
ν	Poissons's ratio
G	shear modulus
κ	tube curvature
ℓ	tube length
ℓ_s	straight section length of tube
ℓ_c	curved section length of tube
OD	outer tube diameter
ID	inner tube diameter
β	translational actuation parameter
α	rotational actuation parameter
$\mathbf{q}$	configuration
Q	configuration space

Cosserat Rod Theory

s	arc length
$\mathbf{g}^*(s)$	initial reference state
$\mathbf{g}(s)$	final state
$\mathbf{F}$	external forces
$\mathbf{L}$	external loads
$\mathbf{n}$	internal forces
$\mathbf{m}$	internal moments
w	global coordinate frame
b	body coordinate frame of tube i
B	body coordinate frame of tube $i = 1$
$\mathbf{R}$	orientation of frame
$\mathbf{r}$	position of frame
ϑ	linear strains
υ	angular strains
θ	rotation angle about local z-axis
$\mathbf{K}$	stiffness matrix
$\mathbf{K}_v$	linear stiffness matrix
$\mathbf{K}_u$	angular stiffness matrix
I_{xx}	second moment of area about x-axis
I_{yy}	second moment of area about y-axis
I_{zz}	polar moment of inertia
$\mathcal{T}$	set of transition points

Optimization Problem

$f(\mathbf{x})$	objective function
$\mathbf{x}$	decision vector
$\mathbf{y}$	objective vector
m	number of decision variables
o	number of objectives
ρ	user defined neighborhood
$g(x)$	equality constraint functions
$h(x)$	inequality constraint functions
$\mathcal{X}$	decision space
$\mathcal{Y}$	objective space
X_f	feasible region
$\mathcal{P}_s$	Pareto optimal set
$\mathcal{P}_f$	Pareto front

Particle Swarm Optimization

t	current generation
T	number of generations

P	number of particles
k	particle index
m	particle component
x_k	particle position
v_k	particle velocity
p_{b_k}	personal best leader
g_b	global best leader
η	inertia coefficient
c_1, c_2	constants
r_1, r_2	random numbers
y	particle cost
A_t	archive
u_b	upper boundary of particle
l_b	lower boundary of particle
N_m	particle's own dimension
N_{m_g}	leader's dimension
λ	aggregation weights

Parameter Optimization Methodology

G_S	surface dataset
G_V	voxelized grid
v_s	voxel size
a	surface data point
c	centroid of surface dataset
o_V	origin of voxelized grid
h	trajectory
o	insertion point
${}_E T^B$	transformation matrix
δ	safety margin
m_s	sampling size
W_R	reachable workspace
W_V	workspace volume
e	end-effector position
p_i	points along backbone
$v_{\text{unreachable}}$	number of unreachable voxels
$v_{\text{reachable}}$	number of reachable voxels
φ	orientation angle
r_z	tangent curvature vector

Applications

Cooperative Task Deployment

S	endoscopic shift distance
$\mathbf{q}_{A,B}$	configuration of robot A and B
$n_{\mathbf{q}_{A,B}}$	number of collaborative configurations
$\mathbf{r}_{z_{A,B}}$	tangent curvature vectors of robot A and B
d_E	Euclidean end-effector distance between robot A and B

Structural Stiffness and Workspace Optimization

Ω	gripper opening angle
$\mathbf{F}$	manipulation forces
c	tube clearance

Laser-Induced Thermal Therapy

γ	extended tube lengths
n_a	number of ablation objects
s_a	size of ablation object
p_a	center point of ablation object
d	number of sequentially used tubes

INTRODUCTION

1.1 CONCENTRIC TUBE CONTINUUM ROBOTS

Concentric tube continuum robots (CTCR) are a subclass of continuum robots whose morphology is described by continuous tangent vectors. CTCR are also referred to as active cannulas or tubular continuum robots in the literature (Burgner-Kahrs, Rucker, and Choset, 2015). They were first introduced by (Sears and P. Dupont, 2006; Webster III, Okamura, and Cowan, 2006) in 2006. CTCR are composed of multiple, precurved elastic tubes (with the number of tubes ⩾ 2) with different length inserted into one another, as depicted in Figure 1. Each tube is actuated through translation and rotation at its base. Elastic interaction of the tubes generates a tentacle-like motion that enables their manipulability. NiTi (nickel-titanium) shape memory alloys represent the most commonly proposed tube material, but also 3D printed thermoplastic materials like PLA (polylactide), PCL (polycaprolactone), and nylon are mentioned in the literature (Amanov, Nguyen, and Burgner-Kahrs, 2015; Morimoto and Okamura, 2016; Webster III, Okamura, and Cowan, 2006).

Due to their small size with diameters usually less than 2 mm and compliant structure, they have been proposed for various medical applications to be utilized as an actuatable needle. These include endonasal surgery (Burgner, Gilbert, and Webster III, 2013), neurosurgery (Anor, Madsen, and Dupont, 2011; Bedell et al., 2011; Bergeles, Gosline, et al., 2015; Boushaki et al., 2016), intracerebral hemorrhage evacuation (Burgner, Swaney, Lathrop, et al., 2013; Godage et al., 2015), intracardiac surgery (Bergeles, Gosline, et al., 2015), bronchoscopy (Kuntz, Torres, et al., 2015; Torres, Webster III, and Alterovitz, 2012), laser prostate surgery (Hendrick, Herrell, and Webster III, 2014), cochlear implant insertion (Granna, Rau, et al., 2016), and transforamenal hippocampotomy (Comber et al., 2016; Gilbert, Neimat, and Webster III, 2015).

Figure 1: Concentric tube continuum robot composed out of three tubes (reprinted from (Gilbert, Neimat, and Webster III, 2015), © 2015 IEEE)

The CTCR could either be employed as an autonomous device or be teleoperated by the surgeon as a master-slave system. Natural orifices or small incisions can be used to deploy the robot into the human body. Depending on the application, the CTCR could be equipped with tools, for instance with a gripper, needle, camera, or laser fiber. The tools can be inserted through the inner lumen of the robot. The CTCR could also be utilized as a surgical device to be deployed through an endoscope. Multiple CTCR arms working collaboratively on a medical task are proposed by (Hendrick, Herrell, Mitchell, et al., 2016; Hendrick, Herrell, and Webster III, 2014; Hendrick, Mitchell, et al., 2015).

The fields of research for CTCR include design, modeling, control, and planning. The design of CTCR considers the selection of materials or structural design of tubes, the design of the actuation unit, and fabrication aspects (Gilbert, Rucker, and Webster III, 2016).

Different models to determine the forward kinematics have been proposed. Early research considered the use of simple geometry and constant curvature arcs to compute the three-dimensional curve of the robot (Rucker and Webster III, 2008). The most recent model utilizes elasticity theory and models the robot as a collection of continuous slender beams undergoing bending and torsion. Shear and axial extension are assumed to have little effect on the bending behavior, such that they are neglected thus far. The model also accounts for external loads (forces and moments) (Rucker, Jones, and Webster III, 2010a). The kinematics for two tubes with constant circular precurvature can be solved analytically - other tube designs require to solve a set of differential equations numerically (Lock et al., 2010; Rucker, Jones, and Webster III, 2010a). The inverse kinematics approaches the forward kinematics numerically (Leibrandt, Bergeles, and Yang, 2015) and utilizes, for instance, an inverse Jacobian approach (Sears and P. E. Dupont, 2007), or considers the use of machine learning concepts (Grassmann, Modes, and Burgner-Kahrs, 2018). Further modeling regards the occurrence of instable configurations that are described by a sudden release of energy that builds up due to the rotational difference and friction between the tubes, so-called snapping (Gilbert, Hendrick, and Webster III, 2016; Ha, Park, and Dupont, 2016; Hendrick, Gilbert, and Webster III, 2015a; Webster III, Romano, and Cowan, 2009; R. Xu, Atashzar, and Patel, 2014).

So far, CTCR's kinematic control concentrated mainly on teleoperation, where a device is utilized to position the robot. Teleoperation also deals with human-machine interaction concepts that investigate user-friendly input devices and control algorithms. Further, optimal kinematic control includes the consideration of shape sensing to receive information about the actual position and orientation of the robot's tip but also other points along the backbone. Additionally, force sensing is required to measure external loads that might occur during deployment (Gilbert, Rucker, and Webster III, 2016).

Another important research field deals with planning concepts. These include motion and trajectory planning approaches to deploy the robot along a tortuous path or around obstacles and the trajectory or motion strategy between adjacent configurations of the robot (Gilbert, Rucker, and Webster III, 2016). Follow-the-leader behavior is an important aspect, which describes a specific motion of a robot where the over-

all backbone follows the path of the tip. This type of motion is required for some minimally invasive applications (Gilbert, Neimat, and Webster III, 2015).

CTCR represent the smallest continuum robot existing thus far and promise to improve minimally invasive surgery considering the diverse set of applications and employed medical tools mentioned in the state of the art. They have potential over various other treatment options, as they can maneuver through tight space and lumen on nonlinear trajectories, which are not accessible with commercially existing tools or robotic designs. However, there still exist fundamental challenges that require attention to finally advance CTCR to their full potential. Addressing these challenges could bring them closer to be finally used as a commercial product in medicine. One of these challenges is their structural design synthesis, which is further detailed in the following.

1.2 OVERVIEW FOR DESIGN OPTIMIZATION OF CTCR

CTCR can only reach their full potential in minimally invasive surgery if the design of the tubes adapts to the specific application, patient, or task. This design process is not one to solve straight forward, as the design parameter space for CTCR is large, such that there exist infinite options. It further requires a priori knowledge about the anatomical constraints and medical conditions, which demands medical image analysis and prior definition of task requirements.

To employ a CTCR for a medical application, design- and application-specific parameters must be selected a priori. The parameter space of CTCR is diverse, as each tube is characterized by certain geometric and material parameters. Geometric parameters are the tube curvature, the outer and inner diameter, and the straight and curved section length that define the overall length of each tube. The material is chosen to be superelastic, which is defined by an elastic modulus, the recoverable strain rate, the Poisson's ratio, and the shear modulus.

Selecting the design parameters manually is not possible, as the tube interaction and the morphology of the robot is only predictable for simple designs. Thus, researchers proposed the use of optimization algorithms to design CTCR for a medical application or task. Existing design optimization algorithms consider the optimization of the tube's lengths and curvatures (Bedell et al., 2011), and consider task or anatomical constraints to maximize a set of reachable points (Bergeles, Gosline, et al., 2015). In (Burgner, Gilbert, and Webster III, 2013), the authors use a different approach and incorporate volume-based objectives to optimize the tube's curvature. (Torres, Webster III, and Alterovitz, 2012) and (Baykal, Bowen, and Alterovitz, 2018) investigate design optimization together with motion planning to compute a feasible path towards the goal. Using a global optimization method, the authors optimize tube lengths and curvatures to maximize the reachable space (Baykal, Bowen, and Alterovitz, 2018). In (Gilbert, Neimat, and Webster III, 2015), the authors first study the use of helically shaped tubes to optimize for follow-the-leader motion to enable the robot to follow a predefined path. Multiple objectives are considered by (Boushaki et al., 2016) to maximize reachability and stability at the same time and include the computation of optimal tube curvatures and lengths.

1.3   CHALLENGES AND RESEARCH QUESTIONS

The parameter optimization of CTCR for a specific application or task remains still a challenge. Design optimization algorithms for CTCR have been proposed for various applications. A design optimization algorithm that applies to different scenarios and patients is challenging, as each problem is defined by specific in- and outputs, parameters, constraints, and objective functions.

Most optimization algorithms that were proposed in the early stages of CTCR used simplified kinematic models. Recent kinematic models require solving highly nonlinear functions (Cosserat rod theory), which constrains the space of applicable optimization algorithms. Further, existing algorithms are still restricted to only a few parameters, where most consider tube curvature and curved length. Especially the consideration of stiffness and material properties is an important aspect, as these parameters influence the robot's ability to withstand or apply external forces and loads during a medical task. They are thus essential for manipulation tasks and have not been considered in the state of the art so far.

Considering other robotic optimization algorithms' state of the art, it is noticeable that various researchers utilized global optimization algorithms. These are mostly heuristic approaches but are especially suited for complex optimization problems with various design parameters and have better performance. As the design space is multidimensional and multimodal, a global optimization algorithm seems suitable for the structural design of CTCR. The parameter space of CTCR has many constraints - especially when the number of optimization parameters increases. Local optimization algorithms are prone to remain stuck in local minima, whereas global (heuristic-based) approaches are more likely to find a global optimum.

Another important aspect of the design optimization procedure is the consideration of conflicting objectives. Looking at optimization strategies for other robots, multi-objective optimization algorithms have been employed for various robot types. Optimization procedures for CTCR mostly considered scalar error metrics or the sum of weighted objectives. This results in problems, as the selection of these weights is not straightforward. However, as objectives tend to be represented by different units, their appropriate selection is essential. Changing these weights influences the outcome of the optimization procedure dramatically and might result in different solutions. The consideration and handling of heterogeneous objectives (represented by different units) is not covered by the state of the art.

To conclude, an optimization framework that utilizes a global optimization approach, which considers the overall parameter space, and handles the combination of multiple heterogeneous and conflicting objectives is unexploited by the state of the art.

1.4 DISSERTATION CONTRIBUTIONS

This thesis seeks to answer the following key questions.

> How can the optimization problem or framework
>
> 1. be **classified** and formulated to handle **different problems** or **patients**?
>
> 2. handle the **overall parameter space** (including length, diameter, wall thickness, curvature, and elasticity of the tubes) and the **nonlinearity** of the kinematic model?
>
> 3. consider **multiple heterogeneous** and **conflicting objectives**?

This thesis classifies the optimization problem of CTCR and formulates the design optimization problem to handle patient-specific image data as input to the algorithm to optimize for patient-individual tubes. Another aim is the formulation of key objective functions that occur in various medical applications and are inspired by the state of the art and the applicability of CTCR to minimally invasive surgery.

This work hypothesizes that evolutionary optimization algorithms and particularly swarm intelligence could be an efficient method to cope with the structural design optimization of CTCR. Especially, multi-objective particle swarm optimization is investigated in the scope of this thesis. The applicability of such a global evolutionary optimization algorithm that considers multiple objectives is currently unexploited by the state of the art. The assumption here is that particle swarm optimization has the potential to handle multimodal problems (with many parameters and constraints) and can especially account for multiple conflicting objective functions. Further, it can handle the nonlinearity of the model.

The proposed algorithm is formulated to consider the overall set of design parameters (number of tubes, material, length, diameters, wall-thickness, curvatures) including the material's elasticity and stiffness. The multi-objective particle swarm optimization algorithm is then evaluated based on three applications, which are the cooperative task deployment of two robotic arms, the structural stiffness optimization under the consideration of workspace constraints and external forces, and laser-induced thermal therapy in the brain.

> In summary, this thesis aims to **classify** the **optimization problem** for CTCR and proposes an optimization strategy that can handle multiple conflicting objective functions. The proposed optimization method includes the **overall parameter** and **configuration space**. This work specifically investigates the applicability of **multi-objective particle swarm optimization**, which is evaluated based on three problems.

1.5 OUTLINE

1.5.1 *Part I: State of the Art*

Chapter 2 presents the fundamentals of concentric tube continuum robots and introduces their design space, actuation principles, and modeling. The modeling part of this chapter is concerned with the forward kinematics of the CTCR that allows the determination of the three-dimensional space curve (pose of the robot) depending on the specific configuration. The forward kinematics represents a key aspect in parameter optimization of CTCR as it can be utilized to determine the workspace of a specific design. This thesis applies Cosserat rod theory, where each tube of the CTCR is assumed to be a slender beam undergoing bending and torsion.

As the aim of this thesis is to apply numerical optimization to the design problem of CTCR, chapter 3 introduces the general definition of an optimization problem and gives an overview of evolutionary algorithms. Particle swarm optimization is particularly presented in this chapter, as this algorithm presents the basis of this work. Further, multi-objective optimization and the extensibility of particle swarm optimization towards multi-objective problems are discussed.

The focus in chapter 4 is the state of the art for optimization algorithms in the area of robotics and their application to design optimization problems. Here, prominent design parameters and objectives are presented, as well as single- and multi-objective optimization strategies. Specifically, the state of the art for design optimization of CTCR is regarded in this chapter and existing parameters and objectives are identified. Lastly, this chapter discusses existing optimization algorithms for CTCR and concludes with the challenges in parameter optimization of this work.

1.5.2 *Part II: Methods*

Chapter 5 presents the parameter optimization methodology for CTCR, which is the basis of this thesis. It formulates and defines key parameters, objectives, and constraints of optimization problems for CTCR. It further introduces the implementation of the multi-objective particle swarm optimization algorithm specifically targeted towards the structural design optimization of CTCR.

1.5.3 *Part III: Applications*

The following chapters investigate the applicability of the presented algorithm regarding three problems. These define novel applications for the use of CTCR in minimally invasive surgery.

The first application (chapter 6) compares the applicability of a single-objective particle swarm optimization algorithm to the performance of the Nelder-Mead algorithm inspired by the state of the art. The application deals with the optimization of cooperative robots to allow for simultaneous deployment of multiple tasks.

The second application (chapter 7) deals with the structural stiffness optimization of CTCR. It considers the overall parameter space for a three-tube CTCR and includes external forces, as well as multiple objectives.

The third application (chapter 8) applies the parameter optimization methodology to laser-induced thermal therapy in the brain utilizing a CTCR. It accounts for multiple objectives and considers application-specific parameters (bin packing problem) in the optimization procedure to show the extensibility of the algorithm.

The last chapter concludes this thesis and reports scientific findings and the underlying contribution of this work.

Part I

STATE OF THE ART

2

FUNDAMENTALS OF CONCENTRIC TUBE CONTINUUM ROBOTS

This chapter presents the fundamentals for CTCR, which include their design, actuation principles as well as kinematic modeling. The design principles present the material and geometric tube parameters, and the actuation principles describe the configuration space of the robot. Further, this chapter presents the forward kinematic modeling for CTCR, where the theory of elastic rods is applied. This includes Cosserat, and specifically Kirchhoff rod theory, which is utilized to model the CTCR as a composition of slender rods undergoing bending and torsion. It further considers the robot to be subject to external forces and loads.

2.1 DESIGN AND CONFIGURATION SPACE

CTCR are composed out of n ($n \geqslant 2$), precurved superelastic tubes, which are inserted into one another. Each tube is mechanically actuated by translation and rotation and is fixed in an actuation unit at its base. The morphology of the robot thus represents a curve in three-dimensional space (Burgner-Kahrs, Rucker, and Choset, 2015).

2.1.1 *Design Principles*

Each tube i is characterized by certain material and geometric parameters. The material is chosen to be superelastic and is defined by an elastic modulus E, the recoverable strain rate ϵ, the Poisson's ratio ν, and the shear modulus G.

Geometric parameters are the curvature κ, and the straight and curved section length ℓ_{s_i} and ℓ_{c_i}, respectively. The overall length of a tube is $\ell_i = \ell_{s_i} + \ell_{c_i}$ where $\ell_1 > ... > \ell_n$ with $i = 1$ being the innermost tube, see Figure 2. Note, that also tubes with non-constant curvature would be conceivable. However, this work focuses on tubes with a straight and a curved section with constant curvature.
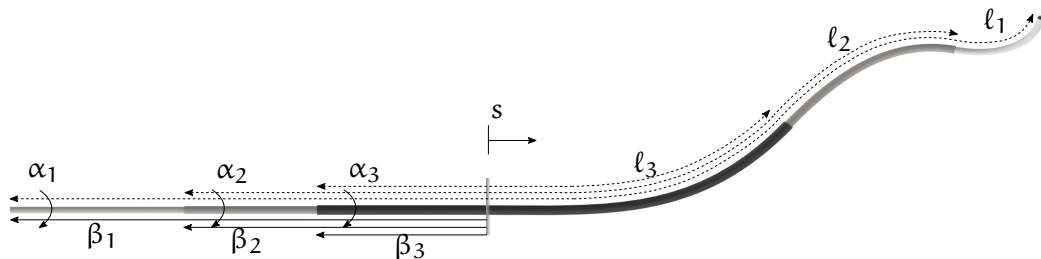
Figure 2: Concentric tube robot composed of three tubes with tube length ℓ_1, ℓ_2, ℓ_3, translational parameters $\beta_1, \beta_2, \beta_3$, and rotational parameters $\alpha_1, \alpha_2, \alpha_3$.

The outer OD_i and inner diameter ID_i of each tube are parameters that define the wall thickness and influence the stiffness and the moment of inertia I of the tubes. Further, the outer diameter constrains the maximum curvature of a tube i as (Webster III, Romano, and Cowan, 2009).

$$\kappa_{i_{max}} = \frac{2\epsilon_i}{OD_i(1 + \epsilon_i)},$$

where ϵ_i defines the strain. This equation describes the relation between material strain limit and plastic deformation of a tube.

2.1.2 *Actuation Principles*

The actuation space of each tube i is defined by the translational parameters $\beta_i \in [-\ell_i, 0]$ and the rotational parameters $\alpha_i \in [-\pi, \pi)$, as illustrated in Figure 2. The configuration space Q of CTCR is thus of dimension 2n with $\mathbf{q} = [\alpha_1, ..., \alpha_n, \beta_1, ..., \beta_n]^{\mathsf{T}}$, which are subject to the following inequalities

$$\beta_1 \leqslant ... \leqslant \beta_n \leqslant 0,$$

$$\ell_n + \beta_n \leqslant ... \leqslant \ell_1 + \beta_1.$$

These constraints arise, as the tip of an inner tube is not supposed to be retracted into an outer tube. Note, that β_i is negative, as it defines the length from the constrained outlet towards the end of a tube.

2.2 MODELING

CTCR can be modeled as slender rods (where their length is assumed to be much longer than their diameter) using elastic rod theory. The elastic Cosserat rod theory describes the deformation of a rod and is an extension to classical beam theory, see (Antman, 2005). It was originally developed by Eugène and Françoise Cosserat in 1907. Cosserat rod theory enables to describe the deformation of the tubes, as well as their torsion against one another (Lock et al., 2010; Rucker, Jones, and Webster III, 2010a). The adapted forward kinematics model for CTCR based on Cosserat rod theory presented here is based on the work by (Rucker, Jones, and Webster III, 2010a).

2.2.1 *Cosserat Rod Model*

General Cosserat rod theory considers a rod to undergo **bending**, **torsion**, **extension**, and **transverse shear**. Considering a CTCR, the theory assumes that friction has only little effect on the bending behavior of the tube and is not considered. In Cosserat rod theory, a set of differential equations describes the rod's deformation. This set of differential equations consists of 1) kinematic equations, 2) equilibrium equations, and 3) constitutive equations.

Consider a single tube i to be a slender Cosserat rod, which is subject to external loads. An external load can be defined by forces, as well as moments. A set of differential Cosserat rod equations can be derived to describe the deformation of a rod

through external loads from an initial, undeformed state $\mathbf{g}_i^*(s)$ to its deformed state $\mathbf{g}_i(s)$.

Figure 3 depicts a Cosserat rod (assumed to be tube i here) with length ℓ, which is subject to external forces $\mathbf{F}$ and loads $\mathbf{L}$, as well as internal forces $\mathbf{n}$ and moments $\mathbf{m}$ at its free end. External forces can account for gravity, and/or interaction/environmental forces. A coordinate frame is attached to the rod and travels along its centerline (represented by the dashed line). The local z-axis of the frame is pointing towards the tangent of the curve and the x- and y-axes are established in a canonical way (different frame conventions can be utilized, e.g. Frenet-Serret's or Bishop's frames). This body coordinate frame is referred to as frame b in the following. Each point on the centerline can be described in a global reference frame w with orientation $\mathbf{R}^* \in SO(3)$ and position $\mathbf{r}^* \in E(3)$ of the coordinate frame.
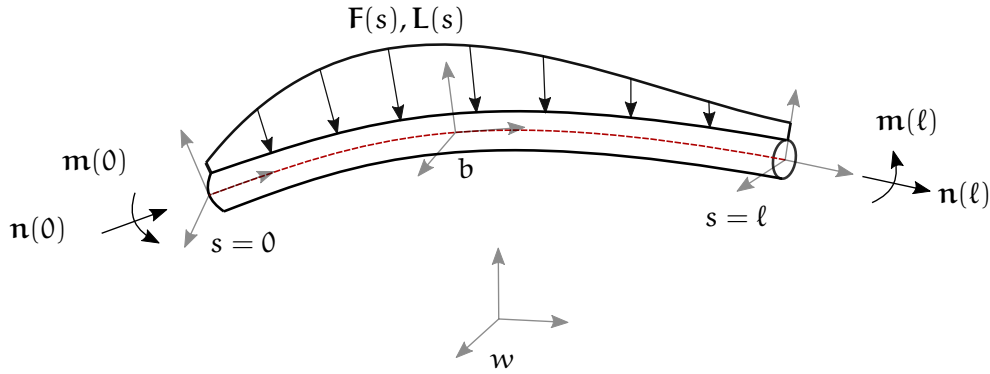
Figure 3: A Cosserat rod with length ℓ and s being the arc length parameter. The slender rod is subject to external forces $\mathbf{F}$ and loads $\mathbf{L}$, and internal forces $\mathbf{n}$ and moments $\mathbf{m}$ at its free end. A body coordinate frame b travels along the centerline (red dashed line) of the tube which is in relation to the global coordinate frame w.

The tube i is thus characterized by an arc length s parameterized curve $_w\mathbf{r}_i^{*b}(s)$ and the position and orientation of frames along the curve can then be represented by $_w\mathbf{g}_i^{*b}(s) \in SO(3)$, where this denotes a transformation matrix of frame b with respect to w. Thus, $(_w\mathbf{R}_i^b)^\mathsf{T} = {}_b\mathbf{R}_i^w$ and $_w\mathbf{g}_i^{*b}(s)$ is represented by

$$_w\mathbf{g}_i^{*b}(s) = \begin{bmatrix} _w\mathbf{R}_i^{*b}(s) & _w\mathbf{r}_i^{*b}(s) \\ \mathbf{0}^\mathsf{T} & 1 \end{bmatrix},$$

where $_w\mathbf{R}_i^{*b}(s) \in SO(3)$ and $_w\mathbf{r}_i^{*b}(s) \in E(3)$ represent the orientation and translation at s with respect to the global reference frame w. The local curvature vector $\mathbf{v}_i^*(s)$ can then be represented by

$$_b\mathbf{v}_i^*(s) = (_b\mathbf{R}_i^{*w}(s)\, \partial_s\, _w\mathbf{R}_i^{*b}(s))^\vee,$$

where $^\vee$ denotes the inverse of $^\wedge$, which describes the mapping from $\mathfrak{se}(3)$ to $\mathbb{R}^3$.

2.2.1.1   *Kinematic Equations*

The kinematic equations describe the evolution of the curvature and pose along arc length s

$$\partial_s \, {}_w\mathbf{r}_i^b(s) = {}_w\mathbf{R}_i^b(s) \, {}_b\vartheta(s),$$

$$\partial_s \, {}_w\mathbf{R}_i^b(s) = {}_w\mathbf{R}_i^b(s) \, {}_b\widehat{\upsilon}_i(s), \tag{1}$$

with

$$_w\mathbf{g}_i^b(s) = \begin{bmatrix} {}_w\mathbf{R}_i^b(s) & {}_w\mathbf{r}_i^b(s) \\ \mathbf{o}^\mathsf{T} & 1 \end{bmatrix},$$

where ∂_s represents the partial derivative with respect to s, ${}_b\vartheta$ and ${}_b\upsilon$ define the linear (extension and shear) and angular (bending and torsion) strains, respectively. Both are represented in the body coordinate frame b. The evolution is characterized by ${}_b\upsilon_i(s) = {}_b\upsilon_i^*(s) + \Delta_b\upsilon_i(s)$ and ${}_b\vartheta_i(s) = {}_b\vartheta_i^*(s) + \Delta_b\vartheta_i(s)$.

2.2.1.2   *Equilibrium Equations*

These equations are derived by writing the static equilibrium for each tube i. Describing the evolution of $\mathbf{m}$ and $\mathbf{n}$ along s, the force and moment equilibrium can be stated as

$$_w\mathbf{n}(s) - {}_w\mathbf{n}(0) + \int_0^s {}_w\mathbf{F}(\omega)\mathrm{d}\omega = \mathbf{0},$$

$$_w\mathbf{m}(s) + {}_w\mathbf{r}^b(s) \times {}_w\mathbf{n}(s) - {}_w\mathbf{m}(0) - {}_w\mathbf{r}^b(0) \times {}_w\mathbf{n}(0)$$
$$+ \int_0^s \big({}_w\mathbf{r}^b(\omega) \times {}_w\mathbf{F}(\omega) + {}_w\mathbf{L}(\omega)\big)\mathrm{d}\omega = \mathbf{0},$$

where the inner forces and moments ${}_w\mathbf{n}$ and ${}_w\mathbf{m}$, and the external forces and loads ${}_w\mathbf{F}$ and ${}_w\mathbf{L}$ are all represented in the global world coordinate system w. The differential equilibrium equations can be derived by taking the derivative with respect to s leading to

$$\partial_s \, {}_w\mathbf{n}(s) + {}_w\mathbf{F}(s) = \mathbf{0}, \tag{2}$$

$$\partial_s \, {}_w\mathbf{m}(s) + \partial_s \, {}_w\mathbf{r}^b(s) \times {}_w\mathbf{n}(s) + {}_w\mathbf{L}(s) = \mathbf{0}. \tag{3}$$

2.2.1.3   *Constitutive Equations*

These equations relate the linear strains ${}_b\vartheta$ and angular strains ${}_b\upsilon$ to the internal forces ${}_w\mathbf{n}$ and moments ${}_w\mathbf{m}$. Constitutive equations of the material are considered, where in this case linear elastic behavior along the tube is assumed for simplicity. To

express these in a global reference frame w, the constitutive equations are multiplied by a rotation matrix $_w\mathbf{R}^b(s)$ according to

$$_w\mathbf{n}(s) = {}_w\mathbf{R}^b(s) {}_b\mathbf{K}_v(s)({}_b\boldsymbol{\vartheta}(s) - {}_b\boldsymbol{\vartheta}(s)^*), \tag{4}$$

$$_w\mathbf{m}(s) = {}_w\mathbf{R}^b(s) {}_b\mathbf{K}_v(s)({}_b\boldsymbol{\upsilon}(s) - {}_b\boldsymbol{\upsilon}(s)^*), \tag{5}$$

where $_b\mathbf{K}_\vartheta$ and $_b\mathbf{K}_\upsilon$ are the linear and angular stiffness matrices, respectively. Assuming homogeneous material behavior, they are expressed as

$$_b\mathbf{K}_\vartheta = \begin{bmatrix} GA & 0 & 0 \\ 0 & GA & 0 \\ 0 & 0 & EA \end{bmatrix},$$

$$_b\mathbf{K}_\upsilon = \begin{bmatrix} EI_{xx} & 0 & 0 \\ 0 & EI_{yy} & 0 \\ 0 & 0 & GI_{zz} \end{bmatrix}.$$

G is the shear modulus, A is the area of the cross section, E is the elastic modulus, I_{xx}, I_{yy} are the second moments of area about the respective axis, and I_{zz} is the polar moment of inertia about the z-axis with $I_{zz} = I_{xx} + I_{yy}$. Note that G, A, E and I are constant along s for each tube i.

2.2.1.4 *Differential Equations*

The differential Cosserat rod equations can then be derived considering the kinematic rod, equilibrium and constitutive equations. The constitutive equations (4) and (5) are derived with respect to s. Substitution of the equilibrium equations (2) and (3), the kinematic equation (1), and multiplication of $(_w\mathbf{R}^b)^\mathsf{T}$ results in the following differential equations.

$$\begin{aligned}
\partial_{s} {}_w\mathbf{r}^b &= {}_w\mathbf{R}^b {}_b\boldsymbol{\vartheta}, \\
\partial_{s} {}_w\mathbf{R}^b &= {}_w\mathbf{R}^b {}_b\hat{\boldsymbol{\upsilon}}, \\
\partial_{s} {}_b\boldsymbol{\vartheta} &= \partial_{s} {}_b\boldsymbol{\vartheta}^* - {}_b\mathbf{K}_\vartheta^{-1}\big(({}_b\hat{\boldsymbol{\upsilon}} {}_b\mathbf{K}_\vartheta + \partial_{s} {}_b\mathbf{K}_\vartheta)({}_b\boldsymbol{\vartheta} - {}_b\boldsymbol{\vartheta}^*) + {}_b\mathbf{R}^w {}_w\mathbf{F}\big), \\
\partial_{s} {}_b\boldsymbol{\upsilon} &= \partial_{s} {}_b\boldsymbol{\upsilon}^* - {}_b\mathbf{K}_\upsilon^{-1}\big(({}_b\hat{\boldsymbol{\upsilon}} {}_b\mathbf{K}_\upsilon + \partial_{s} {}_b\mathbf{K}_\upsilon)({}_b\boldsymbol{\upsilon} - {}_b\boldsymbol{\upsilon}^*) \\
&\quad + {}_b\hat{\boldsymbol{\vartheta}} {}_b\mathbf{K}_\vartheta({}_b\boldsymbol{\vartheta} - {}_b\boldsymbol{\vartheta}^*) + {}_b\mathbf{R}^w {}_w\mathbf{L}\big).
\end{aligned} \tag{6}$$

Note, that s is omitted for practical reasons.

2.2.2 *Kirchhoff Rod Model*

A Kirchhoff rod is a special case of a Cosserat rod, where extension and transverse shear are neglected. The assumption of a tube i being a Kirchhoff rod is considered

in the scope of this work. The linear strains are defined to be constant $\vartheta = \vartheta^* = e_3$. The differential equations simplify to

$$\partial_s \, _w r^b = \, _w R^b \, e_3 \, ,$$

$$\partial_s \, _w R^b = \, _w R^b \, _b \hat{\upsilon} \, ,$$

$$\partial_s \, _w n = -\, _w F \, ,$$

$$\partial_s \, _b \upsilon = \partial_s \, _b \upsilon^* - \, _b K_\upsilon^{-1} \left((_b \hat{\upsilon} \, _b K_\upsilon + \partial_s \, _b K_\upsilon)(_b \upsilon - \, _b \upsilon^*) + \, _b R^w \, _w L \right) \, .$$

2.2.3 *Combination of Multiple Tubes*

Consider now the combination of multiple tubes i, where each tube is assumed to be a Kirchhoff rod. This implies that extension and shear of the tubes are neglected, such that $_b \vartheta = [0\,0\,1]^\mathsf{T}$. It further assumes that extension and shear have only little effect on the deformation of the tubes compared to bending and torsion. The model presented here, was originally published by (Rucker, Jones, and Webster III, 2010a) and considers the following assumptions

- inextensibility of the tubes,

- no transverse shear of the tubes,

- neglection of friction, and

- linear elastic material behavior.

In the following, the Kirchhoff rod equations are derived for multiple tubes and again, the differential equations arise by considering the kinematic equations, the equilibrium equations, and the constitutive equations.

2.2.3.1 *Kinematic Equations*

For the sake of simplicity, it is first assumed that the tubes are aligned and start at $s = 0$ and end at s. As the tubes twist independently (such that orientation of frames may vary), each of the tubes deforms from an initial reference state $g_i^*(s)$ to a final state $g_i(s)$. As the tubes are placed concentrically into one another, their final curves (represented by points) align so that there exists a final deformed curve $g(s)$ for all tubes.

The relative rotation between the tubes, illustrated in Figure 4, can be described by a rotation $_B R_{\theta_i}^b$ about the local z-axis by angle θ_i, where the coordinate frame B defines the body coordinate frame of tube $i = 1$, and b is the body coordinate frame of tube i. The rotation angle θ_i is measured with respect to tube $i = 1$. This rotational relationship is described by

$$_w R_i^b(s) = \, _w R_1^B(s) \, _B R_{\theta_i}^b, \tag{7}$$

with

$$_B R_\theta^b = \begin{bmatrix} \cos(\theta_i) & -\sin(\theta_i) & 0 \\ \sin(\theta_i) & \cos(\theta_i) & 0 \\ 0 & 0 & 1 \end{bmatrix},$$

such that this angular change can also be represented by

$$\partial_s \theta_i = {}_b\upsilon_{i,z} - {}_B\upsilon_{1,z}.$$
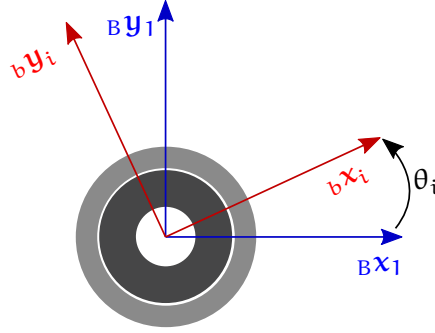
Figure 4: Rotational difference between the tubes measured with respect to tube 1 by a rotation about the z-axis by angle θ_i.

A relation between the curvatures is essential to determine the final curve. This can be derived by considering the kinematic equation (1) for a single rod. Substituting equation (7) into the definition for υ_i leaves

$$_b\upsilon_i(s) = {}_b\mathbf{R}_i^w(s)\partial_s \, {}_w\mathbf{R}_i^b(s)^\vee = {}_b\mathbf{R}_{\theta_i}^B \, {}_B\upsilon_1 + \partial_s\theta_i\mathbf{e}_3.$$

Determination of the derivative with respect to s to describe the evolution of $_b\upsilon_i$ then yields

$$\partial_s \, {}_b\upsilon_i(s) = \partial_s\theta_i \, \partial_{\theta_i \, b}\mathbf{R}_{\theta_i}^B \, {}_B\upsilon_1 + {}_b\mathbf{R}_{\theta_i}^B \partial_s \, {}_B\upsilon_1 + \partial_s^2\theta_i\mathbf{e}_3, \tag{8}$$

where ∂_{θ_i} represents the partial derivative with respect to θ_i.

2.2.3.2 *Equilibrium Equations*

Considering multiple precurved overlapping tubes i, the static equilibrium considering external forces can be written as

$$\int_0^s \sum_{i=1}^n {}_w\mathbf{F}_i(\omega)d\omega - \sum_{i=1}^n {}_w\mathbf{n}_i(s) = \mathbf{0}, \tag{9}$$

and

$$\int_0^s \left({}_w\mathbf{r}^b(\omega) \times \sum_{i=1}^n {}_w\mathbf{F}_i(\omega) + \sum_{i=1}^n {}_w\mathbf{L}_i(\omega) \right) d\omega$$
$$- \sum_{i=1}^n \left({}_w\mathbf{m}_i(s) + {}_w\mathbf{r}^b(s) \times {}_w\mathbf{n}_i(s) \right) = \mathbf{0}, \tag{10}$$

where $\mathbf{n}_i$ and $\mathbf{m}_i$ are the internal forces and moments at each cross section of tube i, and $\mathbf{F}_i$ and $\mathbf{L}_i$ are the external forces and loads in the global coordinate frame w.

Taking the derivative of equation (9) and (10) with respect to s yields the differential equilibrium equations for multiple overlapping tubes

$$\sum_{i=1}^{n} \left(\partial_s \, {}_w\mathbf{n}_i(s) + {}_w\mathbf{F}_i(s) \right) = \mathbf{0},$$

$$\sum_{i=1}^{n} \left(\partial_s \, {}_w\mathbf{m}_i(s) + \partial_s \, {}_w\mathbf{r}^b(s) \times {}_w\mathbf{n}_i(s) + {}_w\mathbf{L}_i(s) \right) = \mathbf{0}. \tag{11}$$

2.2.3.3   *Constitutive Equations*

The linear constitutive equation can easily be written for multiple tubes

$$\sum_{i=1}^{n} {}_w\mathbf{m}_i(s) = \sum_{i=1}^{n} {}_w\mathbf{R}_i^b(s) \, {}_b\mathbf{K}_i(s) ({}_b\boldsymbol{v}_i(s) - {}_b\boldsymbol{v}_i^*(s)), \tag{12}$$

where

$${}_b\mathbf{K}_i = \begin{bmatrix} E_i I_{xx_i} & 0 & 0 \\ 0 & E_i I_{yy_i} & 0 \\ 0 & 0 & G_i I_{zz_i} \end{bmatrix}.$$

Here, the material parameters and geometry of each tube i need to be considered. It is assumed that material parameters are constant for each tube i. G_i is the shear modulus, E_i is the elastic modulus, I_{xx_i} and I_{yy_i} are the second moments of area about the respective axis, and I_{zz_i} is the polar moment of inertia about the z-axis of each tube i.

2.2.3.4   *Differential Kirchhoff Rod Equations*

To obtain the set of differential Kirchhoff rod equations, the kinematic constraints, the equilibrium equations and the constitutive equation for multiple tubes are considered. Note that the arc length parameter s is omitted for practical reasons in the following section. To later receive a definition of $\partial_s \, {}_B\boldsymbol{v}_1$ with respect to the state variables, the constitutive equation (12) is derived with respect to s as (note, that s is again omitted for practical reasons)

$$\sum_{i=1}^{n} \partial_s \, {}_w\mathbf{m}_i = \sum_{i=1}^{n} \partial_s \, {}_w\mathbf{R}_i^b \, {}_b\mathbf{K}_i ({}_b\boldsymbol{v}_i - {}_b\boldsymbol{v}_i^*) + \sum_{i=1}^{n} {}_w\mathbf{R}_i^b \, \partial_s \, {}_b\mathbf{K}_i$$

$$({}_b\boldsymbol{v}_i - {}_b\boldsymbol{v}_i^*) + \sum_{i=1}^{n} {}_w\mathbf{R}_i^b \, {}_b\mathbf{K}_i (\partial_s \, {}_b\boldsymbol{v}_i - \partial_s \, {}_b\boldsymbol{v}_i^*). \tag{13}$$

Consider the equilibrium equation (11) and substitute $\partial_s \, _w\mathbf{R}_i^b = \, _w\mathbf{R}_i^b \, _b\widehat{\upsilon}_i$ and equation (13). Substituting then $_w\mathbf{R}_i^b = \, _b\mathbf{R}_1^B \, _B\mathbf{R}_{\theta_i}^b$ (equation (7)) results in

$$\sum_{i=1}^{n} \, _w\mathbf{R}_i^b \left(_b\mathbf{K}_i(\partial_s \, _b\upsilon_i - \partial_s \, _b\upsilon_i^*) + (_b\widehat{\upsilon}_i \, _b\mathbf{K}_i + \partial_s \, _b\mathbf{K}_i) \right.$$

$$\left. (_b\upsilon_i - \, _b\upsilon_i^*) \right) + \sum_{i=1}^{n} \left(\partial_s \, _w\mathbf{r}^b \times \, _w\mathbf{n}_i + \, _w\mathbf{L}_i \right) = 0.$$

Apply $\partial_s \, _w\mathbf{r}^b = \, _w\mathbf{R}^b \, \mathbf{e}_3$ and equilibrium equation (9). Multiplying with $(_b\mathbf{R}_1^B)^\mathsf{T}(s)$ yields

$$\sum_{i=1}^{n} \, _B\mathbf{R}_{\theta_i}^b \left(_b\mathbf{K}_i(\partial_s \, _b\upsilon_i - \partial_s \, _b\upsilon_i^*) + (_b\widehat{\upsilon}_i \, _b\mathbf{K}_i + \partial_s \, _b\mathbf{K}_i)(_b\upsilon_i - \, _b\upsilon_i^*) \right)$$

$$+ \mathbf{e}_3 \times (_b\mathbf{R}_1^B)^\mathsf{T} \int_0^s \, _w\mathbf{F}_i(\omega)d\omega + (_b\mathbf{R}_1^B)^\mathsf{T} \, _w\mathbf{L}_i = 0.$$

Substitution of equation (8) into the prior determined equation and solving for the first two components of $\partial_s \, _B\upsilon_1$ yields

$$\begin{bmatrix} \partial_s \, _B\upsilon_{1,x} \\ \partial_s \, _B\upsilon_{1,y} \end{bmatrix} = \sum_{i=1}^{n} -_b\mathbf{K}_i^{-1}\mathbf{R}_{\theta_i} \left(_b\mathbf{K}_i\left(\partial_s\theta_i \, \partial_{\theta_i}(_B\mathbf{R}_{\theta_i}^b)^\mathsf{T} \, _B\upsilon_1 - \partial_s \, _b\upsilon_i^*\right) \right.$$

$$\left. + (_b\widehat{\upsilon}_i \, _b\mathbf{K}_i + \partial_s \, _b\mathbf{K}_i)(_b\upsilon_i - \, _b\upsilon_i^*) \right) - \sum_{i=1}^{n} \, _b\mathbf{K}_i^{-1} \left(\widehat{\mathbf{e}}_3(_b\mathbf{R}_1^B)^\mathsf{T} \right.$$

$$\left. \int_0^s \, _w\mathbf{F}_i(\omega)d\omega + (_b\mathbf{R}_1^B)^\mathsf{T} \, _w\mathbf{L}_i \right) \bigg|_{x,y}, \quad (14)$$

where $|_{x,y}$ denotes selection of only the first two components of a vector.
As equation (14) only enables to solve for $\partial_s \, _B\upsilon_{1,x}, \partial_s \, _B\upsilon_{1,y}$, the last differential equation is obtained by considering the Kirchhoff rod equation (6) for a single tube i

$$\partial_s \, _b\upsilon_i = \partial_s \, _b\upsilon_i^* - \, _b\mathbf{K}_{\upsilon_i}^{-1}\left((_b\widehat{\upsilon}_i \, _b\mathbf{K}_{\upsilon_i} + \partial_s \, _b\mathbf{K}_{\upsilon_i})(_b\upsilon_i - \, _b\upsilon_i^* + (_w\mathbf{R}_i^b)^\mathsf{T} \, _w\mathbf{L}_i\right).$$

Substitution of $_b\mathbf{K}_{\upsilon_i}, \, _b\widehat{\upsilon}_i$ and solving for the third component of $_b\upsilon_i$, results in a representation of $\partial_s \, _b\upsilon_{i,z}$ in terms of the state variables. It is given by

$$\partial_s \, _b\upsilon_{i,z} = \partial_s \, _b\upsilon_{i,z}^* + \frac{E_iI_i}{G_iI_{zz_i}}(_b\upsilon_{i,x} \, _b\upsilon_{i,y}^* - \, _b\upsilon_{i,y} \, _b\upsilon_{i,x}^*) - \frac{1}{G_iI_{zz_i}}\mathbf{e}_3^\mathsf{T}(_w\mathbf{R}_i^b)^\mathsf{T} \, _w\mathbf{L}_i.$$

2.2.4 *Solving the Differential Equations*

To determine the model equations of multiple interleaved tubes, a system of continuous rods must be solved considering specific boundary conditions. This includes the consideration of sections that are defined as regions of constant curvature and transition points that mark the passing from one section to the other. The sections of constant curvature for a three tube CTCR are illustrated in Figure 5. For each section,
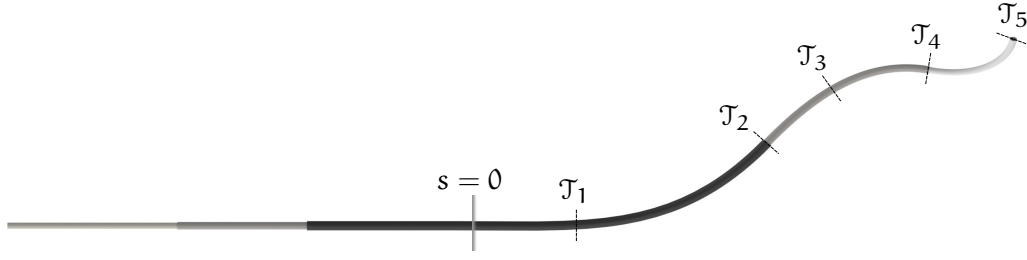
Figure 5: Concentric tube robot composed of three tubes with 5 sections of constant curvature and corresponding set of transition points $\mathcal{T}_{1-5}$, which are elements of $\mathcal{T}$.

the set of differential equations are to be solved considering the following boundary conditions. The set of transition points is defined by

$$\mathcal{T} = \{0, \beta_1 + \ell_{s_1}, \beta_1 + \ell_{s_1} + \ell_{c_1}, \beta_2 + \ell_{s_2}, \beta_2 + \ell_{s_2} + \ell_{c_2}, ..., \beta_n + \ell_{s_n}, \beta_n + \ell_{s_n} + \ell_{c_n}\},$$

where all elements < 0 from $\mathcal{T}$ can be omitted.

2.2.4.1 Boundary Conditions

The boundary conditions consider geometrical constraints of the CTCR, force and moment equilibrium, and the continuity of the space curve. The geometrical constraints define the conditions for arc length s and that the tubes are considered to be straight for $s < 0$. To ensure continuity of the space cure $_w\mathbf{g}_i^b(s^+)$, the conditions apply as

$$_w\mathbf{g}_i^b(s^-) = {_w}\mathbf{g}_i^b(s^+),$$

where s^- defines the state right before the transition point and s^+ after. The transition also requires a static equilibrium as

$$\sum_{i=1}^n {_w}\mathbf{m}_i(s^-) = \sum_{i=1}^n {_w}\mathbf{m}_i(s^+) + \sum_{i=1}^n {_w}\mathbf{L}_{p,i}(s),$$

where $_w\mathbf{L}_{p,i}(s)$ is a point moment applied to tube i in the world coordinate system w. Another equilibrium to be considered is at the tip of the robot, which becomes

$$\sum_{i=1}^n {_w}\mathbf{m}_i(\ell) - \sum_{i=1}^n {_w}\mathbf{L}_{p,i}(\ell) = 0,$$

where $_w\mathbf{L}_{p,i}$ is a point load.

2.2.4.2 Shooting Method

The differential equations are to be solved numerically utilizing a shooting method, as an analytic solution to solve the differential equations exists only for a CTCR with $n = 2$ tubes with circular precurvature (Lock et al., 2010; Rucker, Jones, and Webster III, 2010b).

For other tube combinations, integration from base to tip is performed (though from tip to base is also possible) to solve the differential equations. The integration

defines an initial value problem (can be solved using Runge-Kutta), where the solver guesses for unknown conditions at the proximal end and solves for initial curvatures. The boundary conditions must be considered. If they are not satisfied, the solver guesses new values. To implement this model, the following initial conditions apply

$$_b\mathbf{r}_1^B(0) = \mathbf{0},$$

$$_b\mathbf{R}_1^B = \begin{bmatrix} \cos(\alpha_1 + \beta_1{}_bv_{1,z}^*) & -\sin(\alpha_1 + \beta_1{}_bv_{1,z}^*) & 0 \\ \sin(\alpha_1 + \beta_1{}_bv_{1,z}^*) & \cos(\alpha_1 + \beta_1{}_bv_{1,z}^*) & 0 \\ 0 & 0 & 1 \end{bmatrix},$$

$$\theta_i = (\alpha_i + \beta_i{}_bv_{i,z}^*) - (\alpha_1 + \beta_1{}_bv_{1,z}^*),$$

$$\theta_1(\beta_1) = 0.$$

2.3 CONCLUSION

As the model presented here requires numerical methods to solve highly nonlinear differential equations, incorporation into an optimization framework represents a major challenge for this work. The forward kinematic model limits the application of several optimization strategies, as methods are to be acquired that can handle function nonlinearity. Additionally, the absence of analytically solvable inverse kinematics represents a major limitation when it comes to design synthesis of CTCR, as the straightforward computation from parameters in task space (end-effector position of the robot) into configuration space is not possible.

3

EVOLUTIONARY OPTIMIZATION METHODS

This chapter states the definition of a general optimization problem and presents an overview of evolutionary optimization methods. The methods are categorized into different types, which are suited for distinct problems and functions. Specifically, particle swarm optimization is presented, as this strategy is a core method of this thesis. Finally, this chapter describes multi-objective optimization methods and their implementation with regard to particle swarm optimization.

3.1 OPTIMIZATION PROBLEM

An optimization problem arises from searching an optimal solution to a problem, i.e. the necessity to find an optimum (a minimum or a maximum). In many world problems there is even a need to finding not one solution to a problem, but multiple or infinite numbers of solutions. Optimization methods have been specifically evolved to solve these problems and apply to many domains. Generally, optimization methods describe the numerical solution to a problem and use an initial start value as an estimate (Antoniou and Lu, 2007). The problem can be defined by a function and the applied optimization method utilizes it to solve for extrema.

3.1.1 *Problem Definition*

If one aims to minimize an objective function $f(\boldsymbol{x})$, then function dependent parameters $x_1, x_2, .., x_m$ have to be adjusted such that the function f is minimized, with m being the number of decision variables. The optimization problem can thus be stated as

$$\text{minimize } y = f(\boldsymbol{x}) = f(x_1, x_2, ..., x_m),$$

where $\boldsymbol{x}$ defines the decision vector $\boldsymbol{x} = [x_1, x_2, ..., x_m]^\mathsf{T}$ of the optimization problem and y defines the objective or cost function. Each optimization problem can be written as a minimization of the objective function $f(\boldsymbol{x})$ or a maximization of the objective function $-f(\boldsymbol{x})$, as

$$\text{minimize } f(\boldsymbol{x}) \equiv \text{maximize} \left[-f(\boldsymbol{x}) \right].$$

3.1.2 *Local and Global Minima*

A function can have multiple local minima. A local minimum at $\tilde{\boldsymbol{x}}$ exists for $f(\tilde{\boldsymbol{x}})$, if

$$f(\tilde{\boldsymbol{x}}) \leqslant f(\boldsymbol{x}) \text{ for all } \|\boldsymbol{x} - \tilde{\boldsymbol{x}}\|_2 < \rho,$$

where ρ defines a user-defined neighborhood with $\rho > 0$, and $f(\tilde{\mathbf{x}})$ has a global minimum at $\tilde{\mathbf{x}}$ if

$$f(\tilde{\mathbf{x}}) \leqslant f(\mathbf{x}) \text{ for all } \mathbf{x}.$$

If a function has multiple local minima, it is called multimodal (Simon, 2013). Figure 6 represents global and local optima of a function in $\mathbb{R}^2$.
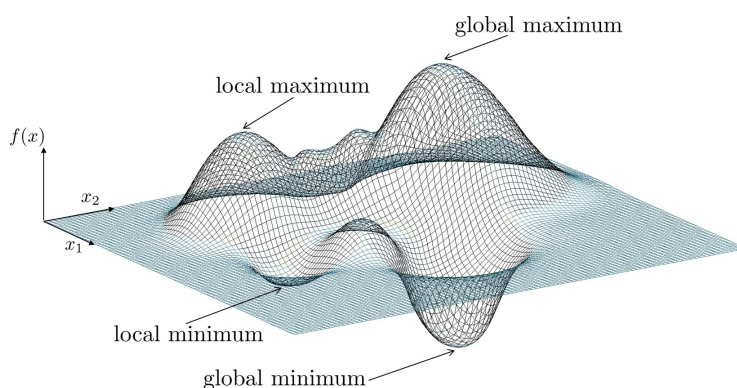
Figure 6: Global and local minima and maxima of a function in $\mathbb{R}^2$.

3.1.3   *Constraints*

The optimization problem can be subject to constraint functions, which can be either equality, or inequality constraint functions as

$$g_i(\mathbf{x}) = 0 \qquad\qquad h_i(\mathbf{x}) \leqslant 0 \qquad\qquad i \in \mathbb{N}\backslash 0.$$

3.2   OVERVIEW OF EVOLUTIONARY OPTIMIZATION ALGORITHMS

Optimization methods can be divided into several subcategories. The manifold of optimization algorithms is large, and the type of optimization problem defines the utilized optimization technique. Selection of an appropriate optimization technique is challenging and not a straightforward task to solve. Generally said, optimization algorithms can be divided into **linear** and **nonlinear** methods, where nonlinear optimization algorithms are iterative methods (gradient is determined numerically) that can be utilized for complex and multimodal problems (Nelles, 2001). See Figure 7 for an overview of optimization methods.

The focus of this thesis is **evolutionary optimization**, as these algorithms are envisioned to be suitable for the structural design optimization problem of CTCR. Evolutionary optimization algorithms are **probabilistic** and fall into the category of **global** optimization methods. Global optimization techniques are suited to explore the overall parameter space and are thus more likely to find global optima. They are generally applicable to complex problems with many optima, nonlinearities, or constrained problems. However, they are not always prone to find a global optimum. For these type of algorithms, there is usually a tradeoff between global exploration and convergence (Nelles, 2001).
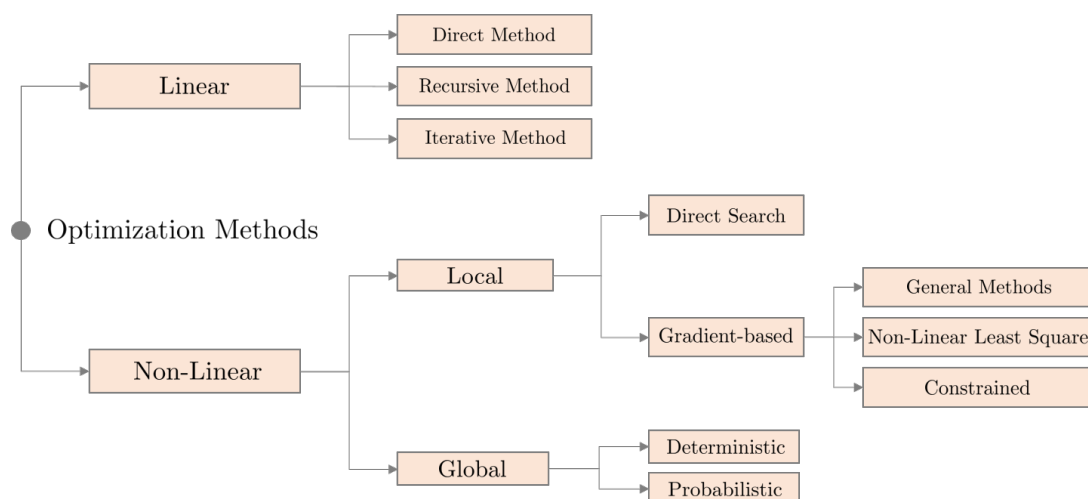
Figure 7: Overview of optimization methods.

Evolutionary algorithms utilize a population-based approach with many iterations (Simon, 2013). Such algorithms are particularly suitable for complex problems and can be used if gradient-based approaches do not provide a sufficient solution or if a gradient of the function cannot be determined. Thus, evolutionary algorithms have been applied to many domains, e.g. robotics, neural networks, or in medicine (Simon, 2013). These algorithms are further suitable to be transferred to multi-objective optimization problems and represent powerful optimization tools (Reyes-Sierra and Coello Coello, 2006).

This thesis concentrates on these types of algorithms, which are further explained in the following. Though many sub-classes and modifications of evolutionary algorithms exist, the following sections concentrate on the most prominent examples, which are genetic algorithms, evolutionary programming, evolution strategy, genetic programming, and swarm intelligence (Simon, 2013; Yu and Gen, 2010).

3.2.1 *Genetic Algorithms*

Genetic algorithms are the most prominent evolutionary optimization methods and represent the inspiration for many of the following algorithmic approaches. They were first introduced by (Holland, 1962) and further extended by (Goldberg, 1989; Goldberg and Holland, 1988). The algorithm is based on the idea of natural selection and the population of individuals. Individuals can reproduce and represent candidate solutions. The algorithm consists of three main steps: evaluation, selection, and recombination. Evaluation represents the assessment of the fitness of each individual within the population. The individuals with the best fitness among the population (parents) are selected for reproduction. Recombination of genes can either happen in the sense of reproduction (the crossover of genes) or by mutation. Mutation of selected individuals ensures diversity and the exploration of space and represents a probabilistic factor. The reproduced individuals then represent the next child population. This genetic cycle continues until a sufficient solution is found, or a maximum number of generations is reached. The genetic cycle is illustrated in Figure 8.

The decision vectors are coded into a binary representation such that bit strings represent candidate solutions. This is a complex task as the representation of the candidate solution is crucial for the functionality of the algorithm (Eiben and Smith, 2003). In genetic algorithms, the fitness score represents the objective function. There exist various representations and operators for genetic algorithms, including different strategies for reproduction and mutation (Eiben and Smith, 2003). It further includes different population strategies, where e.g. only the child population remains and no parents or parent and child populations are overlapping (Weicker, 2015).
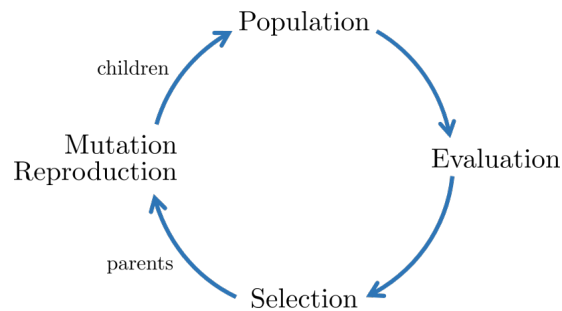
Figure 8: Genetic cycle that consists of the current population, fitness evaluation, selection of individuals, and recombination including reproduction (crossover) and mutation.

3.2.2 *Evolution Strategies*

Evolution strategies intend to simulate biological evolution. They were first introduced by (Rechenberg, 1973). In contrast to genetic algorithms, the decision vectors are represented by real numbers $\mathbb{R}$. Further, the first publications utilized mostly mutation operators and the selection of individuals (Simon, 2013). Gaussian mutation operations ensure the exploration of the space and the candidate solutions are selected randomly from the parent population (Weicker, 2015). The self-adaption of mutation step sizes is characteristically for most implementations of evolution strategies (Eiben and Smith, 2003). Recombination methods can either be discrete or intermediate, such that alleles from two parents are randomly selected or averaged.

3.2.3 *Evolutionary Programming*

Evolutionary programming is comparable to evolution strategies and aims to simulate biological evolution and models artificial intelligence. It was invented by (Fogel, Owens, and Walsh, 1966). The decision vectors are also represented by real numbers $\mathbb{R}$ and mutation and selection operators are applied. New individuals are generated through mutation using statistical distribution and Gaussian perturbation (Eiben and Smith, 2003; Simon, 2013). The principle relies on the fitness computation of individuals and then stochastic selection of some members for the next generation. In evolutionary programming, recombination strategies are not applied and the structure of individuals is fixed (Weicker, 2015).

3.2.4 *Genetic Programming*

Genetic programming is based on genetic concepts - in contrast to evolution strategies and evolutionary programming. It is a stochastic technique and similar to evolutionary programming and strategies, but here the structure of the program can change. This means that genetic programming can be used for problems, where the specific structure of the optimization problem or the number of optimization parameters is unknown (Simon, 2013). It rather belongs to the machine learning family, as it is based on learning concepts and the methods are less constrained (Eiben and Smith, 2003). Genetic programming techniques also use reproduction operators, whereas mutation is not prominent (Weicker, 2015). The methods are built upon tree structures and individuals can vary in size (Weicker, 2015).

3.2.5 *Swarm Intelligence*

Swarm intelligence represents algorithms that are based on the idea of natural selection (Yu and Gen, 2010). They are intended to simulate natural swarm behavior of, for instance, a flock of birds, fish, or insects looking for food or a mating partner. This includes algorithms as particle swarm optimization, ant colony optimization, and artificial bee colony optimization (Yu and Gen, 2010).

Researchers no dot agree whether swarm intelligence belongs to the family of evolutionary algorithms (Simon, 2013). However, as they operate in a similar manner using a candidate solution which evolves from generation to generation, they are considered as evolutionary algorithms in the following. The inventors of particle swarm optimization refer to it as an evolutionary algorithm, which is similar to evolutionary programming and genetic algorithms (Shi and Eberhart, 1999).

3.2.6 *Summary*

Evolution strategies, evolutionary programming, and genetic programming are all adaptions of genetic algorithms. In contrary to other evolutionary algorithms, particle swarm optimization is relatively simple, as it has only one operator for computing new offspring. In that sense, it is different from other evolutionary algorithms, as it does not use selection and crossover. However, it is still a population-based and fitness-oriented approach (Yu and Gen, 2010). Swarm intelligence has become one of the most prominent evolutionary algorithms, which might be explainable by its low computational cost (Reyes-Sierra and Coello Coello, 2006; Yu and Gen, 2010). The authors in (Hassan et al., 2005) investigate the computational efficiency and performance of genetic versus particle swarm optimization based on different test functions. Both algorithms perform similar but particle swarm optimization with lower computational cost, as it needs fewer function evaluations. Further, particle swarm optimization requires no binary coding and parameters can take any value.

The assumption is that evolutionary optimization might be an efficient method to cope with the structural design synthesis of CTCR. Due to the prior mentioned advantages of particle swarm optimization, the following sections concentrate on

swarm intelligence. Note, that the performance of an algorithm is problem dependent (Yu and Gen, 2010), such that other genetic algorithms might be suitable to cope with the parameter selection of CTCR as well. However, this thesis specifically investigates the applicability of particle swarm optimization for the structural design synthesis of CTCR.

3.3 PARTICLE SWARM OPTIMIZATION

As particle swarm optimization is the underlying algorithm of this work, it is explained in detail in the following. There exist many extensions of the original implementation, however, this section introduces the original concept. The selection of particle swarm optimization for the structural design optimization of CTCR is discussed in more detail in the following chapters.

The particle swarm algorithm is a heuristic search algorithm, which is inspired by the social behavior of a swarm and was originally introduced by (Kennedy and Eberhart, 1995). It intends to simulate the social behavior of a swarm, which moves through space in seek for food and tries to find the best fit possible (Kennedy and Eberhart, 1995). The authors intend to transfer this behavior to optimization problems assuming that the swarm consists of multiple particles moving through the search space. It is considered to be an iterative process, where the swarm consists of a number of particles P that move through the search space and change their position within space for each generation t until the maximum number of generations T is reached. Each particle k is defined by its current position x_k and a velocity v_k, where the position of a particle resembles the decision vector of the optimization problem. The position and velocity change from generation t to the next generation $t+1$ and the velocity v_k of a particle is influenced by its personal best position p_{b_k} the particle achieved so far and a global best position g_b within the swarm across all generations (also referred to as leaders). As a position corresponds to a solution/decision vector, the position of a particle x_k can consist out of multiple components m and represent a vector (i.e. multidimensional parameter space) (Kennedy and Eberhart, 1995). The velocity of each particle x_k^t is determined with

$$v_k^{t+1} = \eta \cdot v_k^t + c_1 \cdot r_1 \cdot (p_{b_k}^t - x_k^t) + c_2 \cdot r_2 \cdot (g_b^t - x_k^t), \tag{15}$$

where η defines the inertia weight that controls the influence of the current velocity, c_1 and c_2 are constants controlling the influence of the personal versus global best position, and r_1 and r_2 randomly influence the velocity v_k^{t+1}. r_1 and $r_2 \in [0,1] \in \mathbb{R}$. The position x_k^{t+1} at time step $t+1$ can then be determined using equation (15) as

$$x_k^{t+1} = x_k^t + v_k^{t+1}.$$

The objective function within particle swarm optimization is represented by the cost y of a particle k. The cost y defines the "goodness" of the position x_k of a particle and indicates how close the particle is to its goal, i.e. to an optimum.

Figure 9 illustrates the algorithm's cycle. The selection of leaders, the determination of each particle's cost, and the velocity and position of a particle change for each generation t until the maximum number of generations T is reached. The output of

the algorithm and also the solution to the optimization problem is then the global best position g_b.
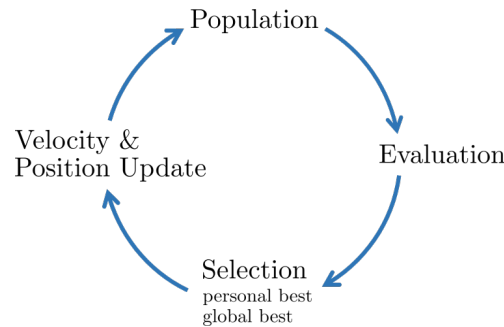
Figure 9: Particle swarm optimization cycle that consists of the current population, fitness evaluation, selection of individuals, and update of each particle's velocity and position.

3.4 ADAPTATIONS OF PARTICLE SWARM OPTIMIZATION

There exist various adaptions of the original particle swarm optimization (Kennedy and Eberhart, 1995). This includes, for instance, the incorporation of constraints, the consideration of different topology approaches, and the transfer from fixed to a variable dimension of decision vectors. The latter is especially important in the scope of this thesis. The following adaptions represent the most prominent and important extensions (considering this work) of particle swarm optimizations.

3.4.1 Constraints

The consideration of constraints is important in most real-world applications, as optimization problems are usually subject to constraints. This is especially true for the structural design of CTCR. It applies for particle swarm optimization as follows. If the position of a particle x_k^{t+1} is not within the search space, then strategies to reposition the particle's position back into the search space considering upper u_b and lower l_b parameter boundaries are to be applied. There exist various strategies to include these constraints. The following present the most prominent approaches, see (S. Xu and Rahmat-Samii, 2007) for an overview.

3.4.1.1 Penalty

This method accepts a position outside the search space of the particle (Parsopoulos and Vrahatis, 2005). However, a particle exceeding the search space receives a penalty, which influences its quality and it is rated worse against other particles. In future generations, particles exceeding the search space thus have a disadvantage among other particles within the swarm.

3.4.1.2   *Truncation*

If a particle exceeds the parameter space in any of the dimensions, this method constrains the particle's position component either at the lower l_b or upper boundary u_b of the parameter space (Coello Coello, Toscano Pulido, and Salazar Lechuga, 2004).

$$
x_k^t = \begin{cases} u_b & \text{, if } x_k^t > u_b \\ l_b & \text{, if } x_k^t < l_b, \end{cases}
$$

where the comparison is done for each element.

3.4.1.3   *Randomization*

If a particle's component exceeds the limitations of the parameter space, the particle's component in this dimension is assigned a new randomly chosen position

$$
x_k^t \in [l_b, u_b].
$$

3.4.1.4   *Reflection*

If a particle's component exceeds the parameter space, the component's position is reflected at the boundary limit into the opposite direction of the parameter space

$$
x_k^t = \begin{cases} u_b - (x_k^t - u_b) & \text{, if } x_k^t > u_b \\ l_b + (l_b - x_k^t) & \text{, if } x_k^t < l_b. \end{cases}
$$

3.4.1.5   *Reflection to Other Side*

This method is similar to the method mentioned before, but the particle's position is reflected at the other side of the boundary limit

$$
x_k^t = \begin{cases} l_b + (x_k^t - u_b) & \text{, if } x_k^t > u_b \\ u_b - (l_b - x_k^t) & \text{, if } x_k^t < l_b. \end{cases}
$$

3.4.2   *Topologies*

Topologies describe the connectivity of particles within the swarm and influence their information exchange. The performance of the algorithm is depended on its topology and the selection of the leader within the neighborhood. This implies that there exist strategies that do not utilize the global best leader approach but utilize different strategies to determine the leader of a swarm by neighborhood topologies. The original implementation of particle swarm optimization utilizes the **global topology** approach, where all particles are connected with all others. Here, the leader of the swarm is the global best position g_b^t considering all particles.

Other topologies consider each particle to be connected to a specific number of neighbors within the swarm and the leader is determined within a local neighborhood - not within the overall swarm. Some neighborhoods can be either assigned through metrics, stochastically, randomly or can also be static (Reyes-Sierra and Coello Coello, 2006; Simon, 2013). Thus, the selected topology has a high influence on the convergence and exploration rate of the algorithm. As the global topology ensures an information exchange with all particles, it enables a high convergence rate. For the same reason, this topology is also limited in exploration and has a higher tendency to converge towards local extrema. The other extreme is the empty topology, where each particle is only connected to itself. This enables high exploration of the search space, but convergence is slow (Reyes-Sierra and Coello Coello, 2006).

3.4.3 *Variable Dimension*

This is an extension to the original proposed particle swarm optimization algorithm and has been recently proposed by (Kadlec and Šeděnka, 2018; Mukhopadhyay and Mandal, 2014; Xue et al., 2014). It is also referred to as particle swarm optimization with variable-length or grammatical swarm approach. Here, the dimension of each particle k within a swarm may vary and the decision vectors can be of different length. This is especially suited for those problems, where the dimension of parameters is not known a priori, and the decision space is thus of variable dimension. This method can be used to search for an optimal dimension of the decision vector. The proposed optimization algorithm has been proven to be effective in performance and optimization result by (Kadlec and Šeděnka, 2018; Mukhopadhyay and Mandal, 2014; Xue et al., 2014).

In contrast to general particle swarm optimization, the velocity must be determined differently, where each component m of a particle k is considered. This is necessary, as each particle exhibits a different dimension. The overall number of components of a particle is defined as N_m and the overall number of components within the global best solution g_{b_m} is N_{m_g}. There exist three scenarios to determine the velocity $v_{k_m}^t$ for each component, considering N_m and N_{m_g}

1) $N_m = N_{m_g}$

$$v_{k_m}^{t+1} = \eta \cdot v_{k_m}^t + c_1 \cdot r_1 \cdot (p_{b_{k_m}}^t - x_{k_m}^t) + c_2 \cdot r_2 \cdot (g_{b_m}^t - x_{k_m}^t). \tag{16}$$

2) $N_m > N_{m_g}$

The number of N_{m_g} components are selected randomly from x_k. The velocity for these components is determined according to equation (16). The velocity of the remaining $N_m - N_{m_g}$ components m is determined with

$$v_{k_m}^{t+1} = \eta \cdot v_{k_m}^t + c_1 \cdot r_1 \cdot (p_{b_{k_m}}^t - x_{k_m}^t).$$

3) $N_m < N_{m_g}$

N_m components are randomly drawn from g_b and the velocity is determined with equation (16) using the selected components. The position of each particle's component $x_{k_m}^{t+1}$ is then determined with

$$x_{k_m}^{t+1} = x_{k_m}^t + v_{k_m}^{t+1}.$$

3.4.4 *Summary*

Particle swarm optimization has one operating mechanism to compute a new population. There exist multiple variables that can be altered to influence this mechanism and change the effect on exploration versus exploitation of the parameter space.

Specifically, the incorporation of constraints can be challenging, as there exist multiple methods for implementation. The adherence to constraints highly influences the outcome of the algorithm. The authors in (Alvarez-Benitez, Everson, and Fieldsend, 2005) found out that a method that keeps the parameter set close to the boundary leads to the fast development of the Pareto front and an exploration close to the boundary. Other methods to enforce the constraints exhibit good performance on specific test functions, however, overall the truncation method allows for safe performance. This method also keeps the velocity from overshooting (Hassan et al., 2005). Thus, truncation is the preferred method for algorithm implementation for CTCR.

Another challenging aspect in particle swarm optimization is the selection of appropriate leaders, as this is based on neighborhood topologies. However, the appropriate selection of particle swarm variables (inertia weight, the influence of personal versus global best parameter set) can also cope with this problem to allow for a good exploration of the overall search space. Generally, a higher inertia rate η increases exploration and leads to a faster convergence, where the parameters c_1 and c_2 determine the self-confidence of a parameter set versus swarm confidence. Thus, the adequate selection of these parameters can tune the algorithm and result in an overall good performance.

There exist guidelines on the selection of population sizes (Coello Coello and Lechuga Salazar, 2002; Trelea, 2003). The authors in (Shi and Eberhart, 1999) find that population sizes are not important and have similar performance regarding $P = 20, 40, 80, 160$ particles. This can be interpreted as a feature of the algorithm and means that the performance is not sensitive to the initial population size. The authors in (Coello Coello and Lechuga Salazar, 2002) advise to select 20 to 80 particles.

Variable dimension is a feature to the general particle swarm optimization if the dimension of decision vectors is not known a priori. The velocity and position updates are more complex compared to general particle swarm optimization and require a higher computational effort but can enlarge the applicability of the algorithm.

As multiple objectives are important for the structural design optimization of CTCR, see Chapter 1, the following sections focus on the implementation of multiple objectives to particle swarm optimization.

3.5 MULTI-OBJECTIVE OPTIMIZATION

In multi-objective optimization there exist multiple solutions to the problem, as each solution to the problem represents a tradeoff between objectives. Thus, one aims to minimize or maximize more than one objective (quality measure).

Evolutionary algorithms are especially suited for these types of problems, as individuals can search through the overall parameter space and thus represent a large diversity, even if the boundaries of the parameter space are unknown. As evolu-

tionary algorithms are adaptable to multi-objective optimization problems, several optimization strategies have been proposed, the most prominent ones are (Simon, 2013)

- Non-dominated sorting genetic algorithm (NSGA)
  (Srinivas and Deb, 1994)

- Strength Pareto evolutionary algorithm (SPEA)
  (Zitzler, 1999)

- Improved strength Pareto evolutionary algorithm (SPEA2)
  (Zitzler, Laumanns, and Thiele, 2001)

- Multi-objective particle swarm optimization (MOPSO)
  (Coello Coello and Lechuga Salazar, 2002)

- Fast and elitist multi-objective genetic algorithm (NSGA-II)
  (Deb et al., 2002).

3.5.1 *Problem Definition*

The multi-objective optimization problem consists of multiple objectives o and can be formulated as

$$\text{minimize } \mathbf{y} = f(\mathbf{x}) = (f_1(\mathbf{x}), ..., f_o(\mathbf{x})),$$

with f_i being the objective functions and $i \in [1, ..., o]$. The following constraints apply

$$g_i(\mathbf{x}) = 0 \qquad\qquad h_i(\mathbf{x}) \leqslant 0 \qquad\qquad i \in \mathbb{N}\backslash 0,$$

where

$$\mathbf{x} = (x_1, x_2, ..., x_m) \in \mathcal{X}, \qquad\qquad \mathbf{y} = (y_1, y_2, ..., y_m) \in \mathcal{Y}.$$

$\mathbf{x}$ defines the decision vector in decision space $\mathcal{X}$ and $\mathbf{y}$ defines the objective vector in objective space $\mathcal{Y}$. $\mathbf{x} \in X_f$, where $X_f = \{\mathbf{x} \in X \,|\, g(\mathbf{x}) = 0, h(\mathbf{x}) \leqslant 0)\}$. Multi-objective optimization usually deals with the optimization of two to three objectives. If more than three objective functions require optimization, the problem is called many-objective (Fleming, Purshouse, and Lygoe, 2005).

3.5.2 *Pareto Dominance*

Pareto dominance describes a concept to balance the objectives against one another, which had a profound impact in multi-objective optimization (Tan, Khor, and Lee, 2005). It can also be defined as an optimality criterion and has been proposed by (Pareto, 1896). Decision vectors are evaluated against one another based on their objectives (quality). The term domination characterizes the elitism of one decision vector over the other (considering the minimization of objective functions):

A decision vector $\mathbf{x}$ **strictly dominates** another vector $\mathbf{x}^*$ ($\mathbf{x} \prec \mathbf{x}^*$), if $f_i(\mathbf{x}) \leqslant f_i(\mathbf{x}^*)$ $\forall i = 1...o$ and $f_i(\mathbf{x}) < f_i(\mathbf{x}^*)$ for some i. A decision vector $\mathbf{x}$ **weakly dominates** another vector $\mathbf{x}^*$ ($\mathbf{x} \preccurlyeq \mathbf{x}^*$), if $f_i(\mathbf{x}) \leqslant f_i(\mathbf{x}^*)$ for all i. A **non-dominated** vector $\mathbf{x}$ thus means, that there exists no $f_i(\mathbf{x}^*) \leqslant f_i(\mathbf{x})$ for all i.

3.5.3 *Pareto Optimality*

The set of different solutions in decision space $\mathcal{X}$ from the evaluation of the quality of objectives through tradeoffs is called the **Pareto optimal set** (Awad and Khanna, 2015). The Pareto optimal set $\mathcal{P}_s$ is defined by the set of non-dominated solutions and is thus defined as

$$\mathcal{P}_s = \{x \in X_f | x \text{ is Pareto optimal}\}.$$

This implies that the decision vector x is Pareto optimal within the feasible region X_f. The set of the non-dominated solutions defines the **Pareto front** $\mathcal{P}_f$ in objective space $\mathcal{Y}$ as

$$\mathcal{P}_f = \{f(x) \in \mathbb{R}^o | x \in \mathcal{P}_s\},$$

where o are the objectives. The Pareto optimal set of solutions also spans the Pareto front, as depicted in Figure 10 (left). The graph illustrates the set of solutions characterizing the Pareto front and the dominated solutions for the two objectives f_1 and f_2. The mapping from decision to objective space is represented by Figure 10 (right).
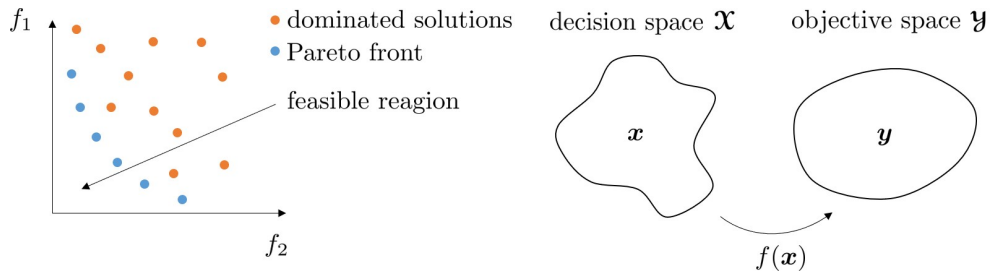
Figure 10: Dominated solutions and solutions on Pareto front (left) and mapping from decision space $\mathcal{X}$ to objective space $\mathcal{Y}$ (right).

3.5.4 *Characterization of Objectives*

Given a solution set $\mathcal{W}$, the objective functions are said to be **totally conflicting**, if there exist no two solution vectors x and x^*, where $(f_i(x) \prec f_i(x^*))$ or $(f_i(x^*) \prec f_i(x))$, $\forall i = 1...o$. This means that no objective function dominates the other and that the solution set already defines the Pareto optimal front. The objective functions are defined as **partially conflicting**, if any x or x^* exists, where $(f_i(x) \prec f_i(x^*))$ or $(f_i(x^*) \prec f_i(x))$ for some i. The objective functions are said to be **non-conflicting**, if there exists any x or x^*, where $(f_i(x) \prec f_i(x^*))$ or $(f_i(x^*) \prec f_i(x))$ for all i. In this case, the objective functions can be converted into one single objective, e.g. using a scalar, as the minimization or maximization of one of the objectives results in the minimization or maximization of the other (Tan, Khor, and Lee, 2005).

3.5.5 *Performance Measures*

To evaluate the quality of candidate solutions, there exist different performance measures. These are the **convergence** of the candidate solutions towards a Pareto optimal front, the **distribution** of candidate solutions over the search space and their coverage of the Pareto optimal region, and the **relative proximity** of the solution set to the set of Pareto optimal solutions (Awad and Khanna, 2015). However, a priori knowledge about the Pareto optimal region and the Pareto optimal front is required in most cases. Usually, the functionality of multi-objective optimization algorithms is evaluated using test functions, or the performance of the algorithms is evaluated against one another. A straight forward method to quantify the propagation of the Pareto front is measured by the number of solutions on the front and their spread (Reyes-Sierra and Coello Coello, 2006).

The following sections concentrate on multi-objective particle swarm optimization (MOPSO), originally proposed by (Moore and Chapman, 1999).

3.5.6 *Multi-Objective Particle Swarm Algorithm*

Particle swarm optimization is the general focus of this work and is selected over other evolutionary algorithms mentioned in this chapter. It proves to be computationally more efficient than other multi-objective evolutionary algorithms (Coello Coello and Lechuga Salazar, 2002; Hassan et al., 2005; Shi and Eberhart, 1999). Further, it is not sensitive to population size (Shi and Eberhart, 1999) and is thus especially suited for complex problems that require high computation times (as smaller population sizes can be selected). Here, it is assumed that computational effort is high for parameter optimization of CTCR as nonlinear differential equations need to be solved for kinematic modeling. Another advantage is that decision vectors can be of variable dimension if utilizing a variable dimension approach. This enables applicability to a larger domain of problems. Further, the algorithm has been shown to offer better convergence for complex objective functions dependent on multiple variables (Ramezan Shirazi, Seyyed Fakhrabadi, and Ghanbari, 2014).

Multi-objective particle swarm optimization was first introduced by (Moore and Chapman, 1999). The presented algorithm is fundamentally related to general particle swarm optimization. In single-objective particle swarm optimization, the objective is evaluated based on its value. This is not possible for multi-objective optimization problems, such that researchers proposed various methods for handling objectives. It is especially complex if objectives are conflicting. Conflicting objective functions refer to the existence of multiple solutions to the problem (Reyes-Sierra and Coello Coello, 2006). As f contains multiple objectives, minimization or maximization of f cannot result in finding a global solution if f contains objectives that are conflicting (Awad and Khanna, 2015).

If an optimization problem is defined by multiple objectives, there exist various approaches for decision making and thus selection of leaders within a swarm. The concepts for objective function handling can be divided into weighted aggregation, population, and Pareto optimality concepts. However, there exists a large variety of

approaches (also combinations of the aforementioned), such that this section only gives a broad overview.

Aggregation Methods combine all objectives and the multi-objective problem is converted into a single objective problem (Ramezan Shirazi, Seyyed Fakhrabadi, and Ghanbari, 2014). Most of these optimization strategies consider a weighted sum approach, where each of the objectives is assigned a different weight as

$$y = \sum_{i=1}^{o} \lambda_i f_i(x) \text{ for } \lambda_o > 0 \text{ and } \sum_{i=1}^{o} \lambda_i = 1,$$

where λ_i define the weights for each objective o. By varying the weights, multiple solutions can be acquired through the algorithm. Usually, the weights are predefined based on the performance of the optimization algorithm. There exist also those concepts that consider a weight change during optimization, using either linear or dynamic aggregating functions (Parsopoulos and Vrahatis, 2002; Ramezan Shirazi, Seyyed Fakhrabadi, and Ghanbari, 2014). Weighted Aggregation Concepts are suited for optimization problems that contain non-conflicting objectives.

Population Methods divide the overall swarm into subpopulations, where each of the subpopulations handles the optimization of a single objective (Chow and Tsui, 2004) such there exist parallel evaluated swarms (Parsopoulos, Tasoulis, and Vrahatis, 2004). If a problem consists of o objectives, then the algorithm is composed of o sub swarms. The sub swarms are combined for solution selection. These type of methods are susceptible to find extreme solutions but do not determine a large variety of different solutions on the Pareto front (Awad and Khanna, 2015).

Pareto Dominance Methods are especially suited for those optimization problems with conflicting objectives (Alvarez-Benitez, Everson, and Fieldsend, 2005). These types of methods utilize the domination principle that some solutions dominate others and base the leader selection on this concept.

3.6 SUMMARY AND CONCLUSION

Aggregation methods are only suitable if objectives are non-conflicting. They can be used if weights are selected appropriately. Population methods may be restricted in generating the true Pareto front and Pareto dominance methods are key if objectives are conflicting or are represented by different units. They are thus the key concept of this thesis.

However, leader selection using Pareto dominance methods is different from general particle swarm and more challenging for this type of optimization, as this incorporates the handling of the non-dominated solutions. Pareto dominance methods usually generate an archive as a repository to store the non-dominated solutions (Reyes-Sierra and Coello Coello, 2006).

The performance in multi-objective optimization is not as straightforward to measure. Usually, the convergence of the algorithm is the key parameter that is used to

forecast when the objective function converges towards a specific value. This principle cannot be used as a measure for the domination principle. The true Pareto front is usually not known a priori, and the performance is usually measured by the stagnation of the solutions on the front.

Besides other advantages, evolutionary optimization algorithms seem suitable for the structural design optimization of CTCR, as they can handle multiple objectives. Particle swarm optimization is one prominent example of evolutionary algorithms. Note, that other evolutionary algorithms might be suitable for the design optimization of CTCR, however, this thesis specifically investigates the applicability of multi-objective particle swarm optimization.

4

OPTIMIZATION ALGORITHMS IN ROBOTICS

This chapter presents an overview of optimization algorithms targeting the design of robots and specifically identifies parameters, objectives, and optimization methods for existing robotic optimization problems. The optimization of parallel, hyper-redundant, and continuum robots (especially soft continuum robots) has been of research interest. In the early stages of optimization algorithms and robotics, researchers targeted the design optimization of serial robots. The state of the art presented here focuses on the optimization of design parameters of various robots - not the optimization of configuration-specific parameters, or motions.

4.1 PARAMETERS

Most optimization parameters in robotic applications consider the structure and/or geometrical design of the specific robot type. These are, for instance, joint distances and angles for serial robots that are composed out of several rigid links and joints (Coello Coello, Christiansen, and Aguirre Hernándes, 1998). The length of links and the configuration of joints is adaptable and characterizes the overall workspace of a robot (Siciliano and Khatib, 2008). An example serial robot is depicted in Figure 11 (left). Even though the parameters of serial robots can be manually tuned for the structural synthesis in most cases, researchers tested the performance of optimization algorithms (Chocron, 2008; Coello Coello, Christiansen, and Aguirre Hernándes, 1998; Khatami and Sassani, 2002; Kumar et al., 2014; Paredis and Khosla, 1993; Stocco, Salcudean, and Sassani, 1998). However, if the diversity of the design parameters is large, design optimization algorithms represent a tool to design the robot according to specific constraints or regarding multiple criteria.

As serial grippers are composed out of various links and joints, their structural design is of research interest (Ciocarlie and Allen, 2010; Datta, Pradhan, and Bhattacharya, 2016; Rao and Waghmare, 2015). The optimization parameters of an example gripper, depicted in Figure 11 (right), are the three geometrical lengths and one joint angle (Datta, Pradhan, and Bhattacharya, 2016).

If two or more serial arms are connected to one end-effector, the system is by definition a parallel robot (Siciliano and Khatib, 2008). The design of such robots is more complex than a single serial chain, as the chains of the parallel structure depend on one another. First research dealt with the structural design optimization of parallel robotic mechanisms and platforms for better performance (Hao and Merlet, 2005; H. S. Kim and Tsai, 2003; Kurtz and Hayward, 1992; Stock and Miller, 2003). Planar mechanisms require design optimization algorithms for structural design synthesis, especially three-dimensional mechanisms, as they can be defined by various parameters. The authors in (Shin et al., 2013) optimize a planar mechanism, as illustrated in Figure 12 (left), and consider the mechanism's kinematic parameters (configurations and lengths of links) for optimization. (Hao and Merlet, 2005) optimize the geometri-
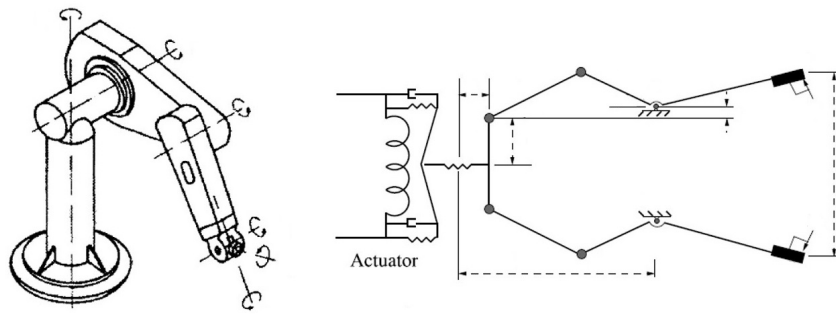
Figure 11: Serial robot (left) (reprinted from (Coello Coello, Christiansen, and Aguirre Hernándes, 1998), © 1998, with kind permission from Cambridge University Press) and robotic gripper (right) (reprinted from (Datta, Pradhan, and Bhattacharya, 2016), © 2016 IEEE).
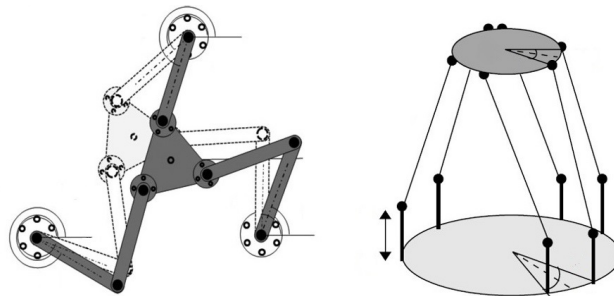
Figure 12: 2DOF planar parallel robot (left) (reprinted from (Shin et al., 2013), © 2013 IEEE) and a parallel robotic mechanism (right) (reprinted from (Hao and Merlet, 2005), © 2005, with kind permission from Elsevier).

cal parameters of a mobile platform connected to six legs by ball joints, as illustrated in Figure 12 (right), and (Ramezan Shirazi, Seyyed Fakhrabadi, and Ghanbari, 2014) determine optimal lengths and joint angles of a parallel robot manipulator. A different parallel robot is depicted in Figure 13 (left), which shows a four cable-driven parallel manipulator for a spherical radio telescope. This mechanism requires the optimization of three geometrical parameters. The optimization parameters of the parallel ankle rehabilitation robot, as illustrated in Figure 13 (right), are also joint connections and distances (Jamwal, Xie, and Aw, 2009).

Hyper-redundant robots are defined by their large number of actuatable DOF, such that the robot has more DOF than are needed to execute a task (Chirikjian and Burdick, 1994). They can be composed out of various materials and actuators, including many rigid links and joints, but also softer materials. Design parameters of the hyper-redundant robot, illustrated in Figure 14 (left), include the number, length, and configuration of soft modules (Trivedi, Dienno, and Rahn, 2008). A similar robot is considered in (Bodily, Allen, and Killpack, 2017), see Figure 14 (middle), and optimization parameters include the mounting height and angle, and link lengths. The authors in (Tesch, Schneider, and Choset, 2013) aim to optimize the gait parameters for the sidewinding of a robotic snake, as depicted in Figure 14 (right). Continuum robots are a type of robot, where the number of DOF converges towards infinity
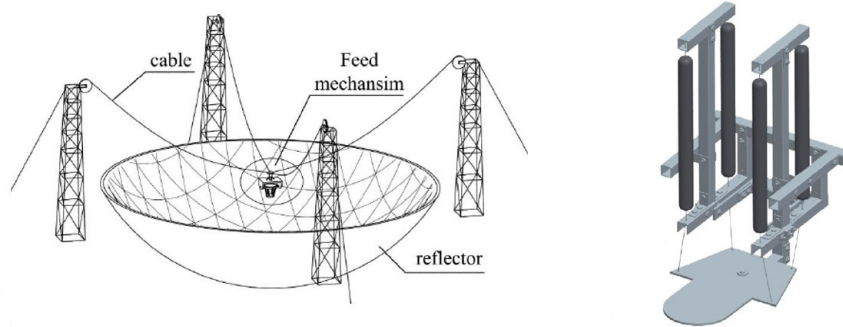
Figure 13: Four cable driven parallel manipulator for a spherical radio telescope (left) (reprinted from (Yao et al., 2010), © 2010 IEEE) and parallel ankle rehabilitation robot (right) (reprinted from (Jamwal, Xie, and Aw, 2009), © 2009, with kind permission from Elsevier).

Figure 14: OctArm (left) (reprinted from (Trivedi, Dienno, and Rahn, 2008), © 2008, with kind permission from ASME), a soft pneumatic robot (middle) (reprinted from (Bodily, Allen, and Killpack, 2017), © 2017 IEEE), and snake robots (right) (reprinted from (Tesch, Schneider, and Choset, 2013), © 2013 IEEE).

(Robinson and Davies, 1999). Continuum robots can be classified mainly into soft, tendon-actuated, and concentric-tube continuum robots.

One example case for a soft continuum robot is depicted in Figure 15 (left). The optimization parameters for this particular mechanism, are the chamber thickness, position, and outer and inner radius of a soft module (Runge, Peters, and Raatz, 2017). A tendon-actuated robotic design is depicted in Figure 15 (right). The design optimization parameters for the particular robot are the overall robot length and the difference in section length of the three-segment tendon-actuated robot to the right (Ouyang, Liu, and Sun, 2016).

It is noticeable that most optimization problems in the state of the art for robotics are defined by few parameters (usually around two to five). In contrast to that, the CTCR optimization problem requires to solve for a higher number of parameters and many constraints (that arise from the constraint configuration space, CTCR geometry, and tube dependencies), which results in higher complexity of the problem.
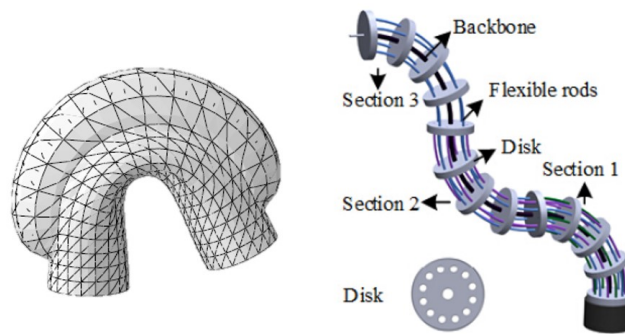
Figure 15: A soft module (left) (reprinted from (Runge, Peters, and Raatz, 2017), © 2017 IEEE) and a tendon-actuated continuum robot composed out of three segments (right) (reprinted from (Ouyang, Liu, and Sun, 2016), © 2016 IEEE).

4.2 OBJECTIVES

Prominent examples of objective functions depend on the specific robot type but some of them are applicable in general. These include, but are not limited to, the workspace, singularities, dexterity, accuracy, stiffness, and other kinematic and dynamic performance measures.

The authors in (Hao and Merlet, 2005) optimize the workspace and accuracy of a three-dimensional mobile platform. Other workspace-specific characteristics are singularities and dexterity, which are considered for a parallel robot by (Ramezan Shirazi, Seyyed Fakhrabadi, and Ghanbari, 2014) and a hyper-redundant robot by (Bodily, Allen, and Killpack, 2017; Trivedi, Dienno, and Rahn, 2008). The authors in (Shin et al., 2013) aim to maximize the stiffness of a planar mobile platform, such that objectives include the determinant and inverse of the condition number of the stiffness matrix. The dynamic performance of a planar robot is considered in (Song et al., 2017). Kinematic performance criteria represent objectives in (Kelaiaia, Company, and Zaatri, 2012) for the design optimization of a linear Delta parallel robot. Specific kinematic performance indices include the isotropy index and global dynamic index that are accounted for by (Unal, Kiziltas, and Patoglu, 2008) for a 2DOF parallel mechanism. Another characteristic is the global condition number of the Jacobian matrix that is mentioned by (Jamwal, Xie, and Aw, 2009) to optimize the design of a parallel ankle rehabilitation robot.

Robot-specific objectives are, for instance, the torques and reaction forces at the joints of serial robots (Coello Coello, Christiansen, and Aguirre Hernándes, 1998), the gripping forces and force transmission rations of serial grippers (Datta, Pradhan, and Bhattacharya, 2016), the cable tension and stiffness for cable-driven parallel manipulators (Yao et al., 2010), the head stability and speed of a hyper-redundant snake (Tesch, Schneider, and Choset, 2013), the load capacity for a specific actuation pressure of the Oct Arm (Trivedi, Dienno, and Rahn, 2008), the load capabilities of a hyper-redundant robot (Bodily, Allen, and Killpack, 2017), and maximum anatomical visibility for the design of a parallel mechanism for minimally invasive surgery (Kuntz, Bowen, et al., 2018).

4.3 SINGLE-OBJECTIVE OPTIMIZATION

Single-objective optimization problems in robotics have been treated with many different optimization algorithms in the past. Those optimization problems, which are rather simple (not defined by various optimization parameters and constraints) can utilize iterative methods, as in (Shin et al., 2013), where the authors chose an iterative method to maximize the stiffness of a planar mechanism. The selected type of algorithm is also constrained by the kinematic model of the robotic structure. For those mechanisms, where the kinematic model can be solved analytically, various types of optimization algorithms can be applied.

Least-squares optimization belongs to the class of local optimization algorithms. It is gradient-based and there exist those methods that apply to linear functions and those that can handle nonlinearity. Those robotic mechanisms that utilize nonlinear kinematic models, require the use of nonlinear optimization algorithms. (Connolly, Walsh, and Bertoldi, 2017) optimize the design of multiple fluidic powered fibers reinforced actuators to follow a specific trajectory utilizing an analytical nonlinear elasticity model. Simple least-squares optimization minimizes a scalar error metric regarding bending angles, segment lengths, and pressures. The authors in (Ouyang, Liu, and Sun, 2016) utilize a nonlinear optimization algorithm (Nelder-Mead) to optimize the workspace of a tendon-actuated continuum robot composed out of three segments, considering the robot's length and the difference in section length.

Heuristic algorithms are suited for nonlinear problems with higher complexity and multiple constraints, as they are more likely to find a global optimum. Evolutionary algorithms are prominent nonlinear global optimization algorithms, and this is the reasoning for their appearance in many robotic applications.

Particle swarm optimization, belonging to the class of evolutionary algorithms, is applied to workspace and accuracy optimization of a parallel robot manipulator in (Ramezan Shirazi, Seyyed Fakhrabadi, and Ghanbari, 2014).

Genetic algorithms are further prominent examples of evolutionary algorithms that have been applied to various robotic optimization problems. (Jamwal, Xie, and Aw, 2009) use a genetic algorithm to optimize the design parameters of a parallel ankle rehabilitation robot. This includes the optimization of joint connections and geometrical distances. The objective of the algorithm considers the global condition number of the Jacobian matrix for optimal performance. (Hiller and Lipson, 2012) utilize an evolutionary algorithm to design a soft robot using volumetric expanding materials such that an automatic design for free form snakes can be developed, and (Runge, Peters, and Raatz, 2017) use the same methodology to optimize the geometrical parameters of a soft module, combining finite element analysis and constant curvature modeling.

Simulated annealing is another heuristic-based algorithm and is applied by (Kuntz, Bowen, et al., 2018) to optimize the design of a parallel mechanism for maximum anatomical visibility under the consideration of motion planning and utilizes adaptive simulated annealing for optimization.

The authors in (Lou et al., 2014) compare different methods for design optimization of parallel robots, including sequential quadratic programming, controlled random search, genetic algorithm, differential evolution, and particle swarm optimiza-

tion. Results show that sequential quadratic programming is suitable for simple robot designs and genetic algorithms, as well as particle swarm optimization, for all problems with many constraints.

4.4 MULTI-OBJECTIVE OPTIMIZATION

Multi-objective optimization approaches are prominent in robotics, as most applications depend on multiple objective functions. If objectives are non-conflicting, weighted methods are suitable to find an overall optimum regarding all objectives. If objectives are conflicting, then Pareto-based approaches represent a helpful tool to determine a parameter set that represents a tradeoff between the objectives. However, some works also utilize weighted methods for conflicting objective functions. This is not advisable, as the minimization of one objective function does not result in the minimization of the others.

4.4.1 *Weighted Methods*

Weighted methods include normalized weighted objective functions, where multiple objectives are represented by a scalar objective. The selection of weights, however, can be a challenge and is usually done empirically.

The authors in (Rao and Waghmare, 2015) utilize this method to implement five different objective functions for configuration optimization of a serial gripper. (Song et al., 2017) consider the use of a scalar error metric for optimization and determine a weighted sum objective, based on dynamic performance and manufacturing cost. The authors apply hybrid particle swarm optimization to optimize the structural parameters of their planar robot.

An iterative method is applied to optimize for stiffness and cable tension of a four cable-driven parallel manipulator for a spherical radio telescope (Yao et al., 2010). The objectives are not conflicting in this case and a method that considers both objectives in one error metric is an appropriate choice.

(Zhang et al., 2010) propose a design optimization algorithm for a 2DOF tendon-actuated module. The authors optimize the stiffness and an increased workspace volume. A weighted method may not be the preferred algorithm as stiffness and workspace volume are conflicting. This is the reason why weighted methods are not the first choice for multi-objective optimization problems.

4.4.2 *Pareto Optimality Methods*

Pareto optimality methods are commonly used in robotics and have been implemented early on. Especially evolutionary algorithms are prominent examples, as they can be easily adapted from single to multiple objectives. A genetic algorithm, for instance, is applied to multi-objective design optimization of a serial robot by (Coello Coello, Christiansen, and Aguirre Hernándes, 1998).

Multi-objective genetic algorithms are applied to determine gripping forces and an optimal force transmission ratio for a serial gripper (Datta, Pradhan, and Bhat-

tacharya, 2016). They are also utilized by (Bodily, Allen, and Killpack, 2017) to optimize the dexterity and load bearing of a hyper-redundant robot to compute a set of Pareto optimal solutions, and by (Kelaiaia, Company, and Zaatri, 2012) for a linear Delta parallel robot that should be designed in a way to have improved kinematic and dynamic performance, high stiffness, and a large workspace. All aforementioned objectives are conflicting, such that the use of Pareto optimality is suitable.

The authors in (Unal, Kiziltas, and Patoglu, 2008) consider multi-objective design optimization of a 2DOF parallel mechanism. They formulate their algorithm in a general manner considering Pareto optimality to optimize geometrical measures.

(Tesch, Schneider, and Choset, 2013) propose another multi-objective optimization strategy. The authors aim to improve the locomotive capabilities of snake robots, considering the head stability and speed of the snake. Again, these objectives are in conflict and Pareto optimality applies. The authors investigate two different optimization algorithms, where their algorithm (considering Pareto optimality) shows improved performance.

4.5 OPTIMIZATION FOR CONCENTRIC TUBE CONTINUUM ROBOTS

Researchers consider the design of CTCR for various applications and optimize CTCR parameters for neurosurgery (Anor, Madsen, and Dupont, 2011; Bedell et al., 2011; Bergeles, Gosline, et al., 2015; Boushaki et al., 2016), bronchoscopy (Torres, Webster III, and Alterovitz, 2012), endonasal surgery (Burgner, Gilbert, and Webster III, 2013), intracardiac surgery (Bergeles, Gosline, et al., 2015), cochlear implant insertion (Granna, Rau, et al., 2016), and transforamenal hippocampotomy (Gilbert, Neimat, and Webster III, 2015; Hendrick, Mitchell, et al., 2015). Figure 16 depicts a CTCR for bronchoscopy, CTCR configurations within the ventrical system of the brain (Bergeles, Gosline, et al., 2015), and helical tubes for follow-the-leader motion within the hippocampus in the brain (Gilbert, Neimat, and Webster III, 2015).

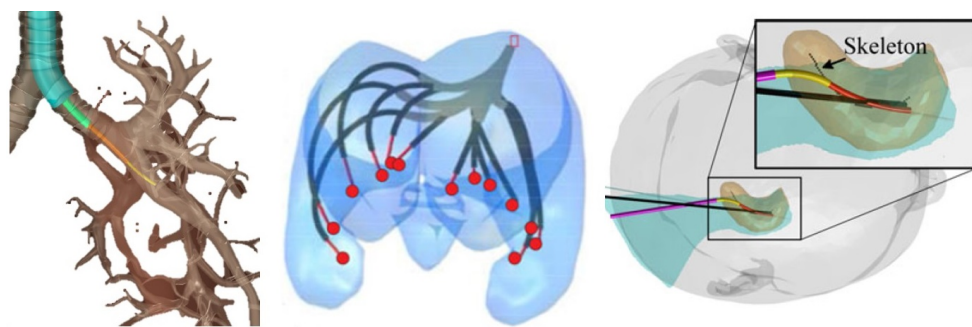Figure 16: CTCR robotic designs in the bronchial tubes of the lung (left) (reprinted from (Torres, Webster III, and Alterovitz, 2012), © 2012 IEEE), in the ventrical system within the brain (middle) (reprinted from (Bergeles, Gosline, et al., 2015), © 2015 IEEE), and helical tubes for follow-the-leader motion within the hippocampus in the brain (right) (reprinted from (Gilbert, Neimat, and Webster III, 2015), © 2015 IEEE).

4.5.1 *Parameters*

CTCR are defined by multiple design parameters (number of tubes, lengths, diameters, wall thickness, curvature, stiffness, material properties). The parameters considered so far by the state of the art are the tube lengths and curvatures as in (Anor, Madsen, and Dupont, 2011; Baykal, Torres, and Alterovitz, 2015; Bedell et al., 2011; Bergeles, Gosline, et al., 2015; Boushaki et al., 2016; Burgner, Gilbert, and Webster III, 2013; Torres, Webster III, and Alterovitz, 2012) for a CTCR composed of three tubes and constant curvature made from the shape memory alloy NiTi.

The authors in (Ha, Park, and Dupont, 2017) consider a non-constant curvature function and optimize the precurvature of each tube. The design of a plastic tube for a 4DOF tube robot is considered by (Noh et al., 2016). It includes the optimization of the straight and curved section length and curvature of the inner tube in two-dimensional space. Helically shaped tubes are optimized by (Comber et al., 2016). The specific application regards the optimization of length, curvature, and torsion of one helical precurved tube and the length of an ablation probe.

4.5.2 *Objectives*

Various objective functions have been proposed in the past that depend on the intended application. These include task and anatomical constraints to reach the desired goal region (Anor, Madsen, and Dupont, 2011; Bedell et al., 2011; Torres, Webster III, and Alterovitz, 2012), to maximize the reachable space (Baykal, Torres, and Alterovitz, 2015) or target points by the CTCR's end-effector (Bergeles, Gosline, et al., 2015). The authors in (Burgner, Gilbert, and Webster III, 2013) incorporate a volume-based objective that defines the number of reachable voxels within the target area, and (Noh et al., 2016) consider the uncovered surface of the target volume as the objective function.

A different approach is taken by (Boushaki et al., 2016; Ha, Park, and Dupont, 2017), who regard the elastic stability of the tubes. (Boushaki et al., 2016) additionally consider reachability and tip trajectory smoothness. The authors in (Gilbert, Neimat, and Webster III, 2015) optimize helical tubes for follow-the-leader deployment along a specific path, where the objective function minimizes the distance of the robot backbone towards the path. The objective function in (Hendrick, Gilbert, and Webster III, 2015b) describes the optimal overlap between the camera and robot workspace.

4.5.3 *State of the Art of Optimization Algorithms for CTCR*

Designing a CTCR for a specific application results in an infinite number of possible combinations. Further, workspace determination is not intuitive, due to the complex interaction of the tubes. This makes it impossible to select a design manually and the utilization of CTCR is not possible without the design optimization of the tubes. Thus, researchers proposed the use of various optimization algorithms.

4.5.3.1 *Single-Objective*

Most optimization algorithms that have been proposed in the context of parameter optimization of CTCR are single-objective and use one single error metric for optimization. First work utilized simple kinematic models for CTCR that describe the three-dimensional shape of the robot using a geometrical approach. Further, most optimization approaches utilize unconstrained optimization algorithms, which are not suitable for all CTCR applications, as constraints can be important. These arise from the configurational and geometrical dependencies between the tubes, as well as from the task or anatomy.

Other work included additional constraints into the design optimization procedure, such as motion planning, obstacles, and elastic stability. (Torres, Webster III, and Alterovitz, 2012) are the first to consider motion planning within the design optimization utilizing a sampling-based motion planning approach. This allows the final robot design to safely navigate through the lung considering obstacles. A heuristic approach performs an exhaustive search over the parameter space to determine optimal parameters. The design space consists of tube lengths and curvatures.

In (Burgner, Gilbert, and Webster III, 2013) the authors apply the Nelder-Mead algorithm for the optimization of tube length and curvatures to cover a tumor volume. The authors utilize a volume-based objective that defines the number of reachable voxels within the target area. Here, the authors utilize Cosserat rod theory to compute the single objective.

(Baykal, Torres, and Alterovitz, 2015) continue the work by (Torres, Webster III, and Alterovitz, 2012) and combine design optimization and motion planning into one problem to determine tube sets to maximize the reachable space represented by a single objective. Global optimization and sampling-based motion planner are utilized together to avoid obstacles to steer into the lung. Here, lengths and tube curvatures are considered using adaptive simulated annealing (a heuristic approach) and rapidly exploring random trees for motion planning. The authors extended their work to the kinematic design optimization of general robotic structures using motion planning in (Baykal, Bowen, and Alterovitz, 2018).

(Hendrick, Gilbert, and Webster III, 2015b) optimize tube parameters of two collaborative robotic arms to achieve an optimal camera overlapping workspace such that the endoscopic field view and the view of the workspace are aligned. Here, the authors optimize the curvature of the inner tube using a brute force method and determine the CTCR workspace using simple geometry.

The authors in (Noh et al., 2016) consider a very special case of a CTCR and optimize the design of a plastic tube for a 4DOF tube robot utilizing a geometric model and a scalar error metric for optimization. As mentioned above, they utilize an unconstrained optimization technique using a derivative-free method (Nelder-Mead simplex algorithm). This type of algorithm is generally suited for nonlinear problems with multiple parameters and can thus handle nonlinear kinematic models.

The authors in (Ha, Park, and Dupont, 2017) consider the elastic stability of the tubes such that the sudden release of energy can be prevented. While prior methods considered tubes with piecewise constant curvature, the authors consider a non-constant curvature function and optimize the tube's precurvature using the steepest

descent method (a local gradient-based approach) to numerically solve the optimization problem.

4.5.3.2 *Multi-Objective*

Multi-objective optimization for CTCR is covered by researchers in the sense of multiple weighted scalar error metrics that are combined into one single objective. This includes work by (Anor, Madsen, and Dupont, 2011), who propose a global pattern search algorithm to determine optimal tube parameters for neurosurgery considering multiple target points based on patient anatomy. The pattern search is further developed by (Bedell et al., 2011) to minimize the length and curvature of all tube sections while minimizing a single objective function and considering task and anatomical constraints based on patient anatomy. A pattern search is a gradient-free numerical optimization approach and not suited for complex parameter optimization of CTCR.

An optimization framework is presented by (Bergeles, Gosline, et al., 2015) considering task and anatomical constraints for the deployment of CTCR and optimizes for a maximum set of reachable points. Here, path planning is also considered using a simplified kinematic model by computing intermediate configurations towards a goal. A Nelder-Mead optimization is utilized to minimize a cost function composed out of multiple scalar error metrics.

Multi-objective optimization is introduced by (Boushaki et al., 2016) using a Pareto grid searching approach to optimize reachability and elastic stability considering tip trajectory smoothness. Optimized parameters are tube's curvature and lengths, where other tube parameters are selected a priori. However, here the objectives are not necessarily conflicting, as high reachability does not inevitably result in low elastic stability. So far, this is the only work that considers multi-objective optimization utilizing Pareto dominance concepts that are suited to treat problems with conflicting objectives.

4.6 CONCLUSION

This chapter presented key parameters and objectives in robotic applications. Considering different robotic structures, parameters for optimization are mainly concerned with their geometrical dimensions. The dimension of the parameter space is small compared to CTCR and optimization parameters usually vary between two to five. The geometrical structure of CTCR is complex due to many geometrical parameters of each tube. This implies that the constrained space for CTCR also increases in complexity, as constraints are dependent on the parameter space. Further, the selection of material dependent parameters is not a priori for CTCR, as the selected material influences the stiffness and the elastic interaction of the tubes. Thus, CTCR optimization parameters are geometric and material dependent, which increases the overall complexity of the optimization problem.

Considering the state of the art for CTCR optimization, the overall set of parameters is yet to be considered regarding their multidimensional parameter space. Also, forces and material parameters are not being considered within the optimization

methodology thus far. While the kinematics for most robotic types can be solved analytically, the modeling for CTCR requires complex elasticity theory. Early research considered simplified kinematic models and applied optimization algorithms that are limited to linear functions or do not regard constraints.

Objectives in other robotic applications include the workspace, dexterity, accuracy, stiffness, and other kinematic and dynamic performance measures. Even though these measures can be applied to CTCR optimization, the objective functions are different for the use of CTCR in minimally invasive surgery and most of the presented optimization algorithms have been applied outside of medicine. The application of optimization algorithms to other robotic systems in minimally invasive surgery is still relatively small, such that objective functions have to be formulated for the intended medical applications of CTCR.

Considering the structural optimization of other robotic types, researchers employed global optimization algorithms and heuristic approaches for complex structures and a large parameter set. Parameters for optimization mostly include structural design but also kinematic parameters. The utilization of multi-objective optimization algorithms utilizing Pareto dominance approaches is prominent for other robotic applications. These optimization algorithms have yet to be applied to the structural design optimization of CTCR for conflicting objectives.

Existing optimization algorithms for CTCR considered scalar error metrics and not conflicting objectives. Weights of weighted objectives are selected empirically, which are prone to result in different outcomes.

To conclude, this thesis aims to classify the optimization parameter space for CTCR and formulates objective functions for their use in minimally invasive surgery. As evolutionary and Pareto dominance concepts have proven their performance for various other robotic applications, their use for the structural design optimization of CTCR is the scope of this thesis and particularly particle swarm optimization is investigated. This further implies the consideration of heterogeneous objective functions that are represented by different units.

Part II

METHODS

5

PARAMETER OPTIMIZATION METHODOLOGY FOR CONCENTRIC TUBE CONTINUUM ROBOTS

This chapter describes the general optimization problem for CTCR. It presents the optimization workflow for different medical applications and describes the procedure of data processing of medical images, which is essential before optimization. The optimization problem for CTCR is then classified into different sub-categories. This includes the identification of parameters to be optimized, definition of objectives, and constraints. Lastly, this chapter presents the algorithmic implementation approach that utilizes a multi-objective particle swarm optimization algorithm with variable dimension to solve for optimal parameters of the optimization problem.

In parts within:

Granna, J., Godage, I.S., Wirz, R., Weaver, K.D., Webster III, R.J., & Burgner-Kahrs, J. (2016). A 3D Volume Coverage Path Planning Algorithm with Application to Intracerebral Hemorrhage Evacuation, *IEEE Robotics and Automation Letters*

Granna, J., Guo, Y., Weaver, & Burgner-Kahrs, J. (2016). Comparison of Optimization Algorithms for a Tubular Aspiration Robot for Maximum Coverage in Intracerebral Hemorrhage Evacuation, *Journal of Medical Robotics Research*

5.1 PROBLEM DEFINITION AND OVERVIEW

As the design space of CTCR is multidimensional, appropriate design parameters for an application, anatomy, or to execute a medical task must be determined through a design optimization procedure utilizing specific algorithms. The parameter space is constrained as design-, as well as application-specific parameters, impose constraints. Additionally, the kinematic model for CTCR is highly non-linear, such that only non-linear optimization methods can be utilized to solve the optimization problem. The overall constrained search space for CTCR can be envisioned as a space with multiple "islands" that represent the feasible space $\mathbf{X}_f$. In the search for an optimum, the decision vector would have to be adapted, such that it "jumps" from one island to the other to remain within the feasible space, see Figure 17. This type of optimization problem demands a specific algorithm that can handle such problems.
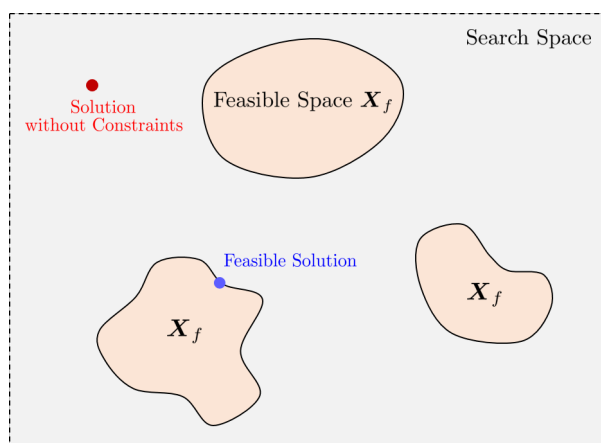

Figure 17: The overall search space of the optimization problem is represented by the gray box, the feasible region $\mathbf{X}_f$ is marked in light orange, a solution without constraints is illustrated in red, and feasible solution considering the constraints in blue.

The contribution of this chapter is the formulation of the structural design optimization problem for CTCR and describes the optimization methodology proposed in this work.

It further presents data representation methods, which are required to account for different patient datasets and applications. The optimization problem and methodology presented here thus has the potential to be adapted to different applications. This thesis targets CTCR applications by the state of the art (neurosurgery, intracerebral hemorrhage evacuation, endonasal surgery, cochlear implant insertion, intracardiac surgery, bronchoscopy, and transforaminal hippocampotomy) and those that are investigated in the scope of this thesis (cooperative task deployment, structural stiffness optimization, and laser-induced thermal therapy). This thesis assumes that CTCR are beneficial to those minimally invasive procedures.

This chapter aims to classify the optimization problem and describes different parameters, objectives, and constraints that define the design- and application-specific optimization problem of CTCR for the targeted applications. The description of the parameter space should thus hold for the entirety of design parameters (number, ma-

terial, curved and straight section length, outer and inner diameter, and curvature). The definition of application-specific parameters is also included in the scope of this chapter.

Lastly, this chapter proposes to utilize multi-objective particle swarm optimization to handle the structural design optimization problem of CTCR regarding multiple objectives and presents the implementation of the algorithm. It is thus structured as follows:

1. Optimization Workflow,

2. Data Representation,

3. Kinematic and Performance Measures,

4. Classification of parameters, objectives, and constraints, and

5. Algorithmic implementation.

5.2 OPTIMIZATION WORKFLOW

Figure 18 illustrates the optimization workflow, which is characterized by three main blocks. The first block represents the preallocation of parameters, objectives, and constraints, as well as the input of medical image data to the optimization procedure. The optimization algorithm requires the definition of objectives, either single or multiple. Robot- and application-specific constraints have to be defined by the user. Further, the use of patient-specific medical image data within the optimization algorithm requires a certain representation for further computation and the definition of the trajectory towards a goal, as well as the alignment of coordinate systems.

The main block illustrates the optimization process, which considers both robot- and application-specific parameter optimization. To compute the objective functions during the execution of the algorithm, kinematic modeling and motion planning algorithms can be utilized. Note, that motion planning algorithms are not considered in the scope of this thesis, but can be included in the design optimization process, if required. The output of the algorithm is then the quality of the optimization and one or multiple parameter sets. If the optimization problem is defined by multiple objectives, a Pareto optimal set of solutions is the output of the algorithm and a solution must be selected from the front either manually or automatically.

Generally, the optimization of design- and application-specific parameters can be divided, such that subsequent optimization strategies are applied, and the outcome of the prior optimization is the input to the proximate optimization. This concept is illustrated by the dashed lines in Figure 18.

5.3 DATA REPRESENTATION

If the aim is to optimize the CTCR for a medical application, task, or scenario, then the optimization procedure requires certain data structures as input to the optimization workflow. The data can be acquired through medical images (e.g. from CT, MRT or ultrasound) to
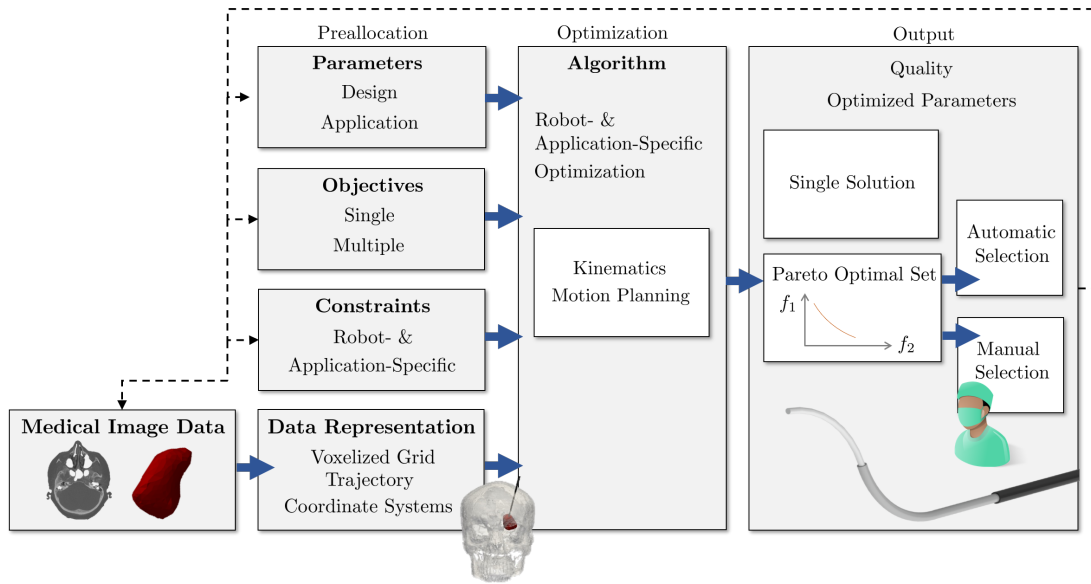
Figure 18: Optimization workflow with preallocation of inputs, optimization, and output.

- generate a voxelized grid representation to describe a target volume or obstacles,

- compute a trajectory towards a target,

- transform the surgical workspace into the robot coordinate system, and

- include a safety margin into the optimization procedure.

This data processing represents the basis for the optimization process such that the CTCR can be specifically optimized for a medical procedure or a patient. Anatomical related constraints can also be acquired from medical image data.

5.3.1 *Voxelized Grid Representation*

Medical image data is input to the optimization procedure. This requires a specific data representation for further computation purpose. Medical images usually come from CT or MRI images. Manual or semi-automatic segmentation of the specified volume using a threshold identifies all voxels within a specified range. The segmented 3D volume (using e.g. 3D slicer) can be exported as a surface dataset G_S (e.g. into Matlab), which is represented by its surface points and can be non-convex. The volume can represent the overall surgical workspace (including obstacles) or a single volume.

5.3.1.1 *Single Volume*

The surface dataset is then converted into a voxelized grid G_V through voxelization of the volume with an isotropic voxel size v_s (in mm and should be selected based

on the size of the end-effector to cover a single voxel). Different surface datasets (representing tumor volumes) segmented from CT image data are depicted in Figure 19 (left) as an example. The extent of G_V in x, y, and z-direction is defined by

$$\frac{|x_{max} - x_{min}|}{v_s} \times \frac{|y_{max} - y_{min}|}{v_s} \times \frac{|z_{max} - z_{min}|}{v_s},$$

with the origin at $\mathbf{o}_V = [x_{min} \, y_{min} \, z_{min}]^T$ and $|x_{max} - x_{min}|, |y_{max} - y_{min}|, |z_{max} - z_{min}|$ being the extent of the surface data points in x, y, z-direction. A voxel containing a surface data point, or enclosed by the surface is set to $G_V(i, j, k) = 1$ and a voxel outside the volume is set to $G_V(i, j, k) = 0$. i, j, k refer to the voxel with $i = \frac{|x - o_{V_x}|}{v_s}$, $j = \frac{|y - o_{V_y}|}{v_s}$, and $k = \frac{|z - o_{V_z}|}{v_s}$. This process is illustrated in Figure 19 (right). Here, the voxelized grid represents a binary representation.
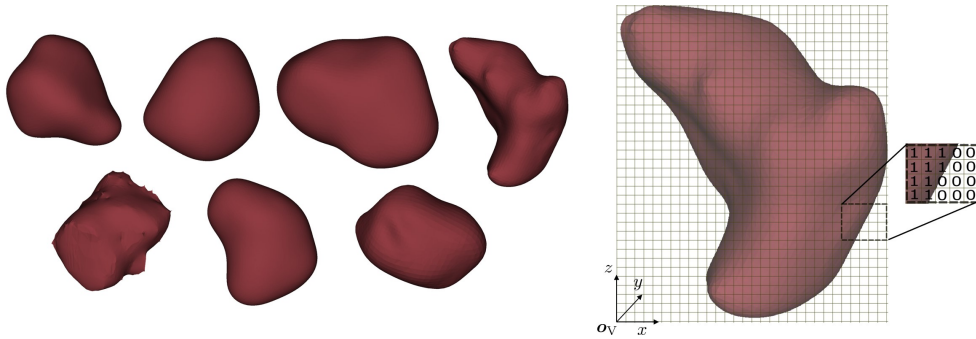

Figure 19: Segmented tumor volumes of different size and shape (left) and volume of interest as a voxelized grid (planar view, right). Voxels inside the volume are set to *one* and outside to *zero*.

5.3.1.2 *Surgical Workspace*

If the application requires the consideration of obstacles, the overall surgical workspace is converted into a voxelized grid. The extent of the voxelized grid is then defined by the extent G_V in x, y, and z-direction considering all volumes or objects (including obstacles). If obstacles are present, they are assigned a different value (> 1) to differentiate them from the target volume. An exemplary voxelized surgical workspace is illustrated in Figure 20, where the target volume is depicted in red and the obstacles in gray.

5.3.2 *Trajectory*

A trajectory defines the path from a start position (on the body surface or within if the CTCR is brought into the body through a different medical device, e.g. a straight endoscope) towards a goal position within the human body. For some medical applications, there might also exist multiple feasible trajectories, as multiple start or goal positions exist. A trajectory can be defined by a straight or nonlinear path - dependent on the application. The insertion point $\mathbf{o}$ can be selected manually by the surgeon or can be optimized from a set of feasible insertion points.
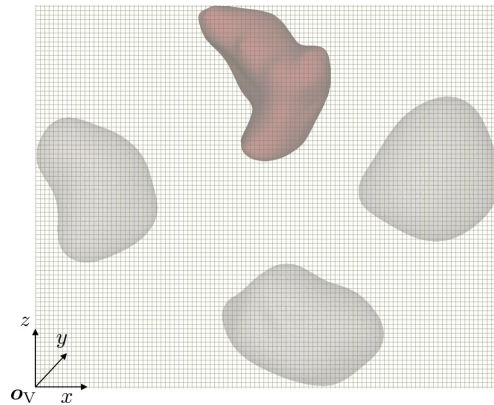
Figure 20: Voxelized grid representation with the target volume in red and obstacles in gray.

5.3.2.1 *Straight Trajectory*

A trajectory towards a target is defined by an insertion point $\mathbf{o}$ and a trajectory vector $\mathbf{h}$ pointing towards the target. The trajectory vector can be computed by considering the insertion point $\mathbf{o}$ and either a surface data point $\mathbf{a}$ of the target volume G_S, or its centroid $\mathbf{c}$. An insertion point on the skull surface and the corresponding trajectory towards a target volume are depicted in Figure 21 (left). Note, that the insertion point $\mathbf{o}$ can be on the surface but also within the body if the CTCR is employed through an insertion tool.
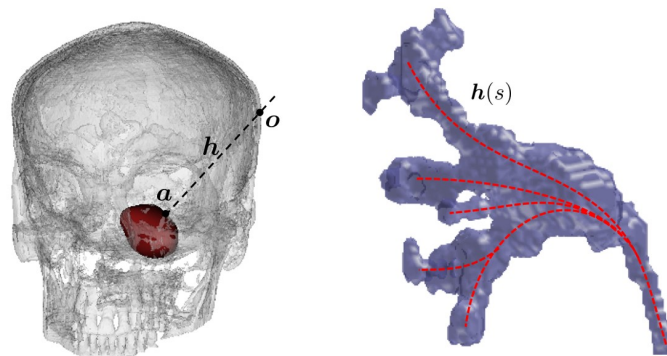
Figure 21: Skull with tumor in red. Insertion point $\mathbf{o}$, trajectory towards the tumor volume $\mathbf{h}$, and tumor surface point $\mathbf{a}$ (left). Multiple nonlinear trajectories $\mathbf{h}(s)$ (in red) from the ureter and renal pelvis into the renal calyces of the kidney (right).

5.3.2.2 *Nonlinear Trajectory*

The trajectory towards a target can also be defined by a nonlinear path $\mathbf{h}(s)$. This is illustrated in Figure 21 (right), where multiple nonlinear trajectories (in red) start at the insertion point $\mathbf{o}$ within the ureter and follow through the renal pelvis into the renal calyces of the kidney. The computation of the nonlinear trajectory can be achieved through thinning of the voxelized representation to determine its skeleton (T.-C. Lee and Kashyap, 1994).

5.3.3 *Coordinate Systems*

The robotic coordinate system B has its zero reference at $s = 0$. The medical coordinate system has its zero reference at the insertion point $\mathbf{o}$. For further computation purposes (i.e. kinematic modeling), medical image data is converted into the robot coordinate system using the transformation matrix $_E\mathbf{T}^B$, such that the position and orientation of E align with B. This transformation and the two coordinate systems are illustrated in Figure 22.
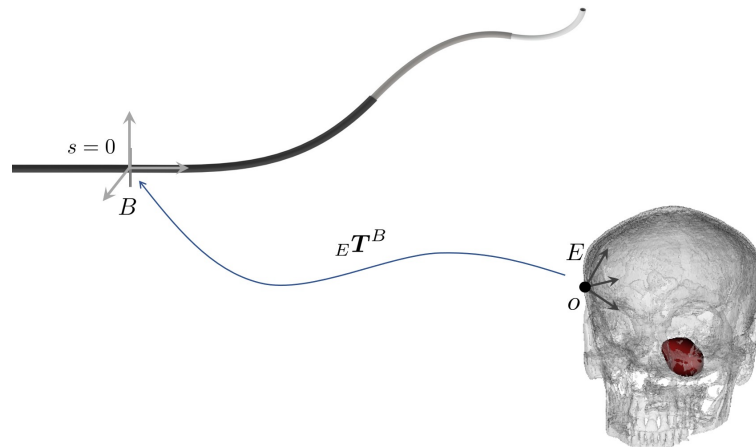
Figure 22: Robot coordinate system B at $s = 0$ and surgical coordinate system E with insertion point o. The transformation between the two coordinate systems is $_E\mathbf{T}^B$.

To generate a voxelized representation G_V of the surgical workspace into the robot coordinate system, the surface data points G_S are transformed through $_E\mathbf{T}^B$ into the robot coordinate system and the transformed point cloud is then converted into a voxelized representation.

5.3.4 *Margins*

A margin is defined as the periphery within or outside a volume. Such margins can be implemented for safety to ensure that the robot avoids the defined periphery (e.g. to keep the CTCR away from critical structures) but also to explicitly reach it by the end-effector (to manipulate within this periphery).

Implementation of such a margin is highly dependent on the geometry of the volume. It can be, for instance, implemented through dilation or reduction of the volume. This is achieved by translation of surface data points towards/from the centroid of a volume. If the object is rather thin and long, then another approach is to scale an object by a defined percentage through a homogeneous transformation of surface normals. If the volume is highly non-convex, then a different approach needs to be considered to preserve topology. The explicit assumption here is that medical image data and corresponding volumes are not highly non-convex, such that a margin can be implemented by dilation or reduction of the volume.

To implement a margin δ utilizing a reduction approach, the surface dataset G_S of a volume is considered. The volume is then shrunken towards its centroid $\mathbf{c}$. The mean of all surface data points accounts for an estimate of the centroid $\mathbf{c}$. To achieve a reduction of the volume, each surface point $\mathbf{a}$ is translated towards the centroid by δ as

$$\mathbf{a}^* = \mathbf{a} + \delta \cdot \frac{\mathbf{c} - \mathbf{a}}{|\mathbf{c} - \mathbf{a}|} . \tag{17}$$

Alternatively, to achieve a dilation of the volume, the direction vector in (17) is pointing into the opposite direction.

5.4   KINEMATIC MEASURES

These following metrics describe the approximation and characterization of the robotic workspace. They are required for the computation of objective functions and are tied to the specific CTCR.

5.4.1   *Approximation of the Configuration Space*

5.4.1.1   *Discretization*

This method approximates the configuration space Q with $\mathbf{q} = [\alpha_1, \ldots, \alpha_n, \beta_1, \ldots, \beta_n]$ by dividing it into m_s translational increments $\triangle\beta$ and m_s rotational increments $\triangle\alpha$ following $\beta_i \in [-\ell_i, 0]$ and $\alpha_i \in [-\pi, \pi)$, and considering the inequalities

$$\beta_1 \leqslant \ldots \leqslant \beta_n \leqslant 0,$$

$$\ell_n + \beta_n \leqslant \ldots \leqslant \ell_1 + \beta_1,$$

with $i \in [1, \ldots, n]$ and n being the overall number of tubes. To save computation time, the translational parameters can also be bounded to an upper or lower boundary.

5.4.1.2   *Sampling of the Configuration Space*

This method applies random sampling of the configuration space Q, where $m_s \times n$ uniformly distributed random samples are generated for $\mathbf{q} = [\alpha_1, \ldots, \alpha_n, \beta_1, \ldots, \beta_n]$. As this method can lead to unique samples q, they are removed for further processing. The following constraints apply

$$\alpha_i \in [-\pi, \pi),$$
$$\beta_n \in [-\ell_{s_n}, 0],$$
$$\beta_i \in [\ell_i - \ell_{i-1} + \beta_{i+1}, \beta_{i+1}] \quad \forall_{i=1,\ldots,n-1}.$$

5.4.2   *Reachable Workspace*

For each configurational parameter set $\mathbf{q}$, the forward kinematic model (see Chapter 2) is utilized to determine the space curve $\mathbf{g}(s)$. The reachable workspace W_R then

defines the set of all end-effector positions. This metric can be used to determine the size and boundaries of the workspace, as the extent in x, y, z-direction can serve as an indicator (Burgner-Kahrs, Gilbert, et al., 2014; Granna and Burgner, 2014).

5.4.3 *Workspace Volume*

The overall CTCR workspace volume W_V can be determined by converting the reachable workspace into a voxelized grid, as in Section 5.3.1. The workspace volume then accounts for all voxels $W_V > 0$ multiplied by v_s^3 (Burgner-Kahrs, Gilbert, et al., 2014; Granna and Burgner, 2014).

5.4.4 *Redundancy*

W_V can also account for a redundancy measure, if one counts all end-effector positions e in each voxel as

$$W_V = W_V + 1 \quad \forall e \in W_R.$$

W_V then accounts for a volume that describes the density of end-effector positions within the workspace volume (Burgner-Kahrs, Gilbert, et al., 2014; Granna and Burgner, 2014).

5.5 PERFORMANCE MEASURES

These metrics describe the performance of the CTCR during utilization. They are required for objective function computation.

5.5.1 *Reachability*

This describes the accessibility of a target volume. The determination of this measure requires the prior computation of the CTCR workspace W_R to determine whether a voxel of the target volume G_V is reachable. A voxel is defined as *reachable* if it is accessible by the robot's tip and the backbone is not colliding with surrounding anatomical structures or obstacles.

This computation makes the implicit assumption that all reachable voxels are reachable from all others. This implies no collisions of the robot with obstacles and no boundary violation.

5.5.2 *Collision Avoidance*

To determine whether the robotic backbone collides with surrounding anatomical structures, the anatomical workspace G_V is converted into the robot coordinate system. For each backbone point of the robotic backbone $g(s)$, it is determined whether it refers to a voxel within G_V that is > 1. If this is the case, then the robotic structure collides with surrounding obstacles.

5.6   CLASSIFICATION

This section aims to classify the optimization problem, where each specific problem can be defined by certain **parameters**, **objectives**, and **constraints**. As the robot is intended to be optimized for medical applications, the parameters and constraints are either robot or application dependent, see Figure 23.
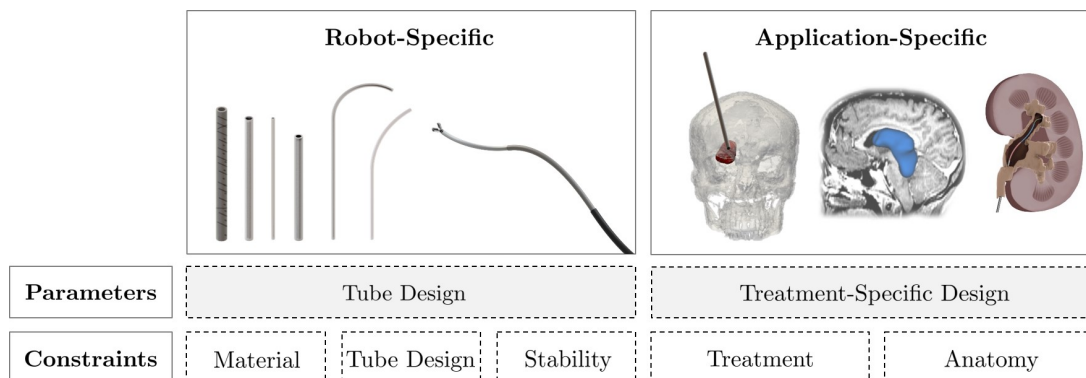

Figure 23: Classification of parameters and constraints into robot- and application-specific.

5.6.1   *Parameters*

The parameter set depends on the employed robot design or medical application. Hence, the parameter space can be divided into robot- and application-specific parameters.

5.6.1.1   *Robot-Specific Parameters*

Robot-specific parameters describe the design parameter space of a single CTCR. The overall number of parameters that could potentially be optimized includes the number of tubes n with $n \in [1, ..., i]$, the tube material properties including the elastic modulus E_i, and the Poisson's ratio ν_i, the curved and straight section length ℓ_{c_i} and ℓ_{s_i}, outer and inner diameter OD_i and ID_i, and curvature κ_i of the curved section.

5.6.1.2   *Application-Specific Parameters*

There exist also those optimization parameters, which are specifically tied to the medical application and are treatment dependent. Some of these parameters can be patient-specific, e.g. the insertion point of the robot, the trajectory towards the goal, or a specific orientation. If parameters are patient-specific, anatomical information can be acquired from medical image data (CT, MRI, ultrasound). Medical treatments could include, for instance, visual inspection with cameras, the suctioning of blood or tissue, the ablation of tissue, the manipulation of tissue using tools, and the collaboration between robotic arms. Optimization parameters for a certain medical application can be camera requirements, motion profiles (for the manipulation of tissue, or the suctioning of blood), ablation dependent characteristics, tool requirements for

manipulation (this could include a required stiffness to exert forces), or the triangulation between robotic arms.

5.6.2 *Objectives*

The optimization problem can be defined by different objectives that represent a quality measure of the optimization. Depending on the formulation of the objective function, the objectives are either minimized or maximized during the optimization procedure. However, as stated in Chapter 3, an optimization function can be formulated as minimization or maximization and transformed into either-or.

Objective functions that require minimization can be for instance the tip or path deviation, the deflection of the shape due to forces, the remaining volume (which must be covered), the number of utilized tubes, the number of unstable configurations for stability, a specific orientation angle, the traveled distance in task space, or certain workspace constraints.

Objective functions, which are formulated for maximization are for example the number of reachable target points, the number of reachable voxels (for volume-based objective), the coverage a volume, the number of stable configurations, a specific orientation angle, the traveled distance in configuration space, the workspace volume, specific workspace constraints, or the camera view.

The following example objectives are inspired by the state of the art and are specifically targeted to the use of CTCR in the previous mentioned applications (neurosurgery, intracerebral hemorrhage evacuation, endonasal surgery, cochlear implant insertion, intracardiac surgery, bronchoscopy, transforaminal hippocampotomy, cooperative task deployment, structural stiffness within the workspace, and laser-induced thermal therapy). Newly presented objectives are the deflection, the orientation, the traveled distance in Cartesian and configuration space, and workspace-specific objectives. Note, that these are objectives specifically targeted towards the structural design of CTCR. Also, simple design objectives can be included (e.g. the number of tubes, number of utilized CTCR, robot length, curvature, number of unstable configurations). Application-specific objectives that target the utilization of specific end-effector tools (e.g. laser, camera) can also be added as objectives into the design optimization procedure as well.

5.6.2.1 *Examples*

The objective functions presented here are evaluated based on one specific parameter set x. Various objective functions require the use of the forward kinematics model (Cosserat rod model presented in Chapter 2) to determine the space curve $g(s)$ and the end-effector position e for the investigated parameter set. In some cases, various calls of the forward kinematics are required to generate the overall CTCR workspace.

End-Effector Deviation This objective function is utilized to describe the deviation of the end-effector from one or multiple goals. The goal here is defined by point h. To determine the objective $f_{\text{deviation}}$, the following steps apply

1. Generate the configuration space Q for the investigated parameter set x.

2. Compute the reachable workspace W_R by determining the space curve $\mathbf{g}(s)$ for each $\mathbf{q}$ and compute the corresponding end-effector position $\mathbf{e}$.

3. Consider only those points from the set of end-effector positions, where the backbone does not collide with surrounding structures.

4. Select the nearest end-effector position (from the remaining set) towards $\mathbf{h}$, by computing the Euclidean distance from each end-effector position $\mathbf{e}$ to the goal $\mathbf{h}$.

5. Compute the Euclidean distance between the end-effector position $\mathbf{e}$ and the goal point $\mathbf{h}$.

$$f_{deviation} = |\mathbf{e} - \mathbf{h}|.$$

Repeat step 1) and 2) for multiple goal points and determine the mean deviation value. The end-effector deviation is measured in mm and illustrated in Figure 24 a).

Trajectory Deviation This objective function intends to optimize the robot towards a trajectory, i.e. minimizes the divergence of the three-dimensional backbone. The trajectory $\mathbf{h}_i$ is defined by N equidistant points $i \in [1, \ldots, N]$. The following steps apply

1. Generate the configuration space Q for the investigated parameter set $\mathbf{x}$.

2. Compute the reachable workspace W_R by determining the space curve $\mathbf{g}(s)$ for each $\mathbf{q}$.

3. Consider only those curves $\mathbf{g}(s)$, where the backbone does not collide with surrounding structures.

4. Divide the space curves $\mathbf{g}(s)$ into N equidistant points $\mathbf{p}_i$.

5. Compute the Euclidean distances between each backbone point $\mathbf{p}_i$ to the corresponding point $\mathbf{h}_i$ for all curves.

6. The objective f_{dev} is then determined by selecting the curve $\mathbf{g}(s)$ with the minimum deviation from $\mathbf{h}(s)$

$$f_{deviation} = \frac{1}{N} \sum_{i=1}^{N} |\mathbf{p}_i - \mathbf{h}_i|.$$

The deviation of the robotic backbone $\mathbf{g}(s)$ from trajectory $\mathbf{h}(s)$ is depicted in Figure 24 b). The trajectory deviation is measured in mm.

Deflection The deflection of the robot as a result of external forces $\mathbf{F}$ can be described by a change from an undeformed shape $\mathbf{g}(s)^*$ to a deformed shape $\mathbf{g}(s)$.

1. Determine the unloaded space curve $\mathbf{g}(s)^*$ for configuration $\mathbf{q}$ utilizing the forward kinematic model for the investigated parameter set $\mathbf{x}$.

2. Determine the loaded space curve $\mathbf{g}(s)$ for configuration $\mathbf{q}$ utilizing the forward kinematic model for the investigated parameter set.

3. Divide both curves $\mathbf{g}(s)^*$ and $\mathbf{g}(s)$ into N equidistant points $\mathbf{p}_i^*$ and $\mathbf{p}_i$.

4. The objective $f_{\text{deflection}}$ can be quantified by computing the Euclidean distances between corresponding points along the unloaded and loaded robot as

$$f_{\text{deflection}} = \frac{1}{N} \sum_{i=1}^{N} |\mathbf{p}_i^* - \mathbf{p}_i|,$$

where $\mathbf{p}_i^*$ are the unloaded robot backbone points and $\mathbf{p}_i$ are the loaded backbone points. Minimization of this objective results in a robotic design, which is more likely to withstand external forces or loads in certain configurations or areas of the workspace. An illustration of this objective is depicted in Figure 24 c). The deflection is measured in mm. Note, that the maximum deviation or deflection can also be considered as an objective.

Remaining Volume and Coverage These describe objectives to execute a surgical plan. This implies to maximize the coverage, or on the contrary to minimize the remaining volume of a target volume. The basis of the computation of these objectives is the voxelized representation of the target volume. The computation of this objective requires the following steps

1. Convert the surgical workspace and target volume into a voxelized grid G_V.

2. Transform the surgical workspace G_V into the robot coordinate system.

3. Determine the CTCR reachable workspace W_R.

4. Determine which voxels of the target volume are *reachable* and *unreachable*.

5. The coverage of the volume f_{coverage} is defined by the ratio of the number of unreachable voxels $\nu_{\text{unreachable}}$ to the number of total voxels ν_{total} within the volume as

$$f_{\text{remaining}} = \frac{\nu_{\text{unreachable}}}{\nu_{\text{total}}}.$$

The remaining volume (coverage) is a ratio between 0 and 1.

Orientation The orientation of the robotic end-effector describes an objective that is important for manipulation tasks. The orientation of the end-effector can be described by the tangent curvature vector $\mathbf{r}_{z_e}$, which is defined as the vector between the last two backbone points.

1. Determine the space curve $\mathbf{g}(s)$ utilizing the forward kinematic model for the investigated parameter set $\mathbf{x}$.

2. Determine the tangent curvature vector $\mathbf{r}_{z_e}$ between the last two backbone points.
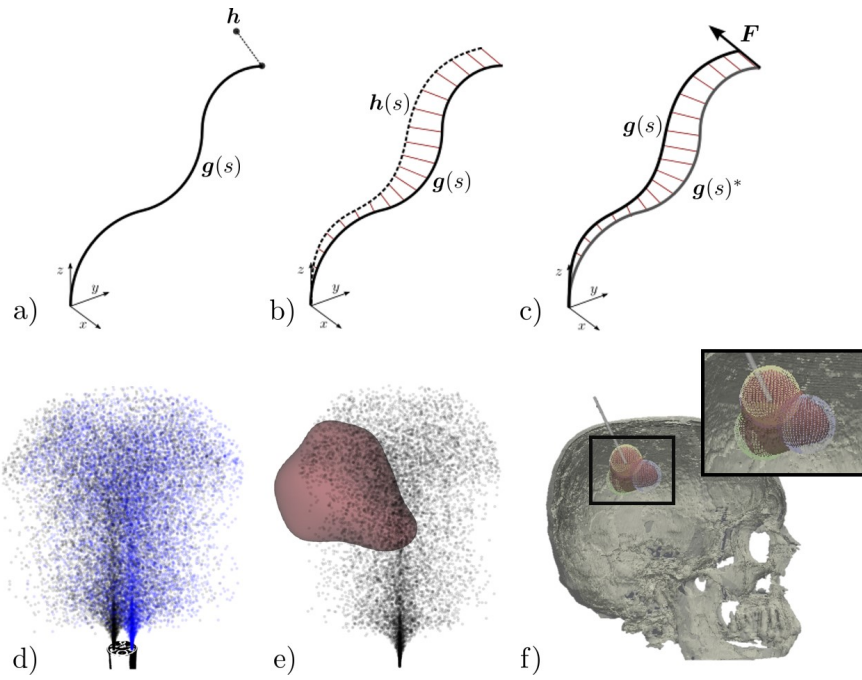
Figure 24: a) Tip deviation, b) path deviation, c) deflection due to forces, d) overlapping workspace, e) CTCR workspace and coverage of a tumor volume, and f) coverage with spherical laser ablations.

3. Compute the angle φ between the required orientation vector $\mathbf{r}_z$ and the tangent vector $\mathbf{r}_{z_e}$. It is determined with

$$\varphi = \text{atan2}\left(\|\mathbf{r}_z \times \mathbf{r}_{z_e}\|, \mathbf{r}_z \cdot \mathbf{r}_{z_e}\right).$$

4. The ideal angle between $\mathbf{r}_z$ and $\mathbf{r}_{z_e}$ is φ_{ideal}. The objective function is thus described by

$$f_\varphi = \varphi_{\text{ideal}} - \varphi.$$

Minimization of f_φ results in an optimal alignment between the two vectors. The orientation is measured in radians.

Traveled Distance This objective function describes either a distance in Cartesian or configuration space. The traveled distance in Cartesian space is the traveled distance by the end-effector of the CTCR. Note, that this could also be the tool center position. One might aim to minimize this distance to operate in a small volume. This objective $f_{\mathbb{R}^3}$ is determined by

1. Determine the motion planning sequence between subsequent target points. This might require solving the inverse kinematics numerically.

2. Determine the sum of Cartesian distances between subsequent end-effector positions as

$$f_{\mathbb{R}^3} = \sum_{i=1}^{N-1} |\mathbf{e}_{i+1} - \mathbf{e}_i|,$$

where e_i is the current end-effector position and e_{i+1} is the subsequent end-effector position, both in Cartesian space. N is the overall number of subsequent configurations. The Cartesian traveled distance is measured in mm.

The traveled distance in configuration space is the traveled distance by the actuators that translate and rotate the tubes. Minimization of this parameter could potentially result in less operation time. The objective $f_{q_{rot}}$ that describes the rotational difference is determined by

1. Determine the motion planning sequence between subsequent target points. This might require solving the inverse kinematics numerically.

2. Determine the sum of distances between subsequent configurations. The objective $f_{q_{rot}}$ that describes the rotational difference is determined by

$$f_{q_{rot}} = \sum_{i=1}^{N-1} |q_{rot_{i+1}} - q_{rot_i}|,$$

and the objective $f_{q_{trans}}$ that describes the translational difference is determined with

$$f_{q_{trans}} = \sum_{i=1}^{N-1} |q_{trans_{i+1}} - q_{trans_i}|,$$

where q_i is the current configuration and q_{i+1} is the subsequent configuration. N is the overall number of subsequent configurations. The traveled distance in configuration space is measured in mm and radians.

Workspace Volume These objectives specifically target the workspace of the CTCR. The aim might be to maximize the reachable workspace or to increase the redundancy within a specified area of the workspace.

1. Determine the workspace volume W_V.

2. The number of voxels > 0 within W_V then accounts for the objective $f_{workspace}$.

The size of the workspace volume ins measured in mm^3.

Workspace Size As the workspace exhibits a rotational symmetry, it can also be approximated trough the generation of samples in a single plane, e.g. x/z-plane. The size of the polygon that spans the extreme end-effector points e can be an indicator for the planar workspace size.

1. Generate the configuration space Q for the investigated parameter set x.

2. Determine all corresponding end-effector points utilizing the forward kinematic model and rotate them into the x/z-plane.

3. Determine the area of the polygon W_P that connects all boundary end-effector points e within the x/z-plane.

The size of the polygon ins measured in mm².

Redundancy To maximize the redundancy in a specified area of the workspace, the following steps apply

1. Determine the workspace volume W_V by counting the number of end-effector positions within each voxel.

2. The objective $f_{redundancy}$ then accounts for the number of redundant end-effector positions within the specified volume.

This objective function is dimensionless.

5.6.2.2 *Combination of Objectives*

The combination of different objectives can be challenging, as they can be classified into homogeneous and heterogeneous objectives, as well as into non-conflicting and conflicting.

If objectives are **non-conflicting**, then all objectives could potentially be combined into a single objective using scalar error metrics. However, this can only be applied if there exists any x or x^*, where $(f_i(x) \prec f_i(x^*))$ or $(f_i(x^*) \prec f_i(x))$ for all objective functions o. Often, they are **partially** or **totally conflicting** in medical applications, such that Pareto dominance methods represent a better concept to cope with the problem. A compromise between weighting and Pareto dominance approaches can also be achieved if some objectives of the problem are conflicting and some are not. Then, non-conflicting objectives are combined into a scalar and used within Pareto optimization.

If objectives are represented by the same units they are by definition **homogeneous**, if not they are **heterogeneous**. If objective functions are heterogeneous, the objectives must be normalized when combined with a weighting approach. Normalization is not always possible, as the maximum or minimum value of an objective function is not always known a priori. The selection of weights is not trivial and influences the outcome of the optimization. Thus, the application of Pareto dominance concepts is preferable for conflicting objectives.

Regarding the example objectives presented in this thesis, the following objectives can be classified as homogeneous: 1) deviation, deflection, traveled distance in Cartesian space, translational distance in configuration space, 2) orientation, rotational traveled distance in configuration space, 3) the remaining volume, and redundancy are dimensionless. However, even though these groups of objectives can be represented by the same units, their range can differ significantly, such that normalization or the selection of weights is necessary for combination

$$y = \sum_{i=1}^{o} \lambda_i f_i(x) \text{ for } \lambda_o > 0 \text{ and } \sum_{i=1}^{o} \lambda_i = 1,$$

where λ_i define the weights for each objective o.

5.6.3 *Constraints*

During the execution of the optimization algorithm, constraints must be applied, such that parameters remain within the search space. As the CTCR tube parameters have many dependencies and the kinematic structure of the robot is not trivial, there exist numerous robot design constraints. Further, the specific medical application can impose constraints on the optimization procedure.

The number of constraints depends on the number of optimization parameters, as the parameter space of these is usually bounded. The design optimization parameters of CTCR can consider the number of tubes n, the tube's material (with the elastic modulus E, the recoverable strain rate ϵ, the Poisson's ratio ν, and the shear modulus G), and the geometric parameters of the robot (the tube's curvature κ, the straight and curved section length ℓ_{s_i} and ℓ_{c_i}, and the outer OD_i and inner diameter ID_i). All aforementioned parameters can thus apply constraints, as they have to remain in predefined parameter space. The constraints are formulated as equality or inequality conditions within the optimization procedure and they are divided into robot- and application-specific constraints in the following.

5.6.3.1 *Robot-Specific Constraints*

These constraints arise from the design nature of CTCR. As the actuation parameters α_i and β_i are constrained as

$$\beta_1 \leqslant ... \leqslant \beta_n \leqslant 0,$$

$$\ell_n + \beta_n \leqslant ... \leqslant \ell_1 + \beta_1,$$

they need to be ensured during the optimization procedure (e.g. when sampling the actuation space, workspace computation). Other dependencies between robot design parameters include the relationship of tube diameters as

$$ID_1 < OD_1 < ID_2 < OD_2 < \cdots < ID_n < OD_n,$$

where also a certain tube clearance needs to be taken into consideration. Further, the material properties (including the elastic modulus E_i and strain limit ν_i) impose constraints on the maximum curvature $\kappa_{i_{max}}$ or minimum diameter OD_i of a tube. The maximum curvature of a tube $\kappa_{i_{max}}$ (or minimum diameter OD_i) depends either on the *a priori* selected tube material, or changes during optimization, if material parameters E_i and ν_i are optimization dependent. The dependency between curvature and diameter is formulated as

$$\kappa_{i_{max}} = \frac{2\epsilon_i}{OD_i(1 + \epsilon_i)},$$
$$OD_{i_{min}} = \frac{2\epsilon_i}{\kappa_i(1 + \epsilon_i)}.$$

The stability of the robot might account for constraints, as certain tube design combinations lead to unstable configurations. The same is true for some designs that require a certain stiffness (Gilbert, Rucker, and Webster III, 2016; Ha, Park, and Dupont, 2016; Hendrick, Gilbert, and Webster III, 2015b; Webster III, Okamura, and Cowan, 2006; R. Xu, Atashzar, and Patel, 2014).

5.6.3.2 *Application-Specific Constraints*

Application-specific constraints cluster into two groups, which are treatment- and anatomy-specific constraints. **Treatment-specific** constraints can impose constraints on the inner diameter ID_i of the tubes. This is depended on the medical tool (e.g. gripper, laser, or camera) deployed through the inner lumen of the robot. Other treatment-specific constraints are defined by the medical task. This can be for instance inspection, manipulation, laser activation, the suctioning of tissue or blood, a specific planning procedure, and the application of external forces and loads.

Considering a specific patient case, the anatomy imposes constraints during the optimization. This can be, for instance, a specific required outer diameter OD_i to deploy the robot within a tight lumen, a curvature κ_i to maneuver along tortuous paths, or the overall length ℓ of the robot to reach the desired goal. Other application-specific constraints include obstacle avoidance and motion planning that could be incorporated into the algorithm to determine feasible configurations of the robot. The **anatomy constraints** can be embedded into the optimization by considering patient image data as inputs to the algorithm.

Both treatment and anatomy dependent constraints limit the minimum or maximum value for the design parameters of the CTCR and are formulated as

- number of tubes $n_{min} \leqslant n \leqslant n_{min}$

- curvature $\kappa_{min} \leqslant \kappa_i \leqslant \kappa_{max}$

- curved length $\ell_{c_{min}} \leqslant \ell_{c_i} \leqslant \ell_{c_{max}}$

- straight length $\ell_{s_{min}} \leqslant \ell_{s_i} \leqslant \ell_{s_{max}}$

- outer diameter $OD_{min} \leqslant OD_i \leqslant OD_{max}$

- inner diameter $ID_{min} \leqslant ID_i \leqslant ID_{max}$

- elastic modulus $E_{min} \leqslant E_i \leqslant E_{max}$.

All optimization parameters have to remain within a predefined parameter space.

5.7   ALGORITHMIC IMPLEMENTATION

The selection of a suitable algorithm requires to consider the overall optimization problem. Linear optimization is not suitable for parameter optimization of CTCR, as highly nonlinear differential equations must be solved. The deployment of nonlinear algorithms is thus a necessity. These are subdivided into local and global methods. As the parameter space is multidimensional and multimodal, a global method is proposed here. These methods are more likely to cover the whole search space of CTCR without remaining stuck in local minima. However, this does not necessarily imply that they find the best or optimal solution.

The assumption here is that evolutionary algorithms, particularly particle swarm optimization, have the potential to be applied to parameter optimization of CTCR. Their application is currently unexploited by the state of the art. However, they have

been successfully employed for other robotic systems (Simon, 2013). Thus, this thesis investigates the applicability of particle swarm optimization to the structural design optimization problem of CTCR.

CTCR are defined by many parameters, which all impose constraints on the parameter space. Further, constraints arise from the dependencies between actuator values and the composition of tubes. Additional constraints are dependent on the medical application or task. The parameter space is thus multimodal, and the decision vector might have to jump from one feasible space to the other. Here, evolutionary algorithms can be efficient.

The combination of objectives is not straight forward for the application in a medical scenario, as they can be heterogeneous. Particle swarm optimization can apply Pareto dominance methods and handle heterogeneous multi-objective functions.

The kinematic model is highly complex compared to other robotic systems, as well as their kinematic structure. The material and stiffness properties influence the interaction of the tubes and the morphology of the robot in contrary to robots that are composed of rigid links, joints or non-deformable materials.

One advantage of particle swarm optimization is their extension to variable dimension. This makes the algorithm applicable to a larger domain of problems, where decision vectors can be either of fixed or variable size. Further, they are not sensitive to population size (Shi and Eberhart, 1999). Thus, smaller population sizes can be selected to find a suitable solution. This can be especially advantageous, as the computation of objective functions requires usually many calls of the kinematic function, such that the computational effort increases with population size dramatically. Further research findings demonstrate that particle swarm optimization outperforms genetic algorithms with respect to computational effort to find high-quality solutions (Hassan et al., 2005). It shows better convergence for complex objective functions dependent on multiple variables (Ramezan Shirazi, Seyyed Fakhrabadi, and Ghanbari, 2014).

This section presents the implementation of the particle swarm optimization algorithm proposed in this thesis, which is extensible to single, multiple, non-conflicting, and conflicting objectives, as well as fixed and variable dimension of decision vectors.

The overall swarm is defined to consist of P particles with position $x_{k_m}^t$ and velocity $v_{k_m}^t$ at time t, where m is the dimension of each particle k. Each particle's velocity and position change from generation t to $t + 1$ (until the maximum number of generations T is reached), as the swarm explores the search space. The implementation of the overall algorithm can be depicted in Algorithm 1. The steps of the algorithm are explained in the following to account for single, non-conflicting, or conflicting objectives. Further, the implementation of the algorithm is explained for fixed and variable dimension.

5.7.1 *Input*

Input to the algorithm is patient-specific image data. This can be a voxelized grid of the target volume or obstacles, the trajectory h, the robot and medical coordi-

nate systems, and margins. Further, the preallocation of parameters, objectives, and constraints are input to the particle swarm optimization algorithm.

5.7.2 *Initialization*

The selection of the number of generations T depends highly on the application and the convergence rate or the spread of the Pareto front. It is adjusted application dependent, however, the authors in (Coello Coello and Lechuga Salazar, 2002) advise to select at least 80 function evaluations. The number of particles P should be at least 20 as the authors in (Shi and Eberhart, 1999) demonstrate good performance for population sizes of 20, 40, 80, and 160 particles. They conclude that the performance does not improve with larger population size. The author of (Trelea, 2003) evaluate particle swarm optimization for 15, 30, and 60 particles. 15 particles lead to fast convergence and 60 particles result in more function evaluations. The best results are obtained for 30 particles. The authors in (Coello Coello and Lechuga Salazar, 2002) advise to select 20 to 80 particles for multi-objective particle swarm optimization.

The inertia weight η ranges between 0.4 and 1.4. The higher the inertia weight, the larger the exploration of the search space and the lower the convergence rate to a single value or the Pareto front. c_1 and c_2 control the influence of the self-confidence of a parameter set and the confidence of the swarm. If $c_1 = c_2$ there exists a compromise and an even influence between exploration of the search space and exploitation. Generally, c_1 varies between 1.5 and 2 and c_2 between 2 and 2.5. These parameters can be easily adapted to change the relationship between exploration and exploitation but must be selected depending on the application.

The second initialization is concerned with the initial population of the swarm, i.e. the initial set of decision vectors. The dimension of the decision vector $\mathbf{x}$ is generally not constrained but the higher the dimension, the higher the computational complexity. Generally, the dimension of the decision vector should be kept as small as possible, as the convergence of the algorithm is affected negatively otherwise. This might not result in a sufficient set of solutions.

To generate the initial population, each dimension m of particle $\mathbf{x}_{k_m}$ with variable dimension has to be initialized based on a uniform random distribution within the parameter space. If each particle has the same dimension within the swarm, then m is equal for all particles.

Considering the structural design optimization of CTCR, a particle (decision vector) represents the optimization parameters of the problem (considering the design and application-specific parameters). The parameter space is thus defined by the application- and robot-specific constraints that describe the underlying problem, see Section 5.6.3.

5.7.3 *Function Evaluation*

The determination of a particle's cost $\mathbf{y}$ depends on the number of objectives, and whether objectives are conflicting or not. The number of objective functions in multi-objective particle swarm optimization can be up to three. Additional objective func-

tions would classify the problem as many-objective. Many-objectives require specific algorithmic implementations (Fleming, Purshouse, and Lygoe, 2005) and are not regarded in the scope of this work. The cost of a particle can represent the objectives mentioned in Section 5.6.3. There exist different methods to represent the cost of a particle depending on the number of objectives and whether they are non-conflicting or conflicting, as explained in the following.

5.7.3.1 *Single-Objective or Non-Conflicting Objectives*

If the optimization problem is defined by a single objective, then the particle's cost $y = f(x)$. This is also the case if objectives are non-conflicting and a weighted sum approach is selected to compute one single objective function out of multiple. The cost of a particle is then defined by $y = \lambda_1 f_1(x) + \ldots + \lambda_o f_o(x)$, where λ are the weights and o are the overall number of objectives.

5.7.3.2 *Conflicting Objectives*

If objectives are conflicting, then the concept of Pareto optimality is applied. This implies that some particles dominate others. A particle (decision vector) x_k **strictly dominates** another particle (decision vector) x_k^* ($x_k \prec x_k^*$), if $f_i(x_k) \leqslant f_i(x_k^*)$ $\forall i = 1\ldots o$ and $f_i(x_k) < f_i(x_k^*)$ for some i. A particle x_k **weakly dominates** another particle x_k^* ($x_k \preccurlyeq x_k^*$), if $f_i(x_k) \leqslant f_i(x_k^*)$ for all i. A **non-dominated** particle x_k thus means, that there exist no $f_i(x_k^*) \leqslant f_i(x_k)$ for all i.

Thus, a particle is represented by multiple costs f_i, where $i \in [1, \ldots, o]$ with o being the number of objectives. Applying the concept of Pareto optimality results in a Pareto optimal set of solutions $\mathcal{P}_s$ that span the Pareto front $\mathcal{P}_s$.

5.7.4 *Leader Selection*

To ensure a good convergence rate, the selection of leaders is based on the idea of the global topology approach, as this is the most prominent approach in multi-objective particle swarm optimization (Reyes-Sierra and Coello Coello, 2006). This implies that each particle is connected with all members of the swarm and information exchange happens between all of them.

5.7.4.1 *Single-Objective or Non-Conflicting Objectives*

Here, the leader of the swarm is the global best position g_b^t considering all particles. Each particle's personal best solution $p_{b_k}^t$ found so far and the global best solution g_b^t within the overall swarm can then be determined to function as leaders.

5.7.4.2 *Conflicting Objectives*

The *non-dominated* solutions across all generations are stored within an archive A_t. Each *non-dominated* particle from the current population is added to A_t. A particle is deleted from A_t, if it is dominated by another particle within A_t. To select a leader g_b^t, a decision vector is then randomly drawn from A_t.

Algorithm 1 PSO and MOPSO

INPUT: patient dataset, robot- and application-specific parameters
DEFINE T, P, η, c_1, c_2
INITIALIZE x_{k_m}, v_{k_m}
for $t = 1 : T$ **do**
    $\{y_i\} :=$ FUNCTION EVALUATION(x_k^t)
    $\{p_{b_k}^t, g_b^t\} :=$ LEADER SELECTION$(x_k^t, p_{b_k}^{t-1}, g_b^{t-1}$ or $A_t, y_i)$
    for $k = 1 : P$ **do**
        $\{x_{k_m}^{t+1}, v_{k_m}^{t+1}\} :=$ UPDATE$(x_{k_m}^t, v_{k_m}^t, p_{b_k}^t, g_b^t, \eta, c_1, c_2)$
        $x_{k_m}^{t+1} :=$ ENFORCE CONSTRAINTS$(x_{k_m}^t)$
    end
end
RETURN g_b^t or A_t

5.7.5 *Position and Velocity Update*

The influence of c_1 and c_2 is exploited to control exploration and convergence. Independent from whether each particle is of equal dimension or not, the position of each particle's component $x_{k_m}^{t+1}$ is determined with

$$x_{k_m}^{t+1} = x_{k_m}^t + v_{k_m}^{t+1}.$$

The update of the velocity $v_{k_m}^{t+1}$ depends on equal or variable dimension within the swarm, as follows.

5.7.5.1 *Equal Dimension*

If the dimension within the swarm is equal for all members, then the velocity is updated according to

$$v_{k_m}^{t+1} = \eta \cdot v_{k_m}^t + c_1 \cdot r_1 \cdot (p_{b_{k_m}}^t - x_{k_m}^t) + c_2 \cdot r_2 \cdot (g_{b_m}^t - x_{k_m}^t),$$

with η being the inertia weight, c_1 and c_2 are constants controlling the influence of personal versus global best and r_1 and r_2 are randomly chosen in the range of $[0, 1]$.

5.7.5.2 *Variable Dimension*

A variable dimension enables optimization for a prior undefined number of optimization parameters. This is especially advantageous for the parameter optimization of CTCR, as the dimension of some parameters is not known a priori, e.g. the number of tubes can be variable.

The velocity and position are updated according to the dimensions of each particle and the global best solution found so far, where the overall number of components of a particle is defined as N_m and the overall number of components within the global best solution g_b is N_{m_g}. There exist three scenarios to determine the velocity $v_{k_m}^t$ for each component, considering N_m and N_{m_g}

1) $N_m = N_{m_g}$

$$v_{k_m}^{t+1} = \eta \cdot v_{k_m}^t + c_1 \cdot r_1 \cdot (p_{b_{k_m}}^t - x_{k_m}^t) + c_2 \cdot r_2 \cdot (g_{b_m}^t - x_{k_m}^t),$$

2) $N_m > N_{m_g}$

The number of N_{m_g} components are selected randomly from x_k. The velocity for these components is determined according to (16). The velocity of the remaining $N_m - N_{m_g}$ components m is determined with

$$v_{k_m}^{t+1} = \eta \cdot v_{k_m}^t + c_1 \cdot r_1 \cdot (p_{b_{k_m}}^t - x_{k_m}^t).$$

3) $N_m < N_{m_g}$
N_m components are randomly drawn from g_b and the velocity is determined with equation (16) using the selected components.

5.7.6 *Constraints*

This algorithm employs the truncation method as this results in high performance independent of the application (Alvarez-Benitez, Everson, and Fieldsend, 2005). To enforce the parameters to remain within the parameter space as

$$x_{k_m}^t = \begin{cases} u_{b_m} & , \text{if } x_{k_m}^t > u_{b_m} \\ l_{b_m} & , \text{if } x_{k_m}^t < l_{b_m}, \end{cases}$$

where l_{b_m} are the lower boundary and u_{b_m} are the upper boundary components.

5.7.7 *Output*

5.7.7.1 *Single-Objective or Non-Conflicting Objectives*

The output of the algorithm here is the global best solution g_b^t. This output is achieved when the maximum number of generations T is reached, or the algorithm converges.

5.7.7.2 *Multi-Objectives*

Once the maximum number of generations T is reached, the optimization ends, and the Pareto optimal solutions are stored within A_t. A solution from the Pareto front can be selected manually (e.g. by the surgeon) or automatically based on performance criteria, which can be determined based on preferences by a surgeon or other constraints.

5.8 SUMMARY

This section discusses the applicability of the proposed optimization algorithm and summarizes the contribution of this chapter.

5.8.1 *Applicability of the Methodology*

The hypothesis of this thesis is the potential of the proposed framework to solve the structural design problem of CTCR. The following paragraphs provide instructions

on how state of the art problems could be reformulated as multi-objective and solved with particle swarm optimization.

Optimization for Endonasal Pituitary Surgery The authors in (Burgner, Gilbert, and Webster III, 2013) optimize a three-tube CTCR to be utilized in endonasal pituitary surgery, where the outer tube is straight and the two innermost are curved. The optimization parameters are the straight and curved section lengths and curvature of the two inner tubes, which results in six parameters total. The objective is the percentage of coverage of the tumor volume by the CTCR. Here, the authors successfully apply a Nelder-Mead algorithm for design optimization. Further, they conclude that the deployment of multiple concentric tube robots simultaneously or subsequentially could improve their results and increase tumor coverage.

Here, the application of multiple objectives and a multi-objective optimization algorithm could have potential. An additional objective could be the number of sequentially employed robots. These objectives are conflicting: the employment of subsequent robots requires time for tube exchange, such that the number of utilized CTCR should be at a minimum. However, the utilization of differently designed CTCR increases coverage.

Thus, the multi-objective particle swarm algorithm could optimize for a Pareto optimal set regarding coverage and number of robots (tube combinations). The surgeon could then select the preferred solution with a minimized number of employed robots but sufficient coverage (remaining coverage could be treated by chemotherapy) from the Pareto front.

Another option would be to apply the CTCR as single-objective but to utilize the variable dimension of decision vectors of the algorithm. Additional optimization parameters could then be the number of utilized tubes or CTCR.

Parameter Optimization for Sets of Concentric Tubes The authors in (Baykal, Torres, and Alterovitz, 2015) present a similar approach and optimize the design of sequentially employed CTCR to maximize the coverage of a goal region. Here, tubes are envisioned to be exchanged during deployment. While the utilization of sequential sets of tubes results in improved coverage of the goal region, the authors aim to minimize the number of utilized CTCR during surgery to reduce time effort.

The authors optimize the design parameters of a CTCR (including the straight and curved section length, and curvature of tube i) utilizing a global optimization algorithm (adaptive simulated annealing). The contribution of this work is the inclusion of a motion planning algorithm for obstacle avoidance (using rapidly exploring random trees), which considers the deployment of the robot.

To solve the design optimization problem, the authors utilized two sequentially employed algorithms. The first algorithm maximizes the coverage of a goal region for a fixed set of sequentially employed CTCR. This algorithm is executed multiple times to determine the coverage for different sets. The second algorithm then minimizes the number of sets that allow for a required percentage of coverage.

Here, the objectives are conflicting as a decrease in the number of utilized CTCR does not decrease the uncovered volume of the reachable space. Thus, the multi-objective particle swarm optimization algorithm could have potential, as it would

not require the execution of two sequential algorithms. The proposed approach could optimize for coverage and the number of utilized CTCR simultaneously. As the proposed framework can incorporate decision vectors with variable length, each sequentially utilized CTCR could have a variable number of tubes. The algorithm could optimize for an optimal combination of tubes and sequentially employed CTCR. A solution from the front of Pareto optimal solutions can then be selected either automatically (based on a threshold) or by the surgeon.

Optimization based on Task and Anatomical Constraints The authors in (Bergeles, Gosline, et al., 2015) take a different approach. They aim to minimize the robot's extension length and curvature while ensuring the reachability of target points. Minimization of the extension length should lead to an overall better stiffness of the CTCR and a minimized curvature can prevent tubes from plastic deformation. Here, the optimization problem is divided into 1) reachability of the target (includes the end-effector position error, the orientation error, and violation of anatomical constraints), and 2) optimal robot design (includes the extension length and curvature). Aim of the optimization algorithm is to minimize the end-effector error, orientation error, violation of constraints, extension length, and curvature. All aforementioned objectives are combined in a scalar error metric utilizing different weights. Here, the employed Nelder-Mead algorithm does not consider constraints as separate equality or inequality functions, such that they are combined into the objectives as penalties.

The authors apply their algorithm to neurosurgery and a beating-heart procedure. Both applications require the selection of different weights, as objectives are heterogeneous. The minimization of curvature and extension length does not necessarily result in the reachability of the target such that objectives are conflicting. The relationship between these objectives is complicated but could be analyzed through the multi-objective approach presented in this work.

The problem could be formulated using three objective functions which describe the reachability (tip and orientation error), the curvature, and extension length of the tubes. The tip and orientation error can be included in a scalar metric by converting the orientation error into a radian measure in mm. The curvature of the tubes and extension length are then independent objectives, as they conflict with the reachability of the target. Another option would be to utilize two objective functions that describe the reachability and the length of the tubes. The maximum curvature of the tubes can be incorporated as a constraint into the multi-objective particle swarm optimization, as well as anatomical constraints.

5.8.2 *Conclusion*

This chapter presents the basis of this thesis and describes the general optimization problem for CTCR in minimally invasive surgery. This is the first work to give an overview of the general problem. Further, the workflow of the proposed optimization methodology is described with respective in- and outputs.

Medical images are input to the design optimization methodology and data representation methods are proposed to handle different patients and medical scenarios.

This includes the representation of target volumes and obstacles, trajectory computation, and kinematic performance measures.

The contribution of this chapter is the presentation of parameters, objectives, and constraints for minimally invasive procedures that are predestined for CTCR. The parameters include the overall parameter space, as well as geometric and material parameters. This chapter specifically describes the computation of objective functions that are different from other robotic applications and thus specifically tied to minimally invasive procedures.

The general assumption of this thesis is that evolutionary optimization algorithms, particularly particle swarm optimization, can cope with the parameter optimization problem of CTCR. The presented particle swarm optimization algorithm employed in this thesis is formulated, such that it can handle single, multiple, non-conflicting and conflicting objectives. Here, the use of particle swarm optimization with variable dimension is proposed - which is new in the area of robotics. The variable dimension of decision vectors is especially advantageous for the structural design optimization of CTCR, as the number of parameters (i.e. the number of tubes, or curved sections) is not known a priori.

Further, the concept of Pareto optimality, which is new to the parameter optimization of CTCR for conflicting objective functions, is explained. This enables the optimization of heterogeneous objectives.

The following chapters represent three example medical scenarios to show the applicability of the proposed algorithm and prove that particle swarm optimization can cope with the structural parameter optimization problem of CTCR, as well as handle other application-specific parameters.

The first application deals with the simultaneous deployment of two CTCR robotic arms to execute a medical task. The proposed design optimization methodology is applied. Additionally, the performance of particle swarm optimization is compared to Nelder-Mead optimization (following the state of the art). Here, the algorithm is utilized as single-objective, as multiple conflicting objectives are not exploited by the state of the art thus far.

The second example considers the overall design parameter space of CTCR, multiple objectives and incorporates external forces for the first time. The aim here is the structural stiffness for force absorption and an increased workspace of the CTCR.

The last application envisions the CTCR in laser-induced thermal therapy. The problem is formulated as multi-objective and accounts for design-, as well as application-specific parameters to demonstrate the extensibility of the proposed algorithm.

Part III

APPLICATIONS

OPTIMIZATION FOR COOPERATIVE TASK DEPLOYMENT

This chapter presents the design optimization problem for two CTCR to work collaboratively, which allows for the simultaneous deployment of multiple tasks. The robotic arms are intended to be employed in a dual channel endoscope. Generally, endoscopes can be utilized in minimally invasive surgery and the incorporation of additional robots into the endoscope could advance single port access surgery that is still restricted until today.

Optimization parameters are the curvature and curved length of each robot. This presents the first approach to optimize two collaborative CTCR arms and the definition of a novel objective, which allows for advanced triangulation of the two end-effectors to improve and enable medical task performance. The presented optimization methodology allows to formulate and identify parameters, the objective, and constraints of this specific problem. Additionally, this chapter compares the performance of the single-objective particle swarm algorithm to the Nelder-Mead algorithm applied by the state of the art.

6.1 MOTIVATION

The employment of multiple CTCR arms allows for robotic cooperation and simultaneous execution of a medical task. This includes manipulation tasks and the employment of different medical tools, such that redeployment and tool exchange of one robot is not necessary. Dual arm continuum robots have been investigated in the past for the use in minimally invasive surgery, especially single port access surgery, where only one incision is performed to deploy all tools required to perform the medical task. This includes, for instance, bimanual teleoperation of tendon actuated continuum robots (pick-and-place and knot tying) in (Bajo et al., 2012), as well as suturing and grape peeling in (K. Xu, Zhao, and Fu, 2014). The employment of CTCR as dual arms is investigated for teleoperation in endonasal skull base surgery and tumor removal in (Burgner, Rucker, et al., 2014). Further, dual-arm CTCR are incorporated into an endoscope for prostate surgery in (Hendrick, Herrell, Mitchell, et al., 2016; Hendrick, Herrell, and Webster III, 2014; Hendrick, Mitchell, et al., 2015). The authors in (Hendrick, Mitchell, et al., 2015) optimize the overlap of the endoscope field of view and CTCR workspace.

This chapter applies the proposed methods from Chapter 5 to design parameter optimization of two collaborating robotic arms (robot A and B), which are incorporated into a dual channel endoscope, see Figure 25.
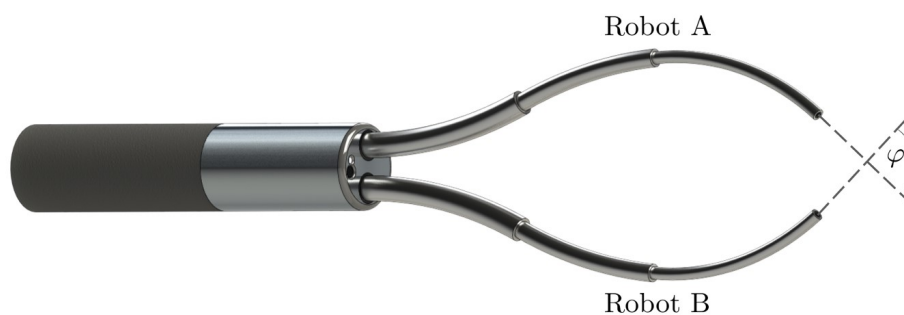
Figure 25: Dual arm channel endoscope with two CTCR arms working collaboratively on a medical task and triangulation angle φ.

6.2 OPTIMIZATION PROBLEM

As this application deals with dual arm CTCR, the optimization problem considers the design parameters of the two robotic arms. In particular, the aim is to enable collaborative task performance of the two end-effectors. Robot A and B are defined by the same design parameters with three tubes each. Parameters, the objective function, and constraints of this optimization application are explained in the following.

6.2.1 *Contribution*

This application requires the introduction of a novel objective that aims to optimize collaboration of the two robotic arms and ensures a specific triangulation between them. In the context of dual-arm CTCR, researchers consider the overlap of the endoscope field of view and CTCR workspace in (Hendrick, Mitchell, et al., 2015). However, none consider to aim for an optimized triangulation of the two arms. This thesis presents the first approach to optimize the design parameters of the two arms and aim for an advanced alignment. Further, it demonstrates that the presented methodology in Chapter 5 allows identifying parameters, the objective function, and constraints for single-, as well as multi-objective problems. Existing optimization approaches consider optimizing for curvature and curved length of a single robot, where this application considers the design parameters of robot A and B to enable interactive manipulation.

This example scenario is specifically selected as it can serve as proof for the applicability of the proposed algorithm. As this application requires the consideration of only one objective, the proposed particle swarm algorithm can be compared to the Nelder-Mead search applied to CTCR design optimization in the past. Convergence behavior, computation time and objective function values are compared for multiple optimization runs.

6.2.2 *Parameters*

This optimization problem is defined by robot-specific parameters and considers the following tube design parameters of the two robotic arms for optimization

- curvature κ_i, with $i \in [1, ..., 3]$,

- curved length ℓ_{c_i}, with $i \in [1, ..., 3]$.

Fixed design parameters and input to the algorithm are the number of tubes n, the diameters of each tube OD_i and ID_i, the straight lengths ℓ_{s_i}, and the elastic modulus E_i of the selected tube material (NiTi). OD_i and ID_i remain fixed during optimization, provided that the triangulation of the two end-effectors is decisively determined by the curvature and curved length of the tubes. The tube diameters and the distance between the arms at the base are driven by commercial dual channel endoscope designs. Typically, the channel diameters vary between 2 and 4 mm with a shift distance $S \simeq 5$ mm. This shift distance is considered as the offset between the two arms at the exit of the endoscope.

Further, this application targets the optimization of curvature and curved length for comparability. Performance of the Nelder-Mead algorithm for six parameters is shown in (Burgner, Gilbert, and Webster III, 2013).

6.2.3 *Objective*

The objective is application-specific and considers the pose of the two robotic arms to allow for an advanced triangulation. This optimization problem is defined as single-

objective and maximizes the number of collaborative configurations $n_{q_{A,B}}$ of robot A and B as

$$\text{maximize} \quad y = f(x) = n_{q_{A,B}} \quad \forall \, q_{A,B} \text{ with } \varphi \in [90°, 180°] \text{ and } |e_A - e_B| > d_E,$$

where $q_{A,B}$ defines a configuration of robot A and B, φ defines the triangulation angle between the robotic end-effectors, $|e_A - e_B|$ defines the Euclidean distance between them, and d_E is a user defined threshold. A configuration $q_{A,B}$ of robot A and B counts as collaborative, if a certain triangulation and Euclidean end-effector distance is guaranteed for task deployment. φ is defined as the angle between the two tangent curvature vectors $r_{z_{A,B}}$ at both end-effectors, as illustrated in Figure 25. The triangulation angle is selected to be $\varphi \in [90°, 180°]$, as this allows the end-effectors to be oriented towards one another to work simultaneously on a task. Thus, the aim of the optimization algorithm is to search for two robotic arm designs, which result in a maximum number of collaborative configurations with the specified triangulation angle. The triangulation angle φ is computed with

$$\varphi = \text{atan2}\left(\|r_{z_A} \times r_{z_B}\|, \, r_{z_A} \cdot r_{z_B}\right).$$

6.2.4 *Constraints*

The constraints are material and robot-specific, and the selected NiTi imposes a maximum limit on the curvature, such that the material remains within the elastic region. The constraints are parameter dependent as

- curvature $\kappa \in [\kappa_{min}, \kappa_{max}]$,

- curved lengths $\ell_c \in [\ell_{c_{min}}, \ell_{c_{max}}]$,

- $\kappa_1 > \kappa_2 > \kappa_3$,

- $\ell_{c_1} > \ell_{c_2} > \ell_{c_3}$.

6.3 IMPLEMENTATION

The aim is to determine optimal tube parameters (curvature and curved length) of the two robotic arms with maximum collaboration. A single-objective particle swarm optimization algorithm is applied as presented in Chapter 5. Here, a particle x_k is defined by the curved lengths ℓ_{c_i} and curvatures κ_i of each tube respectively as $x_k = [\kappa_i, \ell_{c_i}]$. To determine the objective function f for each particle x_k, the workspace of each CTCR is generated by creating uniformly distributed samples m_s for each robot as $q_{A,B_j} = [\alpha_1, \ldots, \alpha_i, \beta_1, \ldots, \beta_i]^T$ with $j \in [1, m_s]$. By utilizing the Cosserat rod forward kinematics model (see Chapter 2), the space curve $g(s)_j$ can be acquired for each sample j and robot. The triangulation angle φ is then computed for each permutation of robot A and B. Only those configurations $q_{A,B}$ count as collaborative that ensure the required triangulation angle and end-effector distance. The workflow of this optimization problem is illustrated in Figure 26. It illustrates the parameters,
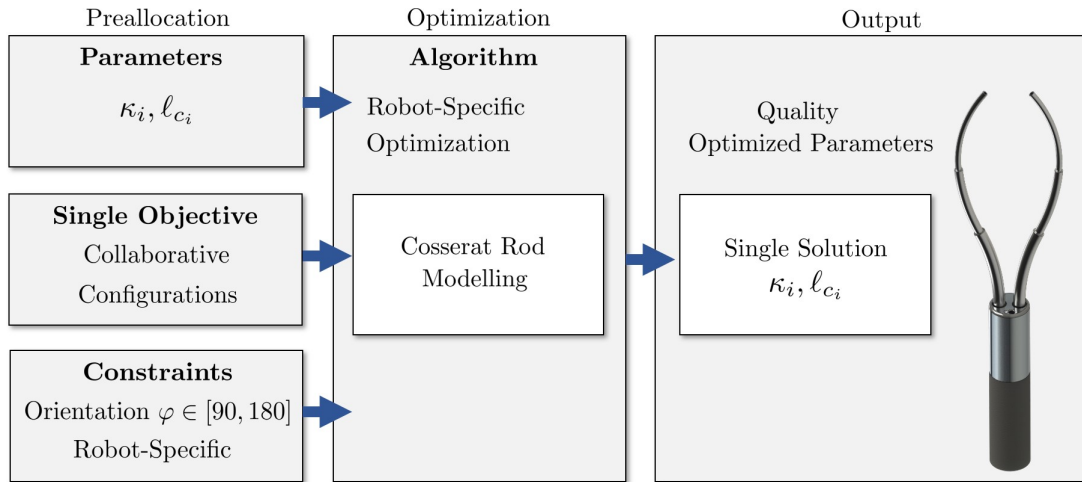
Figure 26: Optimization workflow for cooperative task deployment of two robotic arms with preallocation, optimization process, and output.

objective function, and constraints as input to the algorithm. The algorithm optimizes six parameters of robot A and B and the output is the optimal design set.

As this application utilizes a single-objective particle swarm optimization algorithm, the personal $\mathbf{p}_{b_k}^t$ and global best solutions $\mathbf{g}_b^t$ within a swarm are determined within each generation. The personal best parameter set $\mathbf{p}_{b_k}^t$ of a particle defines the set of parameters with the maximum value for f, as the aim here is to maximize the objective function. The global best parameter set $\mathbf{g}_b$ then describes the set of parameters with the highest cost across all particles and generations.

At the beginning of the algorithm, each particle is randomly initialized on a uniform distribution regarding the constraints of the optimization problem. If a particle exceeds a boundary, then the parameter is truncated regarding the specific constraint.

6.4 EVALUATION AND RESULTS

This section evaluates the performance of the single-objective particle swarm optimization algorithm. Its performance is then compared to the Nelder-Mead algorithm that has been applied to CTCR design problems in the past.

The number of tubes for both robotic arms is $n = 3$. All preselected design parameters are depicted in Table 1. The outer and inner diameter OD_i and ID_i are selected to fit through a commercial dual channel endoscope. Elastic modulus E_i and Poisson's ratio v are defined by the material NiTi.

The particle swarm algorithm is executed with $P = 20$ particles, $T = 100$, $\eta = 0.9$, and $c_1 = c_2 = 2$ (to ensure a compromise between exploration and convergence of the algorithm). All parameters are selected based on performance. r_1 and r_2 are real random numbers $\in [0, 1]$. The population size and number of generations are selected based on the recommendations in (Coello Coello and Lechuga Salazar, 2002; Shi and Eberhart, 1999). The population size is selected to be relatively low for computation reasons. Further, the parameter space is defined by only six parameters,

Table 1: Preselected tube design parameters.

parameter	OD in mm	ID in mm	E in GPa	ν	ℓ_s in mm
tube 1	1.21	0.67	60	0.3	250
tube 2	1.92	1.28	60	0.3	200
tube 3	2.74	2.08	60	0.3	150

such that a small population is assumed to be adequate. The curved lengths for each tube i are empirically selected to be within the range of $\ell_{c_i} \in [0, 100\,\text{mm}]$, and the curvature is selected to be within the elastic region of NiTi as $\kappa_i \in [0, 0.05\,\text{mm}^{-1}]$. The sampling size is $m_s = 500$ for robot A and B (empirically selected based on performance). This results in 250,000 possible combinations. However, only those configuration combinations are regarded as collaborative that exhibit the required end-effector distance d_E and triangulation angle φ.

The optimized tube design sets of the particle swarm algorithm for three optimization runs are depicted in Table 2. The corresponding convergence behavior is illustrated in Figure 27 (left). The first optimization (in blue) results in 198 collaborative configurations and the algorithm converges after approximately 40 iterations. The second optimization (in gray) results in 203 collaborative configurations and converges after approximately 75 iterations. The third optimization (in black) results in 199 collaborative configurations and converges after approximately 20 iterations. All optimizations result in a similar number of collaborative configurations, which proves the performance of the algorithm. Note, that the function value $f(\mathbf{x})$ can be quadruplicated through design optimization of the two robotic arms by the algorithm.

Table 2: Optimized tube design sets for particle swarm and Nelder-Mead optimization for multiple optimization runs. κ_i in mm^{-1} and ℓ_{c_i} in mm.

algorithm run	κ_1	κ_2	κ_3	ℓ_{c_1}	ℓ_{c_2}	ℓ_{c_3}
Particle Swarm 1	0.047	0.030	0.006	80.6	44.1	20.3
Particle Swarm 2	0.048	0.028	0.015	81.0	46.7	5.6
Particle Swarm 3	0.048	0.024	0.006	74.0	48.1	8.2
Nelder-Mead 1	0.034	0.011	0.003	37.0	74.7	92.0
Nelder-Mead 2	0.033	0.018	0.008	95.1	38.5	41.0

Considering the results in Table 2, it is noticeable that all three particle swarm optimizations result in a high curvature for tube 1. All other optimization parameters vary slightly but result in a similar objective function value due to tube interaction.

To verify the applicability of the particle swarm optimization algorithm for the structural design optimization of CTCR, this chapter compares the algorithm to the state of the art. The Nelder-Mead algorithm has been applied in the past to optimize CTCR design parameters (Bergeles, Gosline, et al., 2015; Burgner, Gilbert, and Web-
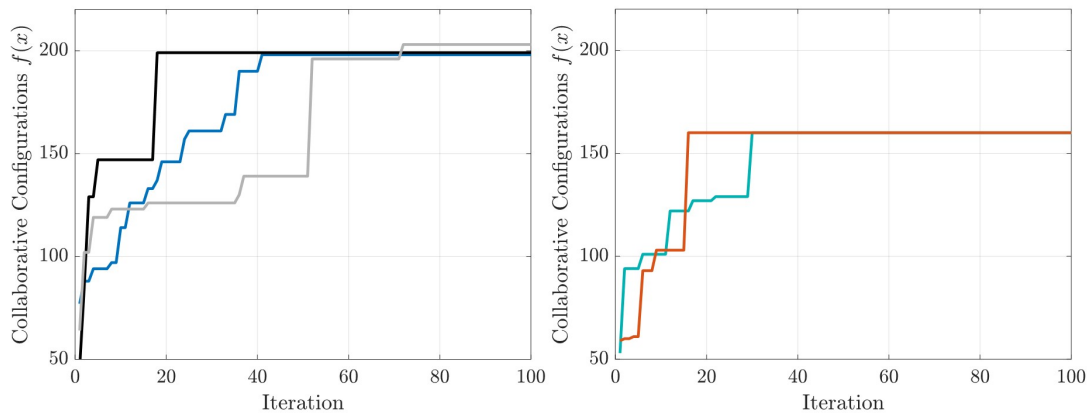
Figure 27: Convergence behavior of particle swarm optimization (left) and the Nelder-Mead algorithm (right) over t = 100 iterations for multiple optimization runs.

ster III, 2013). To compare the performance of the two algorithms, the Nelder-Mead search is initialized with 20 random parameter sets. The optimized tube parameters are also depicted in Table 2 and the convergence behavior in Figure 27 (right). The Nelder-Mead algorithm ran over 100 iterations and converges approximately after 30 iterations to 160 collaborative configurations (in turquoise). The second optimization results in 162 collaborative configurations (in orange) and converges after approximately 15 configurations. Notice, that tube curvatures are similar for the two optimizations, but curved section lengths vary considerably.

The algorithm has been implemented in Matlab on an Intel Core i7-4790 3.60 GHz. To limit computation time, the kinematic model has been loaded into Matlab as precompiled C++ code. Computation times for both algorithms are depicted in Figure 28. The run time per iteration is lower for the Nelder-Mead algorithm. Note, that the run time per iteration for the particle swarm algorithm depends on its population size. The mean convergence time is also lower for the Nelder-Mead algorithm; however, the particle swarm optimization algorithm achieves a higher function value for all optimization runs.

The mean function evaluation time over one generation is 22.7 s for particle swarm optimization. As the objective function for both optimizers is the same, the Nelder-Mead algorithm requires the same time for function evaluation. One call of the forward kinematics takes 0.02 s, measured as the mean over 500 samples.

Note, that the sampling size can be increased if computational power is not limited. This would lead to an increase in collaborative configurations. However, also a low sampling size can indicate a robotic design that offers an improved triangulation. Also, rotational symmetry within the workspace can be utilized to generate an increase in collaborative configurations.

A selection of the particle swarm optimization algorithm over the Nelder-Mead search is preferable to find the overall optimal design. The particle swarm algorithm may be able to overcome a local minimum found here by the Nelder-Mead algorithm. However, Nelder-Mead optimization may be preferable if computation time is limited.
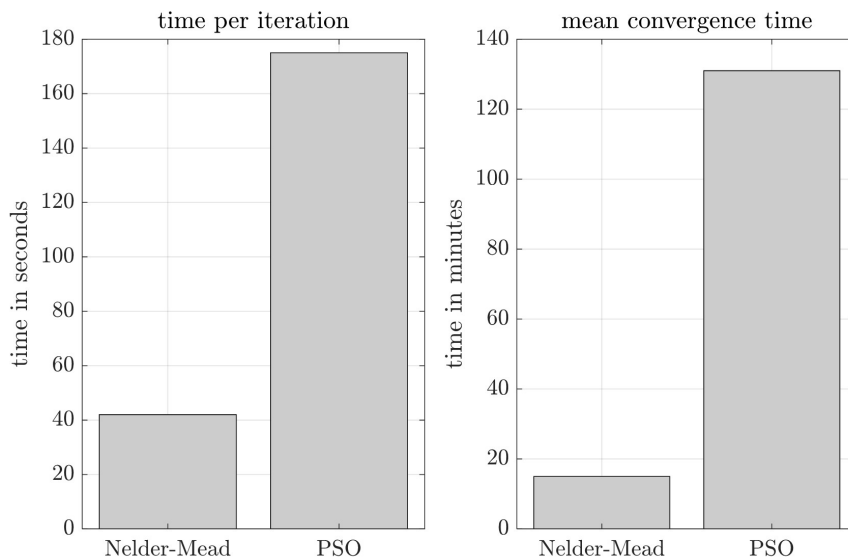
Figure 28: Run time for one iteration and the mean convergence time for the Nelder-Mead and particle swarm algorithms, respectively.

Figure 29 illustrates example collaborative configurations of the optimized robotic arms for the first particle swarm optimization run with a triangulation of $\varphi \in [90°, 180°]$ and end-effector distance $d_E < 5\,\text{mm}$. Note, that the Euclidean end-effector distance can be set to a different value dependent on the application.

6.5 CONCLUSION AND FUTURE WORK

This chapter presents a theoretical study towards the design of collaborative CTCR for contactless tasks. The optimization problem could be extended to multiple objectives if required in the future. This could include specific workspace constraints (manipulability, stability of the robots), or constraints for task deployment (body collision between the two robotic arms). A different relative distance between the two end-effectors or triangulation can be selected in the future but also variable relative distances are accountable.

The collaboration of two CTCR accounts for various applications, as this approach has the potential to reduce intervention time. Medical tasks could include, for instance, tissue manipulation, knot tying, deployment of tools, or cameras. This further enables the simultaneous performance of concurrent sub-tasks.

Most importantly, this study compares the performance of the particle swarm optimization algorithm to Nelder-Mead optimization. Results show that the single-objective particle swarm optimization algorithm results in higher objective function values than the Nelder-Mead algorithm but requires more computation time. Even though the proposed algorithm requires more function evaluations and time, it can be advantageous for those applications that are defined by more parameters and constraints. Particle swarm optimization has the potential to overcome local minima to converge towards a global optimum in a multidimensional constrained search

space. This study represents the first step to show the applicability of the particle swarm optimization algorithm towards the design optimization of CTCR.
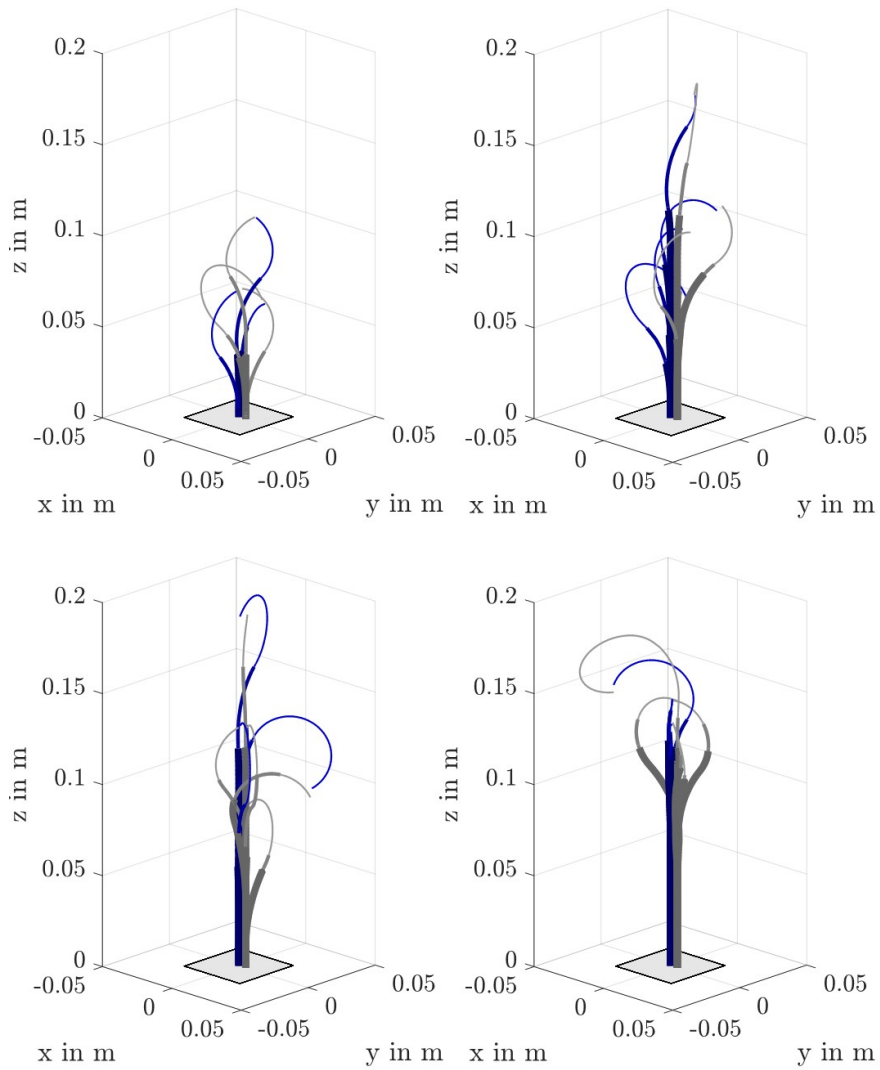

Figure 29: Collaborative configurations of the particle swarm design 1 with an optimal triangulation and end-effector distance for cooperative tasks.

7

STRUCTURAL STIFFNESS AND WORKSPACE OPTIMIZATION CONSIDERING EXTERNAL FORCES

This chapter applies the proposed methodology to the structural stiffness of CTCR and their force absorption capabilities. It considers the overall design space including the wall thickness and elastic modulus of the tubes. This is a multi-objective optimization problem with conflicting objective functions, which aims to increase workspace size while maintaining the structural stiffness of the tubes. The application of external forces is inspired by medical interaction forces during surgery. Further, force absorption capabilities within the overall workspace of the optimized design are compared with two existing state of the art designs.

The presented optimization methodology enables the identification of parameters, objectives, and constraints and utilizes the multi-objective particle swarm optimization algorithm to solve the problem regarding multiple Pareto optimal solutions.

7.1 MOTIVATION

This chapter considers the workspace and stiffness properties of CTCR. The aim is to use the CTCR as a medical device. Some minimally invasive applications require a large workspace of the robot to cover the overall surgical workspace (e.g. within the abdomen or lungs). The inherent flexibility of the CTCR and a large workspace extent are advantageous but the use of the CTCR as a medical device requires certain stiffness capacities of the backbone. This applies particularly if the manipulator is used for manipulation tasks in which it is exposed to external forces. To apply the required manipulation forces during surgery, the CTCR must have a certain stiffness and at the same time sufficient flexibility to cover a specific workspace.

Structural synthesis requires special attention since the stiffness of the CTCR is influenced by both geometrical and material properties. This parameter optimization thus considers the entire parameter space of CTCR (lengths, diameters, curvatures, and material parameters) to optimize the workspace size and provide the desired stiffness for manipulation task performance. An optimal stiffness is achieved through the optimization of the tube's wall thickness and elastic modulus. External forces resulting from manipulation tasks, which influence the shape of the robot backbone are taken into account. To perform the desired manipulation task, the CTCR is equipped with a tool at its end-effector, as illustrated in Figure 30.
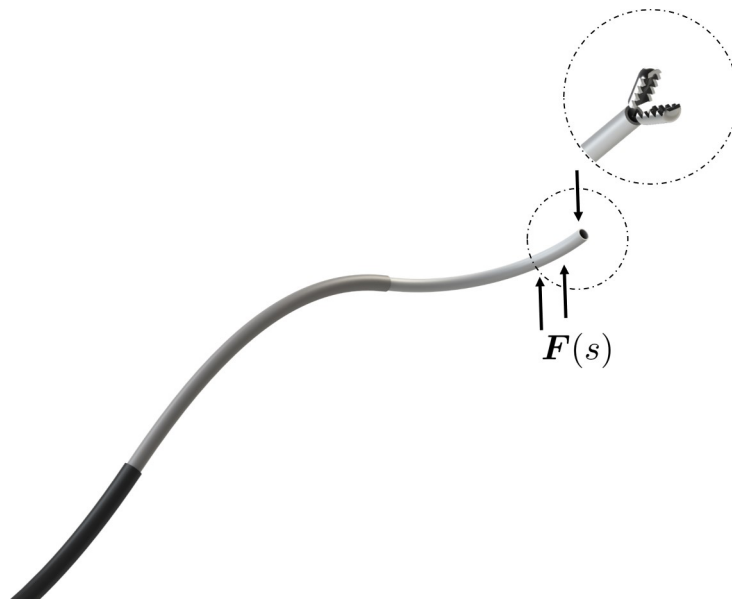

Figure 30: CTCR equipped with a gripper at its tip for manipulation task performance. External point forces $\mathbf{F}(s)$ are applied onto the robotic structure during task performance.

CTCR have been proposed for various applications, however, the investigation of manipulator stiffness and force absorption capabilities remain relevant and challenging research objectives. Forces in minimally invasive surgery have been investigated in the sense of force feedback for other robotic systems. The authors in (U. Kim et al., 2015) investigate pulling forces in minimally invasive surgery using a 4DOF force sensor. A special tool with force measuring capabilities has been developed for

their robot system to measure the pulling forces during manipulation. The measured pulling forces of tissue depend on the gripper opening angle Ω, as illustrated in Figure 31, but the maximum forces are measured to be 1.45 N, 0.21 N, and 0.15 N in x,y, and z-direction with a magnitude of 1.47 N. In the following, these pulling forces are regarded as reference.
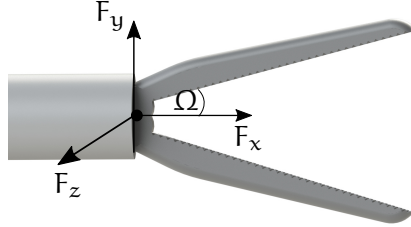

Figure 31: Pulling forces acting on the gripper in x,y,z-direction.

Thus far, different tube materials have been proposed for CTCR. These include the superelastic shape memory alloy NiTi (Nickel-Titanium alloy), but also 3D printed thermoplastic materials like PLA, PCL, and nylon (Amanov, Nguyen, and Burgner-Kahrs, 2015; Morimoto and Okamura, 2016). This application might require materials with higher stiffness, such as CuZnAl (Cooper-Zinc-Aluminum alloy) or CuAlNi (Copper-Aluminium-Nickel alloy). These alloys exhibit a higher Elastic modulus compared to NiTi and are thus stiffer. The elastic modulus E and strain rate ϵ are depicted in Table 3 for different tube materials. The Poisson's ratio is assumed to be 0.33 for metals. These are considered as tube material in the following.

Table 3: Material properties of different alloys. Based on (Huang, 2002; Jani et al., 2014)

Properties	Elastic modulus E in GPa	Strain rate ϵ
NiTi	28-83	8%
CuZnAl	70-100	$4-5\%$
CuAlNi	80-100	$3-5\%$

7.2 OPTIMIZATION PROBLEM

The aim is to determine optimal tube parameters of the CTCR to allow for an increased workspace size while optimizing for a robotic design that exhibits enough stiffness to absorb external manipulation forces. This is a problem with conflicting objectives as stiffness and workspace size are inevitably competing. Here, the multi-objective optimization methodology can be applied to optimize for workspace size and stiffness simultaneously. The manipulation forces considered here are analogous to the pulling forces mentioned in Section 7.1. In the context of this application, external manipulation forces $\mathbf{F}$ are applied to the tip of the unloaded robot $\mathbf{g}(s)^\star$. This point force application results in a deflection represented by the loaded backbone $\mathbf{g}(s)$, illustrated in Figure 32. In summary, this optimization determines optimal

robotic parameters to enlarge workspace size while minimizing the deflection according to external forces within the workspace.
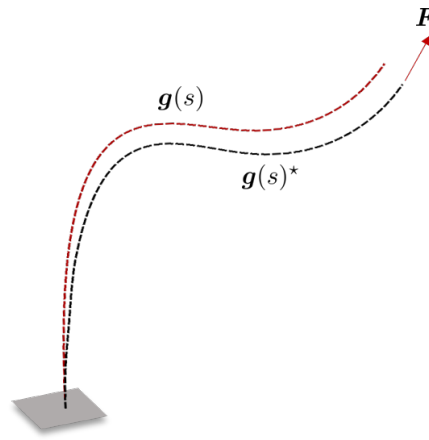

Figure 32: The unloaded $g(s)^\star$ and loaded CTCR $g(s)$ with external point force $\mathbf{F}$.

7.2.1 *Contribution*

This chapter applies the presented optimization methodology from Chapter 5 to the structural stiffness and workspace optimization of CTCR. The optimization problem presented here considers geometric, as well as material properties for the first time. This includes the tube's lengths, diameters, wall thickness, and material properties of different shape memory alloys. Additionally, the consideration of external forces within the design optimization procedure is novel to the state of the art. Two objectives are introduced that allow optimizing for an increased workspace, and the minimization of the deflection according to external forces.

This thesis investigates the CTCR's ability to withstand forces and examines the relationship between stiffness versus flexibility. The robot is required to exhibit certain flexibility to increase workspace size while retaining enough stiffness to absorb external forces.

In terms of stiffness, researchers investigate the patterning of tubes that can lead to a different stiffness behavior in (Azimian et al., 2014; J. S. Kim et al., 2014; D. Y. Lee et al., 2015). However, the authors concentrate on improved stability of the robot to reduce friction between the tubes and snapping (rapid rotational motion of a tube) during deployment. External forces are investigated in terms of force sensing, e.g. in (R. Xu, Yurkewich, and Patel, 2016), using FBG force sensors. The authors aim to measure curvature, torsion, and forces and develop a force-curvature-strain model to incorporate their measurements into kinematic modeling. Force measurements can be utilized in the future to account for robot-tissue interactions. In the context of design optimization, this is the first work that considers the stiffness of the tubes (diameter of the tubes and elastic modulus) within the design optimization procedure. Additionally, external forces are included for the first time. This is essential to determine a tube design that is eventually capable to withstand and absorb the occurring external forces during manipulation. Further, two novel objective functions are

presented. The first objective represents an approximation of the planar workspace size of the CTCR, and the second objective characterizes the deflection according to external forces. The formulation of two conflicting objective functions with the application to multi-objective optimization is novel to the state of the art.

7.2.2 *Parameters*

The parameter space for this particular problem is diverse and the optimization parameters are the

- inner diameter ID_i,

- outer diameter OD_i,

- tube curvature κ_i,

- tube curved length ℓ_{c_i},

- elastic modulus E_i with $i \in [1, ..., n]$.

The elastic modulus corresponds to a specific alloy with the respective strain rate ϵ, and Poisson's ratio ν. The straight tube length ℓ_{s_i} remains fixed during optimization and $n = 3$.

7.2.3 *Objectives*

Objectives here aim to increase workspace size, as well as minimize the deflection according to external forces. The objectives are conflicting, as an increase of workspace size does not necessarily result in an increased stiffness to absorb the occurring external forces. In fact, an increased stiffness of the CTCR (with short tubes and maximum wall-thickness) and high corresponding force absorption capabilities leads to a narrow and small workspace. Thus, the optimization problem is defined as multi-objective

$$\text{minimize } \mathbf{y} = f(\mathbf{x}) = (f_1(\mathbf{x}), f_2(\mathbf{x})),$$

where f_1 describes the workspace size and f_2 is the deflection as a result to external manipulation forces. The conflicting objective functions f_1 and f_2 imply that there exist no two solution vectors $\mathbf{x}$ and $\mathbf{x}^*$, where $(f_1(\mathbf{x}) \prec f_2(\mathbf{x}^*))$ or $(f_2(\mathbf{x}^*) \prec f_1(\mathbf{x}))$. Since the workspace size requires maximization and the deflection minimization, f_1 is represented by a negative number. This enables the minimization of both objective functions.

7.2.3.1 *Objective Function f_1*

To determine the size of the workspace for a tube parameter set $\mathbf{x}$ (i.e. each particle) and evaluate the cost $\mathbf{y}$, the discretization approach is used for workspace approx-

imation. The rotational parameters α_i remain unactuated, while the translational parameters are actuated using the following three sequences and intervals

1. $\beta_1 \in [-\ell_1, -\ell_2]$, $\beta_2 = -\ell_2$, $\beta_3 = -\ell_3$.
2. $\beta_1 \in [-\ell_2, -\ell_3]$, $\beta_2 \in [-\ell_2, -\ell_3]$, $\beta_3 = -\ell_3$.
3. $\beta_1 \in [-\ell_3, 0]$, $\beta_2 \in [-\ell_3, 0]$, $\beta_3 \in [-\ell_3, 0]$.

These sequences are executed after one another. The size of the translational increments $\triangle\beta$ is set to 1 mm. For each sample $\mathbf{q} = [\beta_1, \beta_2, \beta_3]$ the forward kinematics (Cosserat rod modeling) is used to determine the space curve $g(s)_{\mathbf{q}}^*$. Note, that this leads to a representation of end-effector positions in one plane, as the rotational parameters remain unactuated. The generated end-effector points represent the right border of the workspace. The left border is represented by the z-axis (due to rotational symmetry) and the top border is a line from $[0, z_{max}]$ to $[x_{max}, z_{max}]$. This is illustrated in Figure 33 (left). Using this discretization, the size of the workspace can be approximated by computing the area of the polygon, which is defined by all border points. As the workspace of the CTCR exhibits rotational symmetry, the area of the polygon W_P can be an indicator for the size of the overall workspace as

$$f_1(\mathbf{x}) = W_P.$$

This approximation requires considerably less computation time compared to a three-dimensional random sampling-based approach.

7.2.3.2 *Objective Function f_2*

Objective f_2 accounts for the deflection of the backbone as a result of external forces

$$f_2(\mathbf{x}) = \frac{1}{N} \sum_{j=1}^{N} \left(\frac{1}{M} \sum_{d=1}^{M} |\mathbf{p}_{d_j}^* - \mathbf{p}_{d_j}| \right),$$

where M defines the number of equidistant backbone points of the unloaded $\mathbf{p}^*$ and of the loaded backbone $\mathbf{p}$. The deflection is measured along the entire backbone to obtain a measure that reflects the overall stiffness of the manipulator. N defines the number of configurations. To determine the force absorption capabilities of the investigated parameter set, external forces are applied to the unloaded robot in tangential direction at the tip to account for pulling forces, see Figure 33 (right). Here, the external point forces are applied to the following configurations $\beta_1 = \beta_2 = \beta_3 = -\ell_3$ and $\beta_1 = \beta_2 = \beta_3 = 0$, α_i remain unactuated. These configurations represent examples where the tubes are extended and the robot has a low load capacity.

7.2.4 *Constraints*

The geometric and material parameters of the CTCR impose constraints, as they have to remain within their defined parameter space. The following constraints apply

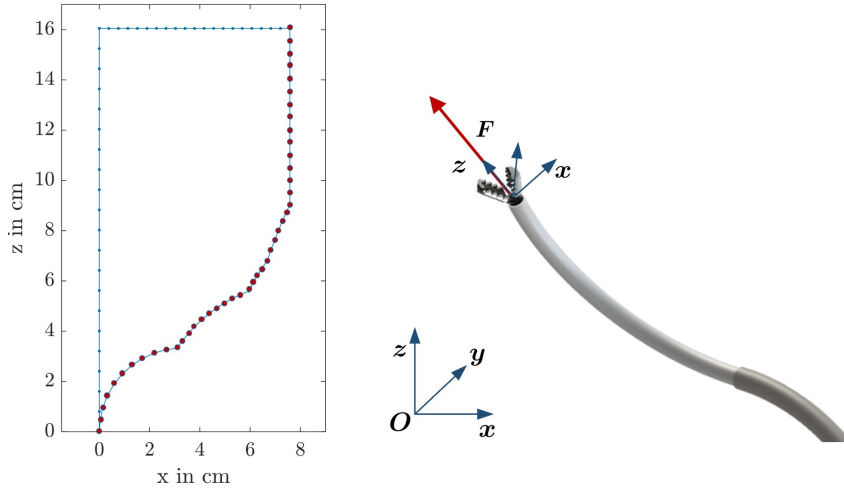- inner diameter $ID_i \in [ID_{i_{min}}, ID_{i_{max}}]$,

Figure 33: Planar workspace approximation. The red points mark the end-effector positions generated through the discretization (left). Robot in its undeformed state with external point force $\mathbf{F}$ in tangential direction to account for pulling forces (pointing in z-direction of the local coordinate system) (right).

- outer diameter $OD_i \in [OD_{i_{min}}, OD_{i_{max}}]$,

- tube clearance $c < c_{min}$,

- tube curvature $\kappa_i \in [\kappa_{i_{min}}, \kappa_{i_{max}}]$,

- tube curved length $\ell_{c_i} \in [\ell_{c_{i_{min}}}, \ell_{c_{i_{max}}}]$,

- elastic modulus $E_i \in [E_{i_{min}}, E_{i_{max}}]$.

Additionally, the overall design of the robot requires $ID_1 < OD_1 < \cdots < ID_n < OD_n$, c considers the minimum clearance between the tubes, $\kappa_{i_{max}}$ has to remain below a certain threshold such that the material remains within the elastic region, and the constraint for E_i depends on the Poisson's ratio ν of the respective material and vice versa. Further, $\kappa_1 > \kappa_2 > \kappa_3$ and $\ell_{c_1} > \ell_{c_2} > \ell_{c_3}$ apply here.

7.3 IMPLEMENTATION

Here, the particle swarm optimization algorithm considers multiple objectives f_1 and f_2. The decision vector is defined by the following set of parameters: $\mathbf{x}_k = [ID_i, OD_i, \kappa_i, \ell_{c_i}, E_i]$, with the inner and outer diameter, curvature, curved length, and elastic modulus of each tube i respectively. As this problem has two conflicting objectives, the concept of Pareto optimality is applied (see Chapter 5). The cost of each particle is defined as $\mathbf{y} = [f_1, f_2]$. The corresponding workflow of this optimization is presented in Figure 34. The input to the optimization algorithm are parameters, objectives, and constraints. The constraints are robot-specific design parameters and the external forces $\mathbf{F}$. During optimization, Cosserat rod modeling is applied to determine the deflection of the robotic backbone according to the external

forces. The output is a Pareto optimal set considering the two objective functions. A solution is then manually selected from the front.

To enforce constraints of this problem the upper and lower boundary for each parameter are considered. If a particle's parameter exceeds this boundary, it is repositioned to the nearest value within the parameter space.
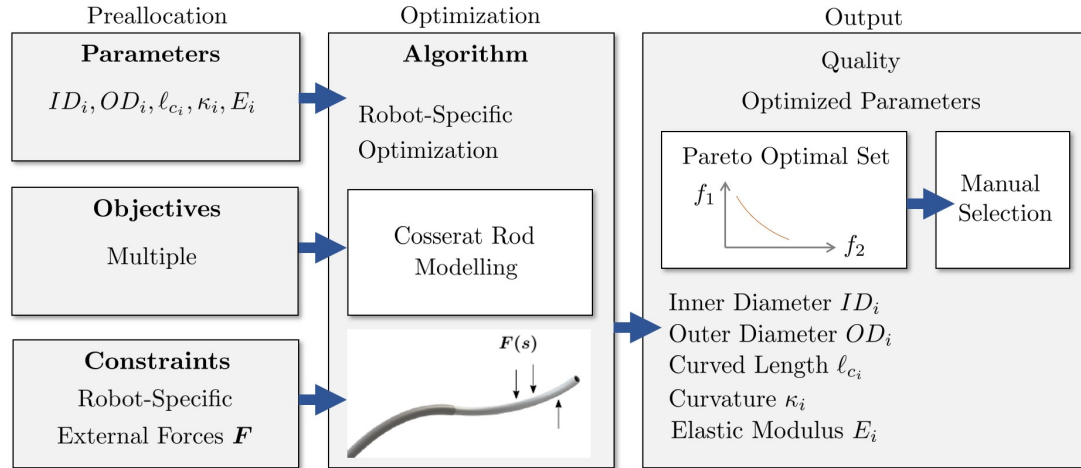

Figure 34: Design optimization workflow with preallocation, optimization, and output.

7.4   EVALUATION AND RESULTS

The optimization methodology applied here aims to optimize the CTCR's structural stiffness, and workspace considering external forces. The first evaluation applies the proposed algorithm, while the second evaluation investigates the force absorption capabilities of the optimized design.

7.4.1   *Workspace and Stiffness Optimization*

The multi-objective particle swarm optimization algorithm is executed with $P = 50$ particles, $T = 100$ generations, inertia weight $\eta = 1.4$ and $c_1 = 1, c_2 = 2$. All parameters are selected based on performance. r_1 and r_2 are real random numbers $\in [0, 1]$. The population size and inertia weight are increased in comparison to the previous application, as this optimization problem is defined by a larger parameter set. A higher inertia weight ensures a better exploration of the search space and an increased population size ensures diversity. The global confidence c_2 is increased for the same reason.

Each particle is initialized on a uniform random distribution within parameter constraints. Constraints are selected as: inner diameter $ID_i \in [0.2\,\mathrm{mm}, 3.3\,\mathrm{mm}]$, outer diameter $OD_i \in [0.3\,\mathrm{mm}, 3.5\,\mathrm{mm}]$, lengths $\ell_{c_i} \in [50\,\mathrm{mm}, 150\,\mathrm{mm}]$, curvatures $\kappa_i \in [0.005\,\mathrm{mm}^{-1}, \kappa_{i_{max}}]$, and elastic modulus $E_i \in [60\,\mathrm{Gpa}, 100\,\mathrm{GPa}]$. The minimum tube clearance is $c < 0.5\,\mathrm{mm}$, and the minimum wall thickness is $0.2\,\mathrm{mm}$. The upper boundary for the outer diameter of tube 3 is selected to be $3.5\,\mathrm{mm}$, as a higher diameter is not preferable for the intended applications of CTCR. $\kappa_{i_{max}}$ is either the maxi-

mum allowed curvature to remain within the elastic region or defined as $0.06\,\mathrm{mm}^{-1}$. The upper and lower boundaries for the elastic modulus are selected based on the presented materials in Table 3. For fabrication convenience, it is assumed that all tubes are made from the same alloy. All other boundaries are empirically chosen. The maximum curvature $\kappa_{i_{max}}$ is adjusted during optimization, as the outer diameter is an optimization parameter. The straight section lengths are selected to be $\ell_{s_1} = 150\,\mathrm{mm}$, $\ell_{s_2} = 100\,\mathrm{mm}$, and $\ell_{s_3} = 50\,\mathrm{mm}$, all empirically chosen.

Figure 35 illustrates the convergence behavior of the Pareto front for $P = 50$ particles after initialization, 10, 50, and 100 iterations. The Pareto front is depicted with respect to the mean deflection of the robotic backbone and the planar workspace size. Notice, that the particles on the front differ only slightly from 50 to 100 iterations, which indicates that the front converges. The archive size is 10, 17, 26, and 30 particles, respectively.
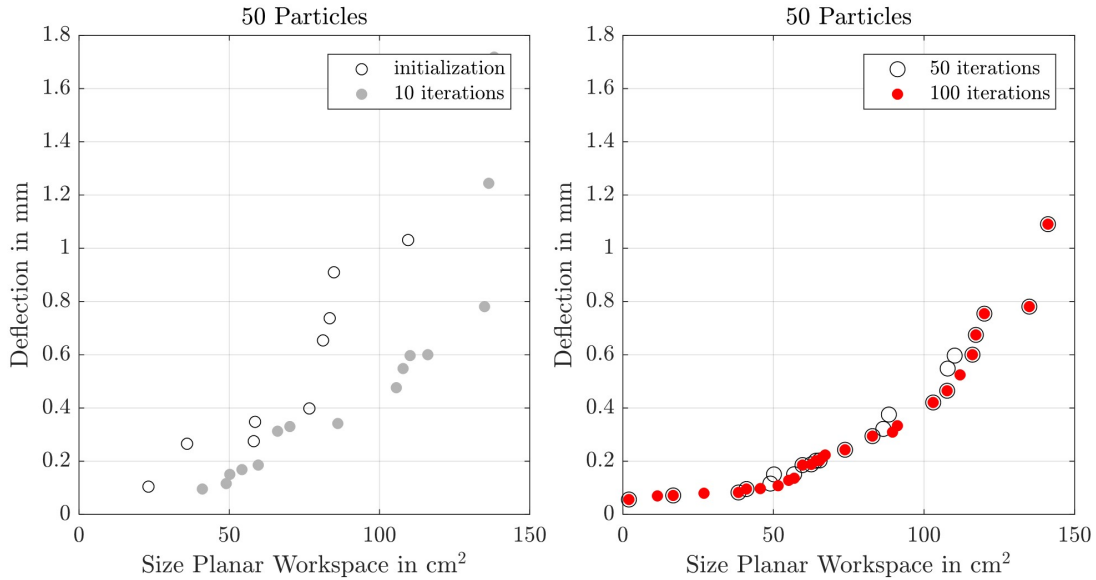

Figure 35: Development of the Pareto front after 50 and 100 iterations with respect to planar workspace size and deflection. Population size is selected to be $P = 50$.

The algorithm is executed for four optimization runs utilizing $P = 50$ particles. Figure 36 illustrates the result and shows that the optimization algorithm results in a similar Pareto optimal set after 100 iterations. The solutions distribute between the two objective functions, which proves that they are conflicting.

Note, that the Pareto front is sparse for larger workspaces and deflections. This could be explained by the fact that it is difficult for the algorithm to find solutions with higher stiffness, as the outermost tube diameter and the elastic modulus are constrained. The continuity of the front could potentially be increased through larger population sizes. However, since a solution with a compromise between planar workspace size and deflection is sought, solutions with extreme function values are not required.
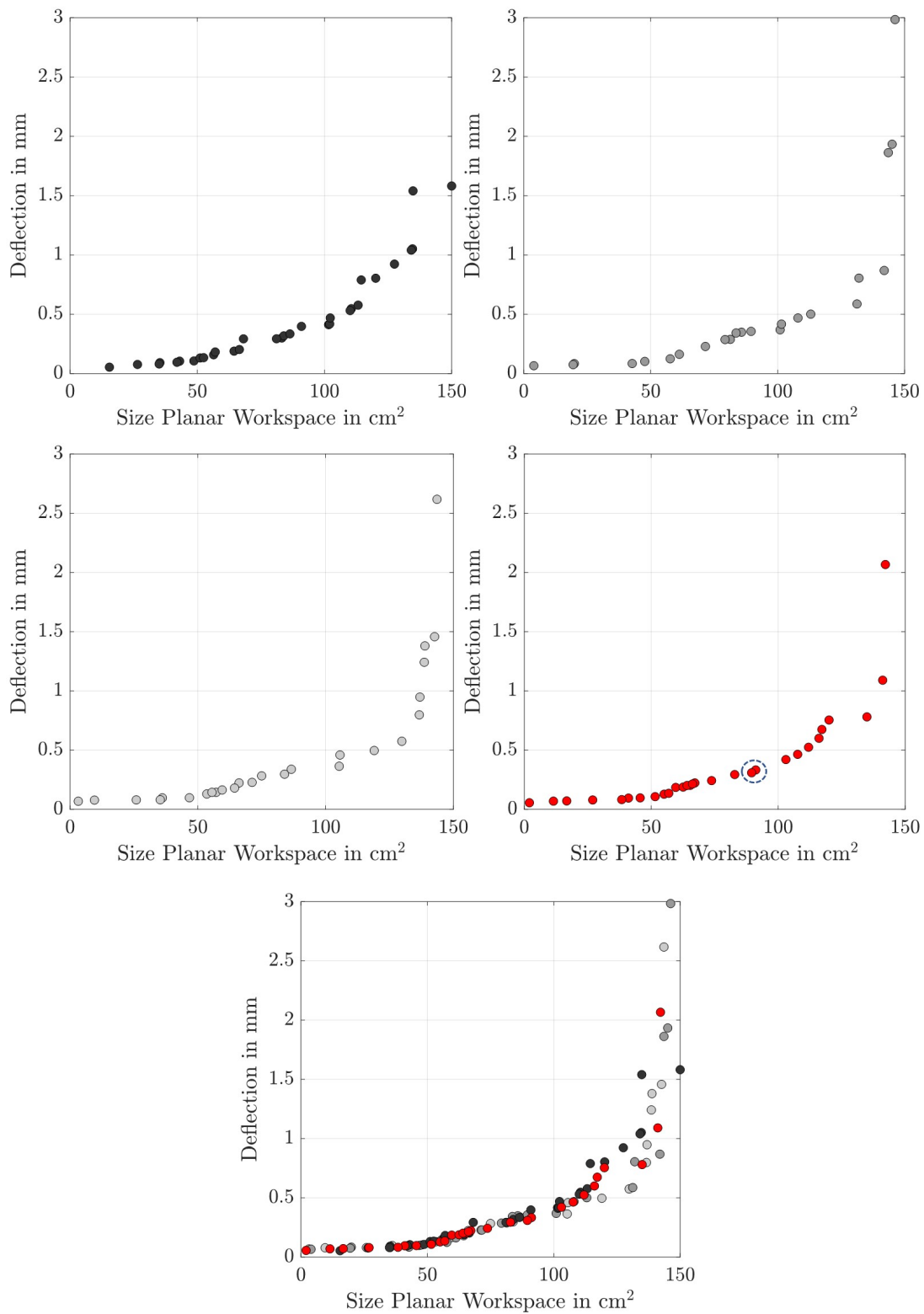
Figure 36: Four optimizations with $P = 50$ and $T = 100$. Objective function f_1 represents the planar workspace size and objective f_2 the mean deflection. The figure on the bottom illustrates all four optimizations.

A solution is then selected from the front that represents a compromise between workspace size and deflection, marked by a circle in Figure 36. The selected parameter set has a planar workspace size of $91\,\text{cm}^2$ and a mean deflection with extended tubes of $0.33\,\text{mm}$. All optimized tube parameters are illustrated in Table 4. Notice, that the optimized design exhibits the maximum allowed outer diameter for tube 3. The elastic modulus is $95\,\text{GPa}$. This means that a different material than NiTi must be selected as tube material.

The algorithm has been implemented in Matlab on an Intel Core i7-4790 3.60 GHz and the computation time for 100 iterations was $22\,\text{h}$. The mean run time for one generation is $13\,\text{min}$, for function evaluation it is $14.18\,\text{s}$, to enforce constraints it is $4.2\,\text{ms}$. To decrease computation time, the forward kinematics including external forces has been compiled as C++ code and converted into Matlab executable commands. Over 100 calls of the function, execution takes $0.54\,\text{s}$ on average with external forces.

Table 4: Optimized tube design parameters of the selected solution from the first Pareto front.

parameter	tube 1	tube 2	tube 3
OD in mm	2.48	3.08	3.5
ID in mm	1.05	2.75	3.29
E in GPa	95	95	95
ℓ_c in mm	84	78	56
κ in mm^{-1}	0.0297	0.0150	0.0095

7.4.2 *Workspace Analysis*

This section aims to investigate the stiffness and force absorption capabilities of the selected and optimized design within the overall workspace. Further, it is compared to two existing state of the art designs.

In particular, this considers the deflection of the CTCR's backbone according to external forces at the tip. The analysis proceeds as follows. $m_s \times n$ uniform randomly distributed samples are drawn for each configuration $\mathbf{q}$. The space curve $\mathbf{g}(s)^*$ for each configuration $\mathbf{q}$ is then computed using Cosserat rod theory. Three-dimensional external forces $\mathbf{F}$ with a magnitude of $1.47\,\text{N}$ are applied to the tip of each backbone $\mathbf{g}(s)^*$. The force direction vector is randomly determined to point away from the end-effector to account for a pulling force at the tip. The deflection between $\mathbf{g}(s)^*$ and $\mathbf{g}(s)$ then accounts for the force absorption capabilities of the investigated tube design. The deflection is defined as the sum of all Euclidean distances between each point along $\mathbf{g}(s)^*$ and $\mathbf{g}(s)$, where the points are equidistant along each curve.

The first CTCR design is from (Burgner, Swaney, Rucker, et al., 2011), which is optimized for endonasal skull base surgery. The second design is from (Burgner, Gilbert, and Webster III, 2013) and is optimized for transnasal surgery. All corresponding design parameters are depicted in Table 5 and Table 6, respectively. In both appli-

cations, the optimization parameters are the curvature and curved section length of each tube respectively, where the outer tubes are selected to be only straight.

Table 5: Optimized tube design parameters for endonasal skull base surgery from (Burgner, Swaney, Rucker, et al., 2011).

parameter	tube 1	tube 2	tube 3
OD in mm	1.64	2.29	3.05
ID in mm	1.4	2.04	2.8
E in GPa	60	60	60
ℓ_c in mm	60.6	60.2	0
κ in mm^{-1}	0.0185	0.0084	0

Table 6: Optimized tube design parameters for transnasal surgery from (Burgner, Gilbert, and Webster III, 2013).

parameter	tube 1	tube 2	tube 3
OD in mm	1.17	1.68	2.32
ID in mm	0.76	1.35	1.87
E in GPa	60	60	60
ℓ_c in mm	74.8	68.1	0
κ in mm^{-1}	0.0128	0.0109	0

The analysis of the force absorption capabilities for all tube sets considering 100 configurations and external forces with a magnitude of 1.47 N is illustrated using box plots. Figure 37 (left) represents the overall box plot and Figure 37 (right) illustrates the deflection for the tube set for endonasal surgery in comparison to the optimized tube set. The red line indicates the median values, the box upper, and lower quartiles, the whiskers indicate the minimum and maximum values, and outliers are depicted in red. Results show that the tube set for transnasal surgery exhibits the largest deflections as a result of external forces. The tube set for endonasal skull base surgery follows as the maximum deflection across all configurations is the second highest. Overall, the optimized tube set exhibits the best force absorption capabilities. The mean deflection for the tube set for endonasal skull base surgery is 5.2 mm, for transnasal surgery it is 31.4 mm, and for the optimized design it is 1.4 mm. The maximum deflection for the tube set for endonasal skull base surgery is 35.7 mm, for transnasal surgery it is 146.61 mm, and for the optimized design it is 4.14 mm. The design for transnasal surgery results in the largest deflections, as it has a lower wall thickness and tube diameter. Further, the second design features long tubes that lead to a higher deflection. Notice, that the optimized design has tubes with overall higher curvature to increase the workspace extent in x/y-direction.

To investigate the workspace extent, its planar size is determined by the approximation method proposed in this chapter. The result for all three tube designs is depicted in Figure 38. Notice, that the optimized design exhibits the second largest
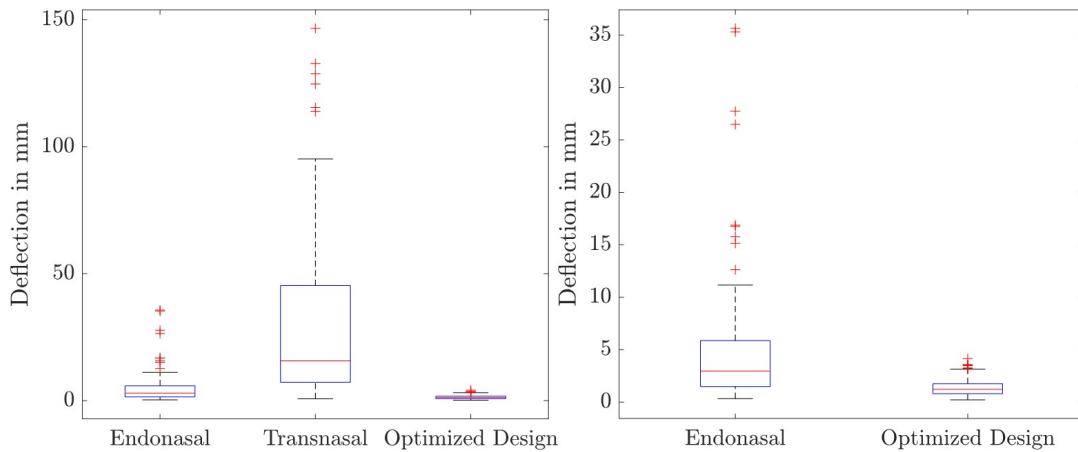
Figure 37: Box plot for the deflection according to the applied external forces for all tube sets. The red line indicates the median, the box upper and lower quartiles, the whiskers indicate the minimum and maximum values, and outliers are depicted in red.

workspace extent. Its planar size is lower compared to the design for transnasal surgery, as it represents a compromise between workspace size and deflection. To
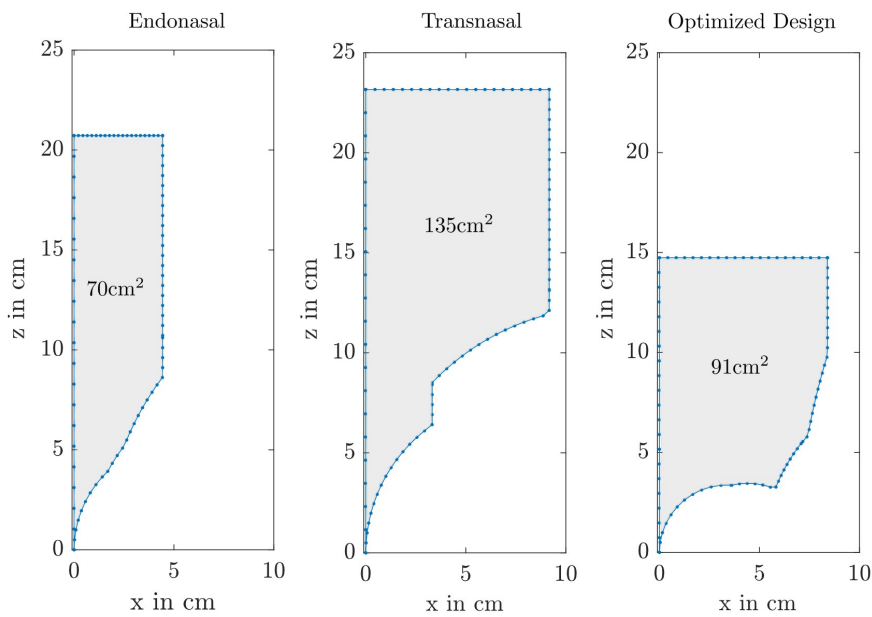

Figure 38: Planar workspace approximation for all tube designs.

verify the proposed planar workspace approximation, 10,000 uniform random distributed samples for $\mathbf{q}$ are drawn to approximate the configuration space Q. The corresponding end-effector positions and the planar workspace are illustrated in Figure 39. Notice, that the planar workspace represents the size of the randomly sampled workspace for the tube design for endonasal surgery. The actual workspace size for the optimized tube design is larger compared to the planar representation, as the extent in z-direction is created by the rotation of tubes against one another. However, the planar workspace approximation can be an indicator for the actual size if compu-
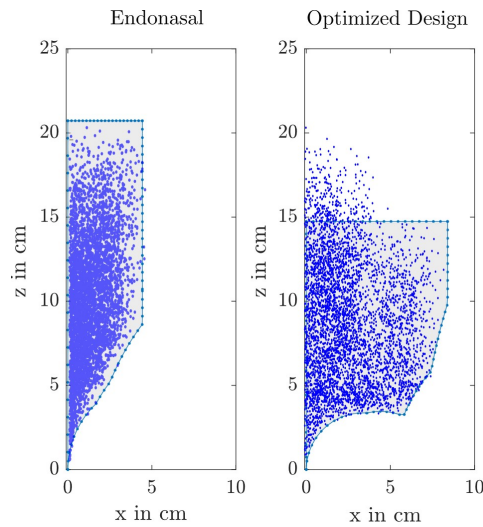
Figure 39: Planar workspace representation and randomly sampled end-effector points in blue for two robotic designs (endonasal skull base surgery and optimized design).

tational time is limited and time for function evaluation must remain at a minimum. Further, the extent in x/y-direction is of higher interest, as the extent in z-direction can be increased through an increase of straight section lengths. If computation time is not limited, then the sampling of the configuration space or further discretization including the rotation of the tubes is preferable.

5 example configurations for all investigated tube designs are depicted in Figure 40, Figure 41, and Figure 42, respectively. The unloaded backbone is depicted in gray and the loaded backbone in blue. Randomly generated three-dimensional forces with a magnitude of $1.47\,\mathrm{N}$ are applied to the tip of the robot and result in the illustrated deflections. Notice, that the optimized tube design exhibits only small deflections.
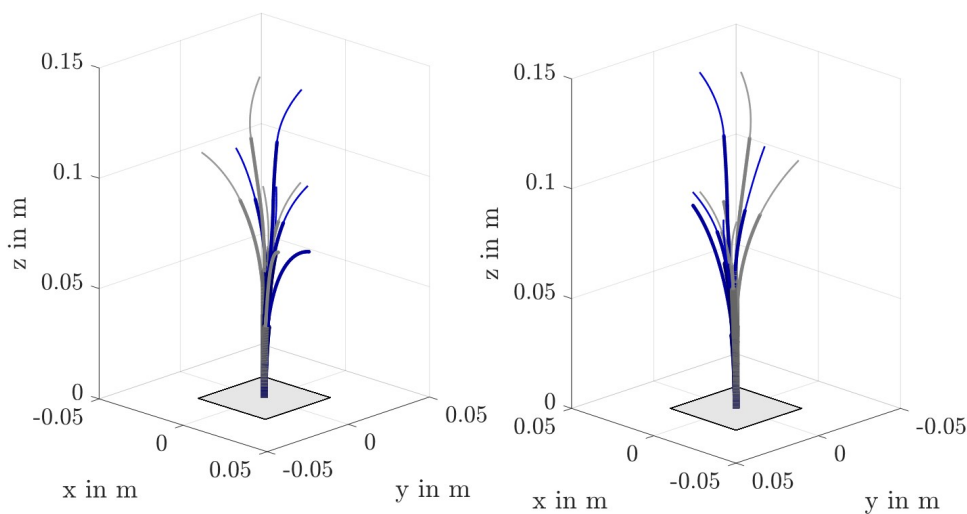

Figure 40: Unloaded (gray) and loaded (blue) robotic configurations of the optimized tube design for endonasal surgery.
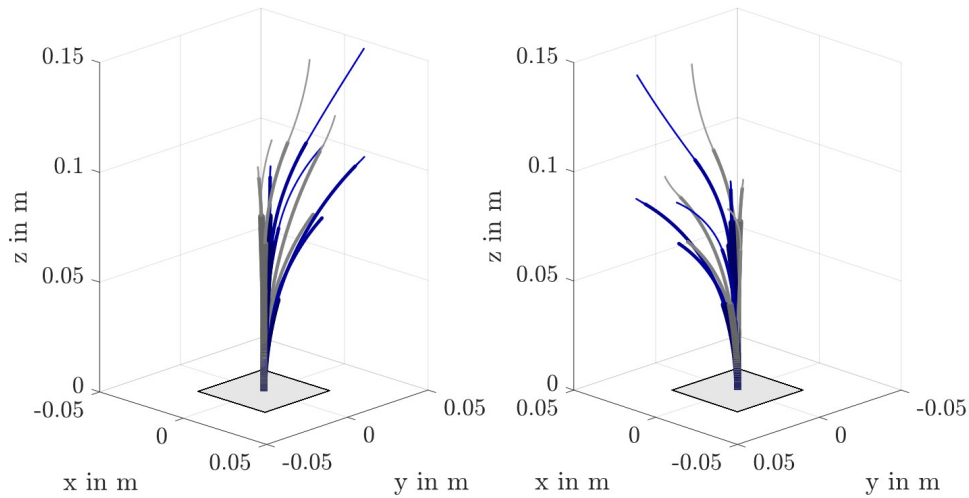
Figure 41: Unloaded (gray) and loaded (blue) robotic configurations of the optimized tube design for transnasal surgery.
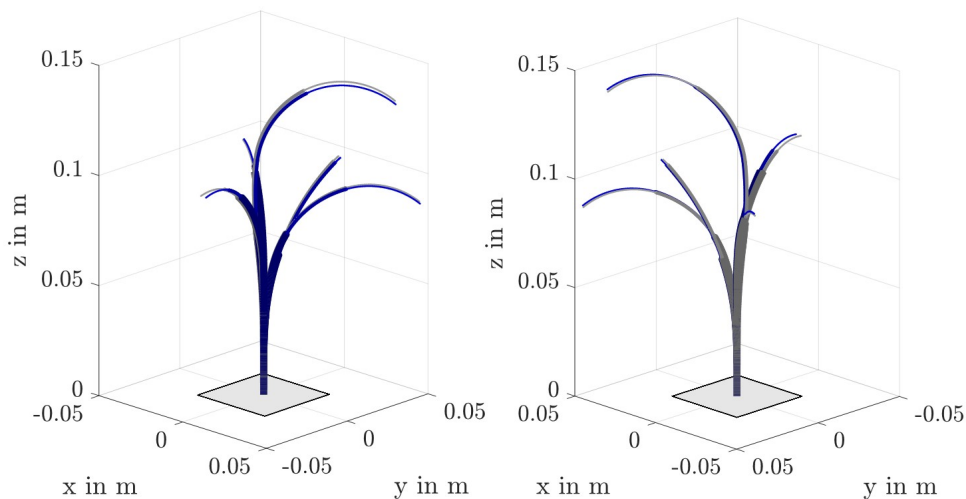

Figure 42: Unloaded (gray) and loaded (blue) robotic configurations of the first optimized tube design.

7.5 CONCLUSION AND FUTURE WORK

The investigation of existing tube designs results in large deflections within the workspace for some configurations. This proves the necessity to include parameters that affect the robot's stiffness into the optimization procedure. This chapter presents the first work on design optimization of CTCR considering external forces and the stiffness of the manipulator. It shows that the presented optimization methodology applies to the structural stiffness optimization of CTCR. This is the first work to consider the diameters and elastic modulus into the design optimization procedure. The state of the art considers up to six design parameters for optimization, while this optimization considers 13 parameters.

Two conflicting functions are included in the procedure and a Pareto optimal set is achieved. The solutions distribute between the two objective functions and the development of the Pareto front proves that the two are conflicting. It demonstrates that the algorithm can account for the multidimensional parameter space. Further, the two objective functions are novel to the state of the art. The planar workspace approximation can be utilized for various applications to limit computation time. It can also be utilized to determine the reachability of a target.

Future work demands the consideration of tube materials with increased stiffness. The selection of NiTi and especially 3D printed materials as tube material might not be appropriate for those tasks that require high manipulation forces.

This means that control algorithms must consider the behavior of the robot under external forces. Further, motion planning algorithms could avoid configurations that exhibit low force absorption capabilities. Future research can investigate the effect of external forces on the overall structure of the CTCR. Additionally, external moments might occur during the intervention and can be incorporated in the future.

8

OPTIMIZATION FOR LASER-INDUCED THERMAL THERAPY

This chapter presents the optimization of a CTCR for the specific application of laser-induced thermal therapy (LITT) in the brain. In this case, the CTCR is employed as a steerable laser probe and the robot design parameters are specifically optimized to cover and destroy a tumor volume through laser activation. Further, application-specific parameters are optimized, which are the number, location, and size of laser ablations.

This example scenario utilizes real image data and demonstrates the optimization process based on different patient datasets. It employs the presented data processing methods to extract volumetric models from medical image data.

Further, it shows the extensibility of the algorithm to optimize for application-specific parameters to solve a packing problem. The problem is formulated as multi-objective and particle swarm optimization with a variable dimension of decision vectors is applied.

Based upon:

Granna, J., Nabavi, A., & Burgner-Kahrs, J. (2017). Toward Computer-Assisted Planning for Interstitial Laser Ablation of Malignant Brain Tumors using a Tubular Continuum Robot, *MICCAI*

Granna, J., Nabavi, A., & Burgner-Kahrs, J. (2018). Computer-Assisted Planning for a Concentric-Tube Robotic System in Neurosurgery, *International Journal of Computer Assisted Radiology and Surgery*

8.1 MEDICAL MOTIVATION

Laser-induced thermotherapy (LITT) in the brain is a minimally invasive surgical procedure to denature tumor tissue through laser activation (Mensel, Weigel, and Hosten, 2006). Prior to the intervention, stereotactic frames are attached to the patient's head, and a straight laser probe is brought towards the tumor volume. Medical imaging (MR-thermometry) is utilized to localize the target and monitor the surrounding anatomical structures. As the invasiveness is low compared to conventional approaches, the relatively new method has potential benefits over others. However, the method is restricted. Irregularly shaped, and large tumors require multiple punctures to treat the overall volume. A steerable device that allows reaching the tumor on a nonlinear path could broaden the scope of this surgical procedure. A CTCR employed with a laser fiber within its inner lumen could maneuver towards the tumor volume on a nonlinear path. The robotic design and laser ablations in the brain are illustrated in Figure 43.

Other minimally invasive steerable devices have been proposed, e.g. in (Burdette et al., 2010; Swaney et al., 2012), particularly for neurosurgical applications. These include an automatic laser ablation endoscope (Su, Tang, and Liao, 2015), a thermal or laser ablation probe (Graves et al., 2012; Rezapour, Leuthardt, and Gorlewicz, 2016), MRI-guided stereotactic neurosurgery (Li et al., 2015), and robot-assisted neurological lasers (Motkoski et al., 2013). However, a system of a steerable laser probe for LITT in the brain does not exist.
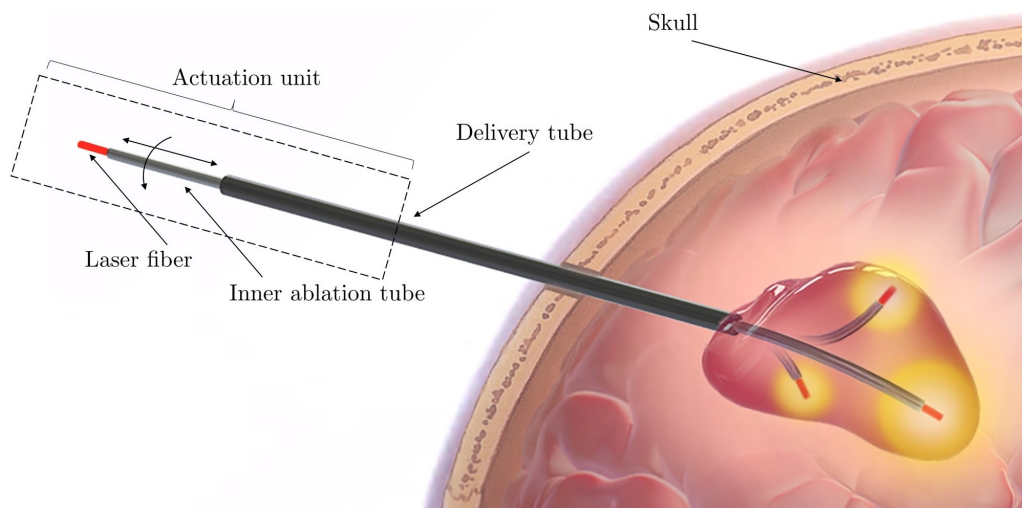

Figure 43: CTCR system composed of an outer delivery tube and an inner ablation guiding tube housing the laser fiber (red) within its inner lumen. The laser fiber deposits energy (yellow) in a spherical region (reprinted from (Granna, Nabavi, and Burgner-Kahrs, 2018), © 2018, with kind permission from Springer Nature).

8.2   ROBOTIC SYSTEM

8.2.1   *Design and Configuration Space*

For the application of LITT, the CTCR consists of two tubes. A straight tube is utilized to deliver the inner curved tube on a straight path towards the tumor volume. Within the inner lumen of the CTCR is the laser fiber to denature the tumor tissue, depicted in Figure 43. The translation and rotation of each tube enable the precise positioning of the laser fiber on a nonlinear path within the tumor volume. As the robot is supposed to be monitored during the procedure using thermometry, the tubes are considered to be made from the shape memory alloy NiTi, which has proven to be MR- and biocompatible (Comber et al., 2016).

The design and configuration space of this CTCR is as follows: the curved tube is composed of a straight section ℓ_{s_1}, and a curved section ℓ_{c_1}. The outer delivery tube is only composed of a straight section ℓ_{s_2}, as illustrated in Figure 44. The configuration space is $\mathbf{q} = [\alpha, \beta_1, \beta_2]$, where α is the rotation of the inner tube, and β_1, β_2 the translation of the two tubes respectively, see Figure 45. These are subject to the following constraints

$$\beta_1 \in [\beta_2 - (\ell_{c_1} + \ell_{s_1} - \ell_{s_2}), 0],$$
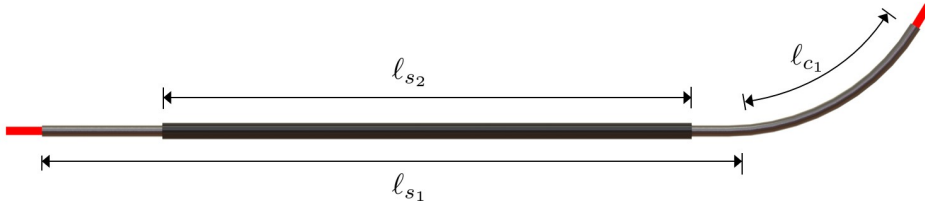$$\beta_2 \in [-\ell_{s_2}, 0].$$

Figure 44: The inner tube is composed of a straight section ℓ_{s_1}, and a curved section ℓ_{c_1}. The outer delivery tube is composed of a straight section ℓ_{s_2}.

8.2.2   *Kinematics*

The forward kinematics allows the computation of the shape of the robot for a configuration $\mathbf{q}$. In this case, a geometric model can be applied (and utilization of Cosserat rod theory is not necessary), as the robot is composed of only two tubes (one being straight), and the outer tube is much stiffer in comparison. Thus, torsion can be neglected.

The coordinate system is defined, as illustrated in Figure 45: the z-axis is pointing into the direction of the trajectory vector (which is defined by a point on the skull, towards a point within the tumor volume), and the x- and y-axis are chosen to span an orthogonal frame. The rotational $0°$ angle aligns with the negative y-axis.

The end-effector position of the CTCR is defined as $\boldsymbol{e} = [x, y, z]$. It can be computed utilizing the configuration depended lengths γ_i, see Figure 45. γ_3 here defines the length of the retracted laser fiber and depends on the selected laser probe design.
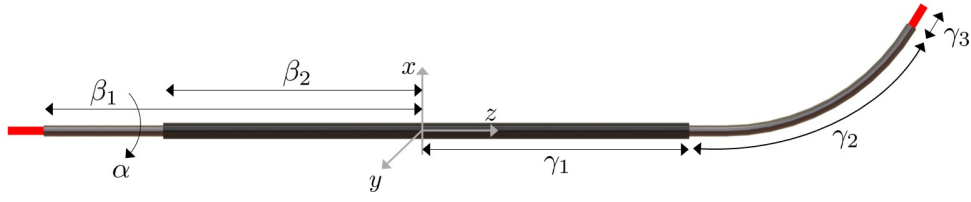
Figure 45: Configuration space and kinematic parameters of the CTCR.

$$x = \sin(\alpha) \left(\frac{1 - \cos(\kappa_1 \, \gamma_2)}{\kappa_1} + \gamma_3 \sin(\kappa_1 \, \gamma_2) \right),$$

$$y = -\cos(\alpha) \left(\frac{1 - \cos(\kappa_1 \, \gamma_2)}{\kappa_1} + \gamma_3 \sin(\kappa_1 \, \gamma_2) \right),$$

$$z = \gamma_1 + \frac{\sin(\kappa_1 \, \gamma_2)}{\kappa_1} + \gamma_3 \cos(\kappa_1 \, \gamma_2),$$

with

$$\gamma_1 = \ell_{s_2} + \beta_2,$$

$$\gamma_2 = \ell_{s_1} + \ell_{c_1} + \beta_1 - \gamma_1,$$

where κ_1 is the curvature of the inner tube. The inverse kinematics of this geometric model can be determined numerically to determine a configuration q for a given end-effector position e.

8.3   OPTIMIZATION PROBLEM

In the case of LITT, the CTCR would be utilized as a steerable laser probe to position laser ablation objects within the tumor volume. It can be assumed that the ablation objects are represented by geometrical objects (e.g. sphere, half-sphere, or ellipsoid), depending on the heat distribution of the utilized laser probe. The aim for the positioning of laser ablation objects is that they cover the overall tumor volume. This would mean that placing many overlapping ablation objects into the volume would be the ultimate goal. However, this could lead to heat accumulations in some areas, which can cause carbonization or gas formation. To prevent this, ablation objects should overlap only slightly ensuring coverage of the tumor volume, but also avoid complications of heat accumulations.

Regarding this specific application, another important aspect is to consider the insertion point on the skull surface, and the trajectory towards the tumor volume (considering surrounding anatomical structures). Also, to position the ablation objects within the tumor volume, the design of the CTCR needs to be taken into account. In summary, this is an application- and robot-specific optimization problem, of

- placing ablation objects into the tumor volume considering their overlap and coverage of the overall volume,

- and determining optimal tube parameters to place these ablation objects into the volume.

This also implies utilizing the forward kinematics model to determine the configuration parameters of each evaluated robot design.

8.3.1 *Contribution*

Optimization of application and robot dependent parameters is essential for the use of LITT, as manual placement of ablation objects cannot consider multiple objectives at the same time. The problem of placing ablation objects into a volume is related to the general problem of bin packing (Delorme, Iori, and Martello, 2015). However, general bin packing algorithms do not consider the overlap between objects. They usually only consider packing constraints, such as filling a volume with as many bins as possible, so that the applied optimization approach handles a bin packing problem with a new constraint. This packing problem is illustrated in Figure 46.
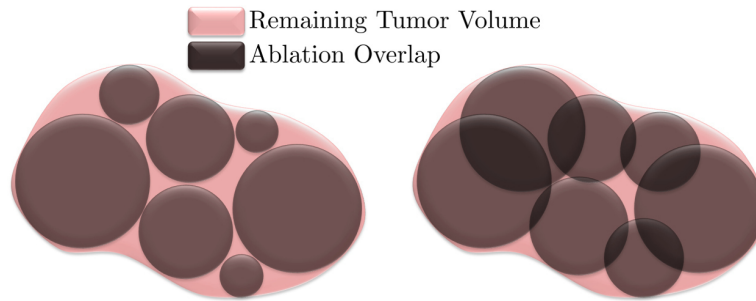

Figure 46: Regular bin packing problem (left) and packing problem for robot-assisted LITT with overlapping objects. The remaining tumor volume is depicted in light pink and the overlapping tumor volume in dark brown (right) (reprinted from (Granna, Nabavi, and Burgner-Kahrs, 2018), ©2018, with kind permission from Springer Nature).

Many researchers considered ablation planning over the past years. Most of these algorithms concentrate on radiofrequency ablation, which include multi-objective trajectory planning to treat liver (Baegert et al., 2007), or large tumors (Ren, Campos-Nanez, et al., 2014), mixed variable optimization for maximum coverage and multiple probe placements (Kapoor, Li, and Wood, 2011), optimization of electrode placement via finite-element models for a fixed access point (Chen, Miga, and Galloway, 2009), and an algorithm for optimal probe placement based on the simulation of the temperature within tissues (Altrogge et al., 2006), and under consideration of surrounding anatomical structures (Audigier et al., 2017; McCreedy et al., 2006). The authors in (Ren, Guo, et al., 2014) propose a genetic algorithm for coverage planning, and (Tani et al., 2016) consider ablation margins within the MRI planning procedure.

The existing algorithms cannot be applied as they either cannot handle multiple objectives, are specifically targeted towards radiofrequency ablation (which considers straight probes, or needles for multiple incisions into the brain), or cannot handle the application and design optimization problem at the same time.

The presented optimization framework in Chapter 5 is applied to the specific problem of robot-assisted LITT to optimize for application-, as well as robot-specific parameters at the same time. It demonstrates the extensibility of the proposed frame-

work, as the algorithm solves a bin packing problem. It utilizes medical images and different patient datasets as input to the algorithm. Further, it demonstrates the extension towards a variable dimension of decision vectors.

8.3.2 *Parameters*

The parameters of this optimization problem can be categorized into application- and robot-specific parameters. Application-specific parameters are the insertion point on the skull, the trajectory vector towards the tumor, the number of ablation objects, and their corresponding size and position. The robot-specific parameters are the number of sequentially utilized inner tubes, and their corresponding curvature and curved length. Sequential use of differently curved inner tubes potentially results in more coverage of the tumor volume. These parameters are described by

- trajectory vector $\mathbf{h}$,

- insertion point on the skull $\mathbf{o}$,

- number of ablation objects n_a,

- size of ablation object s_{a_i} with $i \in [1,...,n_a]$,

- center point of an ablation object $\mathbf{p}_i = [x_i, y_i, z_i]$,

- sequentially used inner tubes d,

- tube curvature κ_{1_j} with $j \in [1,...,d]$,

- tube curved length $\ell_{c_{1_j}}$ with $j \in [1,...,d]$.

Note, that these only include parameters, which change during the optimization procedure. However, more parameters could potentially be included to describe the overall optimization problem (e.g. the tube diameters, or straight lengths). They are assumed to remain fixed here to limit the complexity of the problem. Also, this thesis considers spherical ablation objects. Other geometrically shaped ablations can be considered, as well as their orientation.

8.3.3 *Objectives*

There exist multiple objective functions that define this optimization problem. It can be further categorized into two sub-problems, which can be explicitly described as

1) The aim of this optimization problem is to minimize the remaining tumor volume (i.e. maximize coverage) while minimizing the overlap of adjacent ablation objects. Thus, this problem is defined as multi-objective. The two objectives are conflicting, as minimization of one objective does not result in the minimization of the other. The objective functions are f_1 (minimization of tumor volume) and f_2 (minimization of ablation overlap) and can be stated as

$$\text{minimize } \mathbf{y} = f(x) = (f_1(x), f_2(x)),$$

where x defines the decision vector. The conflicting objective functions f_1 and f_2 imply that there exist no two solution vectors x and x^*, where $(f_1(x) \prec f_2(x^*))$ or $(f_2(x^*) \prec f_1(x))$.

2) The second aim is to enable the CTCR to position the ablation objects into the tumor volume. This implies that the number of ablation objects that are reachable by the robot is maximized. This number is defined as the objective function f_3 with

$$\text{maximize } y = f_3(x).$$

8.3.4 *Constraints*

The application- and robot-specific parameters impose constraints, as they have to remain within their defined parameter space. The following constraints apply

- number of ablation objects $n_a \in [n_{a_{min}}, n_{a_{max}}]$,

- size of ablations $s_a \in [s_{a_{min}}, s_{a_{max}}]$,

- sequentially used tubes $d \in [d_{min}, d_{max}]$,

- tube curvature $\kappa_1 \in [\kappa_{1_{min}}, \kappa_{1_{max}}]$,

- tube curved length $\ell_{c_1} \in [\ell_{c_{1_{min}}}, \ell_{c_{1_{max}}}]$.

The set of surface data points G_S and the voxelized grid representation G_V of the target volume need to be considered, such that all ablation center points $p_{a_i} = [x_i, y_i, z_i]$ remain within tumor volume. Medical images (MRI) define anatomical constraints for the insertion point o on the, and the trajectory vector h.

8.4 IMPLEMENTATION

The implementation of the algorithm can be accounted for by two different approaches: 1) a combined optimization approach, where the algorithm optimizes for application- and robot-specific parameters simultaneously, and 2) a separate approach, where the application- and robot-specific optimization is executed in two steps. The combined optimization approach is illustrated in Figure 47, and the separate approach in Figure 48 and Figure 49. Both approaches utilize the concept of Pareto optimality to optimize for multiple objective functions. The input to the two approaches is identical: medical images (in this case MRI) and the segmented tumor volume. The workflow of the two approaches is described as follows:

1) The combined optimization considers the definition of the insertion area on the skull after medical image processing (e.g. by the surgeon or automatically), and the trajectory towards the tumor volume can be computed as a next step (considering anatomical constraints). Then, the optimization algorithm optimizes for application- and robot-specific parameters simultaneously. The outcome of the algorithm is the Pareto optimal set considering the two objective functions f_1 and f_2. The objective function f_3 is not considered in this approach and only required for the separate optimization. The preferred solution from the front can then be selected automatically, or manually by the surgeon. Every solution describes the ablation plan (i.e.
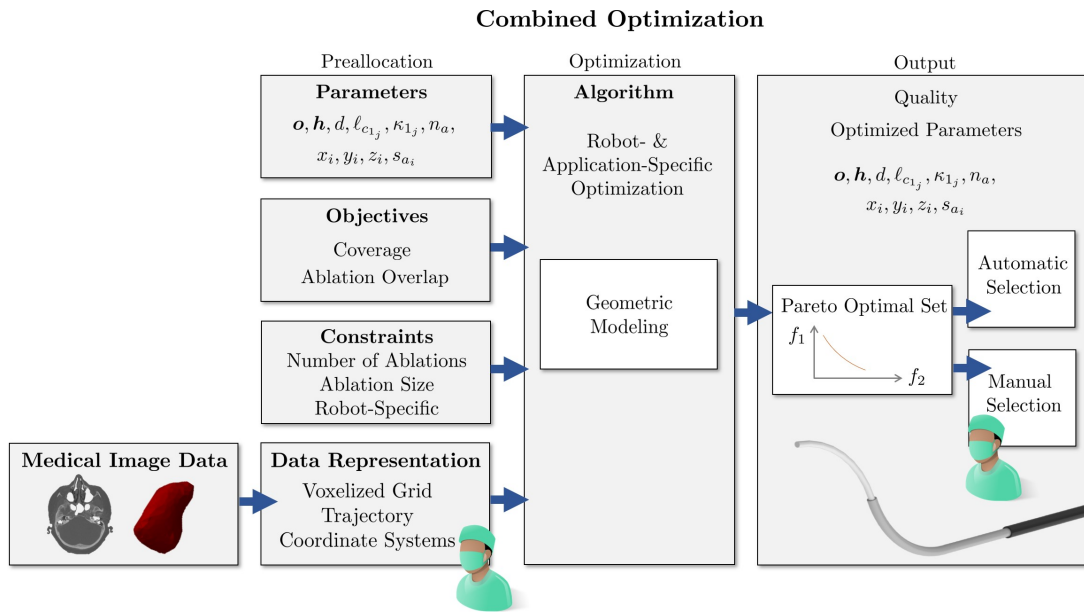
Figure 47: Combined optimization (simultaneous application- and robot-specific optimization).

number, position, size of ablation objects), and the corresponding CTCR parameters (i.e. number of sequentially used tubes, curvature, length) for execution.

2) After medical data processing, the second approach considers the determination of the application-specific parameters first and computes an optimal distribution of ablation objects. The application-specific parameter optimization also considers the two objective functions f_1 and f_2. The outcome of the algorithm is then a front of optimal solutions with respect to f_1 and f_2. Again, the preferred ablation plan can be selected automatically, or manually. Then, the surgeon could either select the insertion area on the skull manually, or it can be optimized considering anatomical structures. The trajectory to the tumor volume can be determined via the insertion point. As the last step follows the second optimization with respect to one objective f_3. The robot-specific parameter optimization computes optimal robot parameters to position the precomputed ablation objects into the tumor volume.

The combined optimization approach has the advantage that an optimized design and ablation plan is available after one execution of the algorithm, while the separate requires two steps. The separate approach simplifies the optimization problem and reduces complexity, as fewer parameters must be optimized at once. This could enable the implementation of differently shaped ablation objects, e.g. ellipsoids. The planning requires to consider their orientation, which increases the complexity of the problem.

8.4.1   *Multi-Objective Particle Swarm Optimization with Variable Dimension*

As presented in Chapter 5, the optimization approach in this thesis utilizes multi-objective particle swarm optimization. In this specific case, a variable dimension of each particle is selected. This is especially suited, as the dimension of the decision

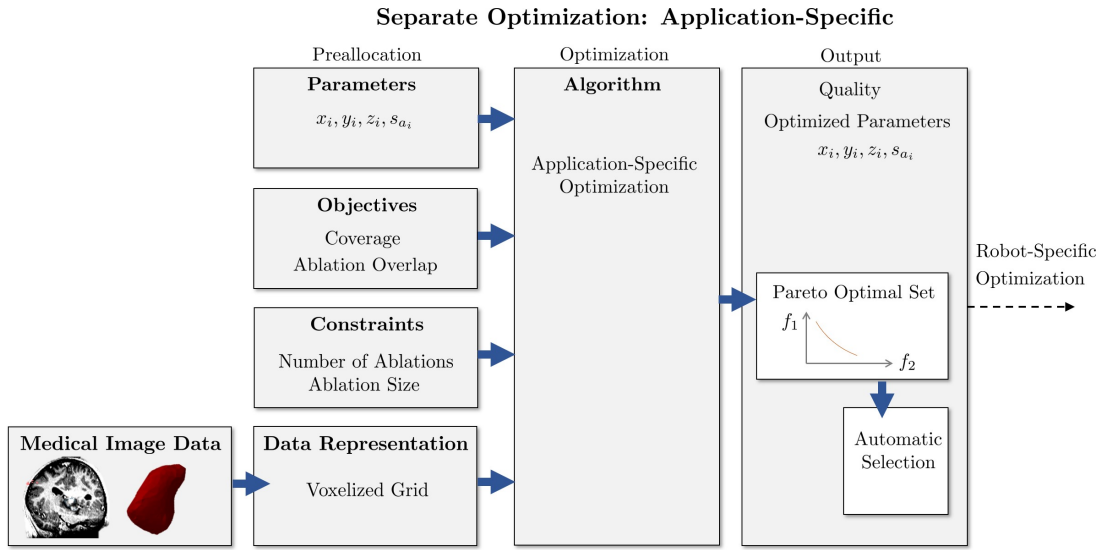**Separate Optimization: Application-Specific**

Figure 48: Separate optimization approach with application-specific optimization.

vector can be of variable length, i.e. the number of distributed ablation objects within the tumor volume, or the number of sequentially utilized tubes does not have to be fixed.

The combined optimization approach utilizes one multi-objective particle swarm algorithm. The separate approach utilizes two sequentially applied particle swarm optimization algorithms, where only the first one uses multiple objectives.

8.4.1.1 *Combined Optimization Approach*

The aim here is to optimize for application- and robot-specific parameters simultaneously. This implies that the representation of a particle differs from the separate optimization approach. A particle $\mathbf{x}_k$ is defined as $\mathbf{x}_k = [\mathbf{o}, \mathbf{h}, d, \ell_{c_{1_j}}, \kappa_{1_j}, n_a, x_i, y_i, z_i, s_{a_i}]$, where $\mathbf{o}$ is the insertion point on the skull, $\mathbf{h}$ is the trajectory vector, d is the number of sequentially utilized tubes with curved length $\ell_{c_{1_j}}$ and curvature κ_{1_j}, $j \in [1, ..., d]$. Each tube is able to position a specific number of n_a ablation objects into the tumor volume with position $\mathbf{p}_{a_i} = [x_i, y_i, z_i]$ and size s_{a_i}, $i \in [1, ..., n_a]$. This approach only requires the use of objective functions f_1 and f_2. Objective function f_3 is only required for the separate approach, as each ablation tube corresponds to a certain number of ablation objects using the above-mentioned particle representation. To determine a configuration $\mathbf{q}_i$ corresponding to the position $\mathbf{p}_{a_i} = [x_i, y_i, z_i]$ of an ablation object i, the inverse kinematics must be solved.

To enforce constraints on the parameter space, the upper and lower boundaries for $d, \ell_{c_1}, \kappa_1, n_a$, and s_a are considered. If a value exceeds this boundary, it is repositioned to the nearest value within the parameter space. The insertion point $\mathbf{o}$, and the position of ablation objects $\mathbf{p}_{a_i} = [x_i, y_i, z_i]$ are kept within the parameter space, by considering the skull surface data points, and the surface dataset G_S of the tumor volume.
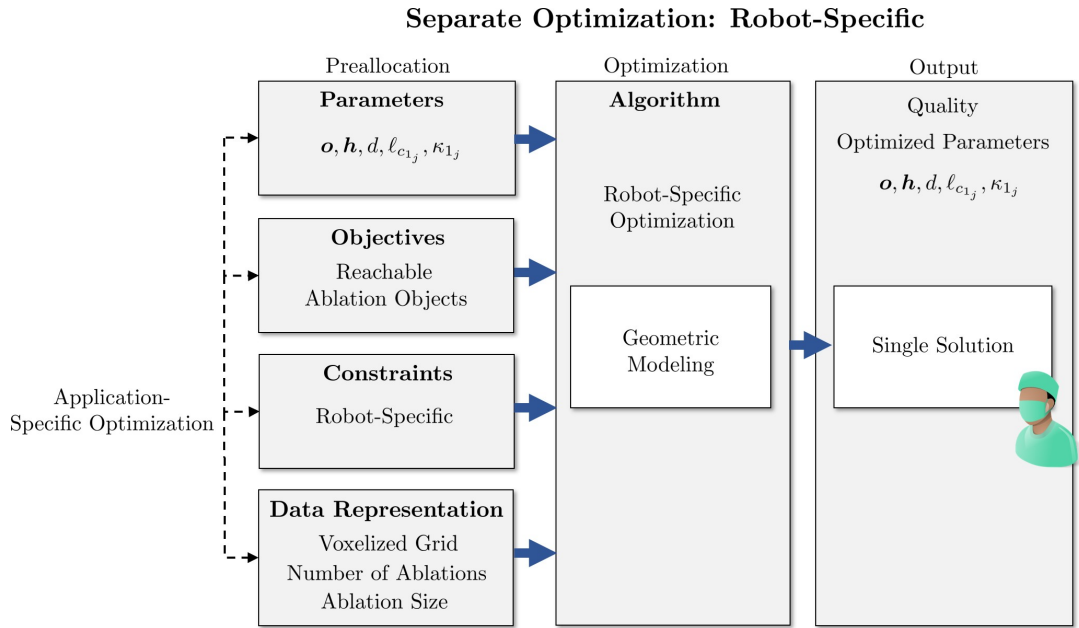
Figure 49: Separate optimization approach with robot-specific optimization.

8.4.1.2 *Separate Optimization Approach*

Application-Specific The aim of the application-specific parameter optimization is to determine an optimal number n_a of ablation objects with their position, i.e. centerpoint $\mathbf{p}_{a_i} = [x_i, y_i, z_i]$ within the tumor volume and size s_{a_i}, where $i \in [1, ..., n_a]$. The application-specific optimization utilizes the objective functions f_1 (remaining tumor volume) and f_2 (ablation overlap). A particle is defined by $\mathbf{x}_k = [x_i, y_i, z_i, s_{a_i}]$, where $\mathbf{p}_{a_i} = [x_i, y_i, z_i]$ defines the ablation object's position, and s_{a_i} defines their size, with $i \in [1, ..., n_a]$, and n_a being the number of ablation objects.

Robot-Specific To position the optimized ablation object distribution within the tumor volume using the CTCR, design-specific parameters must be determined. Thus, the particle swarm algorithm maximizes f_3, which is the number of reachable ablation objects. This implies that the number of ablation objects n_a, their position $\mathbf{p}_{a_i} = [x_i, y_i, z_i]$ and size s_{a_i} are fixed now and inputs to the robot-specific parameter optimization to determine an insertion point $\mathbf{o}$, a trajectory vector $\mathbf{h}$, the number of sequentially utilized tubes d, the curved length ℓ_{c_1} and curvature κ_1 of the inner tube. The decision vector is represented by $\mathbf{x}_k = [\mathbf{o}, \mathbf{h}, d, \ell_{c_{1_j}}, \kappa_{1_j}]$, with $j \in [1, ..., d]$.

To determine whether the center point $\mathbf{p}_{a_i} = [x_i, y_i, z_i]$ of an ablation object is reachable by the tip of the CTCR, the inverse kinematics is solved numerically. If the position is reachable, then $\mathbf{e} = \mathbf{p}_{a_i}$ and a configuration $\mathbf{q}$ is found. The CTCR within the tumor, a trajectory $\mathbf{h}$, and the corresponding ablation object are depicted in Figure 50.

8.5 EVALUATION AND RESULTS

To evaluate the proposed optimization approaches, real patient datasets are acquired through manual segmentation of MRI images using 3D slicer (slicer.org). All patient datasets are selected as representatives for irregular tumor geometries, depicted in Figure 51.

Further, a safety margin δ is defined by the surgeon to be 6 mm to ablate over the edge of the tumor to ensure maximum coverage. The voxel size v_s is set to 2 mm, as the laser probe's tip is of similar size, and the laser can thus be precisely positioned within it (see existing LITT probes, e.g. Medtronic).

8.5.1 *Combined Optimization Approach*

The combined application- and robot-specific parameter optimization is evaluated with 5 different patient datasets (tumor volumes). For each patient dataset, 3 different trajectories are generated, which result in 15 trials in total. To generate different trajectories, a surgeon places fiducials onto the skull to mark feasible insertion points (considering anatomical structures). The trajectory vector $\mathbf{h}$ is then defined by the vector pointing from an insertion point $\mathbf{o}$ to the closest direct neighbor (Euclidean distance) to the centroid of the tumor volume.

As the insertion point $\mathbf{o}$ and the trajectory vector $\mathbf{h}$ are both inputs to the optimization algorithm, they are not optimized for this evaluation. Further, the curved length ℓ_{c_1} remains fixed during the optimization to lower the computational complexity. The parameters optimized by the multi-objective particle swarm optimization algorithm with variable dimension are $\mathbf{x}_k = [d, \kappa_{1_j}, n_a, x_i, y_i, z_i, s_{a_i}]$.

The algorithm is executed using $P = 20$ particles, $T = 500$ generations, with an inertia coefficient as $\eta = 0.9$, $c_1 = c_2 = 2$ to ensure a compromise between exploration and exploitation, and r_1 and r_2 are real random numbers between 0 and 1. All parameters are selected based on performance, according to the principles mentioned in Section 5.7.2. Due to the large parameter set, computational complexity is high, such that the population size is set to a minimum of $P = 20$ particles. As mentioned in (Coello Coello and Lechuga Salazar, 2002), the number of generations should be at least 80, such that 500 generations are higher that the minimum required function evaluations. Fixed parameters are set to $\ell_{c_1} = 30$ mm and $\ell_{s_1} = \ell_{s_2} = 400$ mm, where ℓ is selected according to the mean skull dimensions considering the different patient datasets.

Each particle is initialized on a uniform random distribution regarding the following constraints of the optimization problem: $d \in [1, 2]$, $\kappa_1 \in [\frac{1}{9} \text{ mm}^{-1}, \frac{1}{15} \text{ mm}^{-1}]$, $n_a \in [4, 14]$, $s_a \in [3, 10]$ (all empirically chosen and κ selected to be within the elastic strain region of NiTi). The center point $\mathbf{p}_a = [x_i, y_i, z_i]$ of an ablation object is randomly placed into the tumor volume.

Three example Pareto fronts for patient datasets 1-3 for one trajectory into the tumor volume are illustrated in Figure 52. The solutions of the front distribute between the two objective functions f_1 and f_2. The Pareto front for patient dataset 4 for one trajectory with respect to f_1 and f_2 is depicted in Figure 53. It further illustrates three
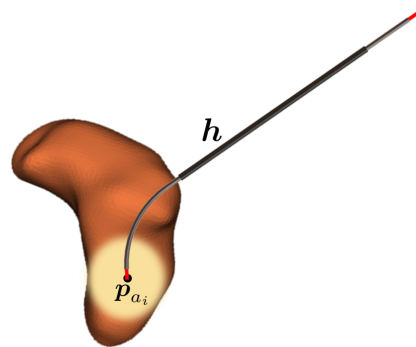
Figure 50: CTCR within the tumor volume (orange), spherical ablation object with position $\mathbf{p}_{a_i}$ (yellow), and trajectory vector $\mathbf{h}$.
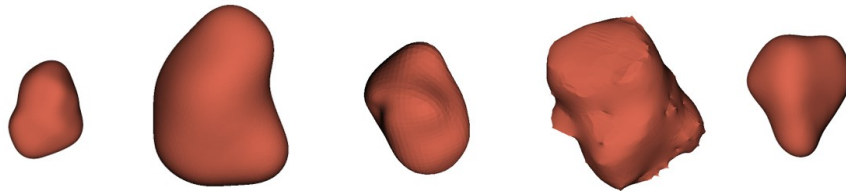

Figure 51: Five patient datasets as representatives for irregular tumor volumes.

different solutions selected from the front, which are 1) the solution with the lowest remaining tumor volume, 2) the solution with the lowest remaining tumor volume from a set of solutions with sphere overlap $< 50\%$, and 3) the solution with the least overlap between spheres from a set of solutions with remaining tumor volume $< 10\%$. All optimized spheres are of different size with a range between 3 mm and 10 mm radius. The number of sequentially used inner tubes is $d = 1$, and the inner tube's curvature is $\kappa_1 = 1/15\,\text{mm}^{-1}$ for all three solutions. The inverse kinematics is solved geometrically, as this first approach does not consider the extension of the laser fiber γ_3 that otherwise requires to solve it numerically.

The run time for the illustrated patient trial 4 was 38 h on an Intel Core i7-4790 3.60 GHz using parallelization. The mean run time for one generation is 4 min. The mean computation time over one generation for enforcing constraints is 14 s, 0.73 s for objective function evaluation, and 0.6 ms for the geometrical inverse kinematics (mean over 100 calls). The run time for enforcing constraints is relatively high, as not only the parameter space of the tubes needs to be considered but also the position of the spheres.

Figure 54 depicts two box plots for the percentage of remaining tumor volume and ablation overlap across all patient trials for solution 1-3. Across all trials, solution 1 has the lowest mean remaining tumor volume, but also the highest overlapping volume compared to the other two solutions. Solution 3 has the highest remaining tumor volume and in contrary the lowest overlapping volume, as objectives are conflicting.
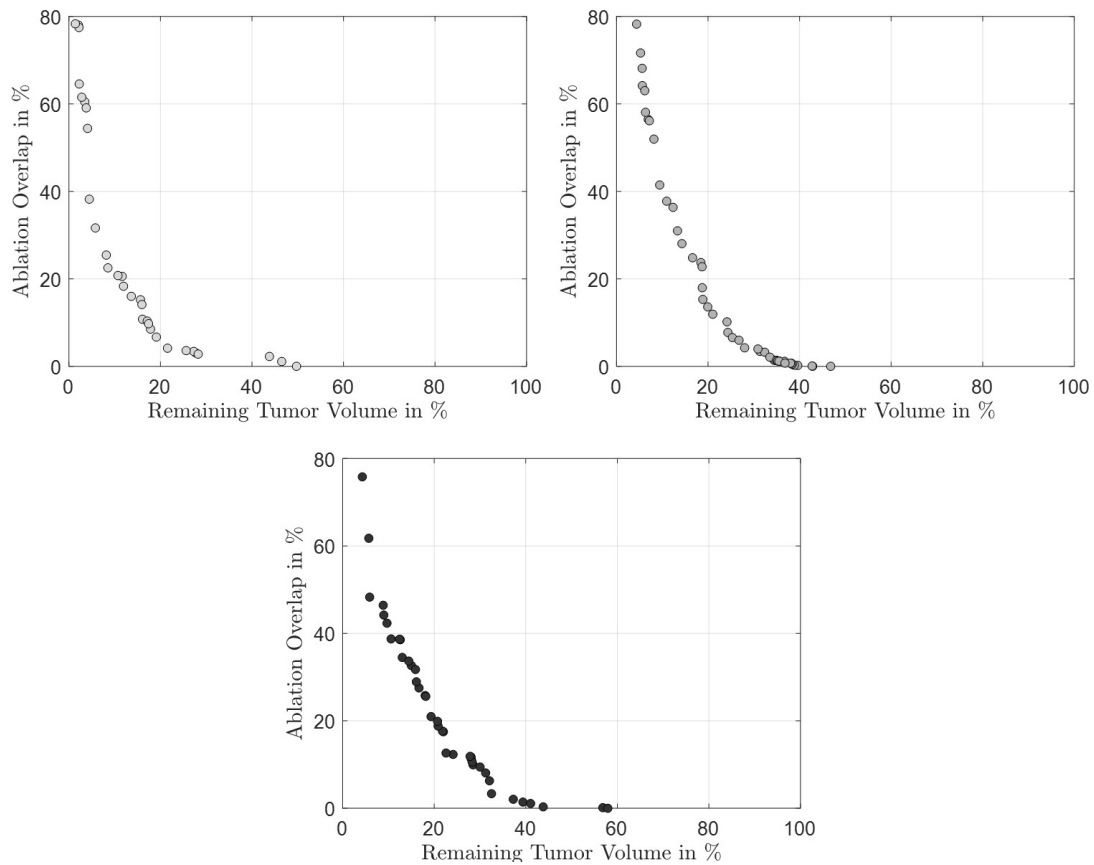
Figure 52: Example Pareto fronts for patient datasets 1-3 for one single trajectory with respect to the two objective functions ablation overlap and remaining tumor volume, both in percent.

Figure 55 illustrates three Pareto optimal sets for patient dataset 5 for three different selected trajectories. Note, that the Pareto fronts distribute similar between the two objectives functions. As the trajectories vary, the algorithm finds different solutions. However, this plot proves the effectiveness of the selected algorithm.

Figure 56 illustrates the development of the Pareto front for patient dataset 5 for a single trajectory. The Pareto optimal set is depicted after initialization, and after 50, 250, 500, and 1000 iterations. It is noticeable that the solutions improve after initialization and the Pareto front converges after 500 generations. The Pareto optimal set contains 8, 33, 25, 34, and 34 solutions after initialization, and iterations 50, 250, 500, and 1000.

An experiment is then conducted, where two neurosurgeons select their preferred solution from the front (out of the three prior selected ones) considering 10 trials (5 patient datasets and 2 different corresponding trajectories). The surgeons never select solution 1, solution 2 is selected 8 times, and solution 3 is selected 22 times. They argue that approximately 10% remaining tumor volume is acceptable, as chemotherapy after LITT treatment outweighs the risk of heat accumulation.

RTV 3.5%   RTV 3.7%   RTV 9.9%
Overlap 58.1%   Overlap 43.6%   Overlap 15.6%
9 Spheres   9 Spheres   7 Spheres
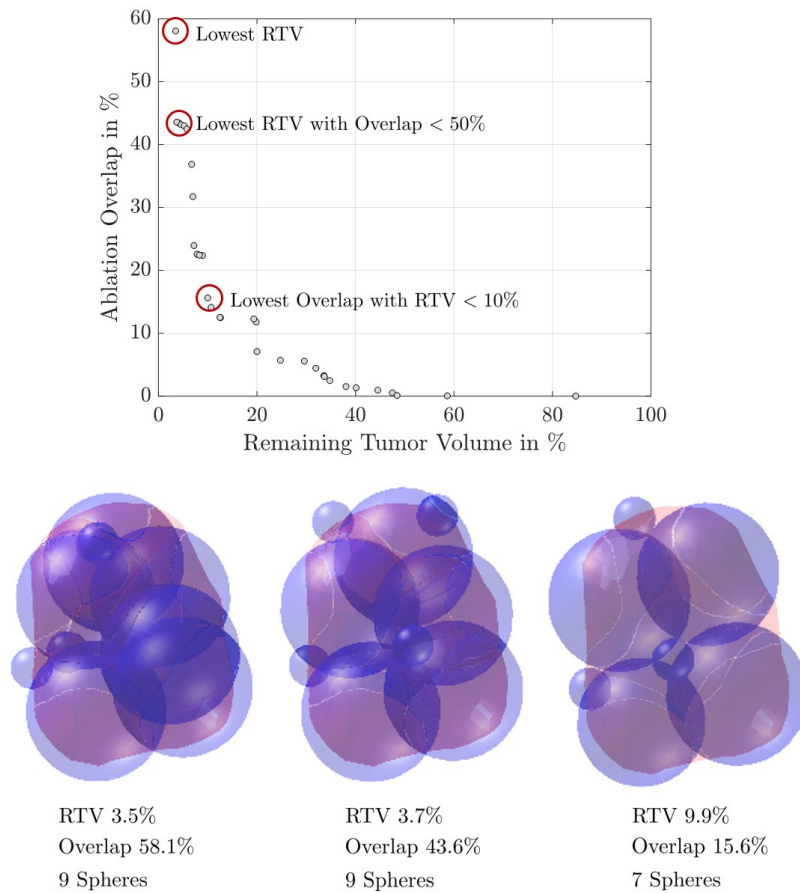
Figure 53: Pareto front for patient dataset 4 for one trajectory with respect to the two objective functions ablation overlap and remaining tumor volume, both in percent. The selected solutions from the front are marked by red circles (top) and the sphere distribution is illustrated (bottom).
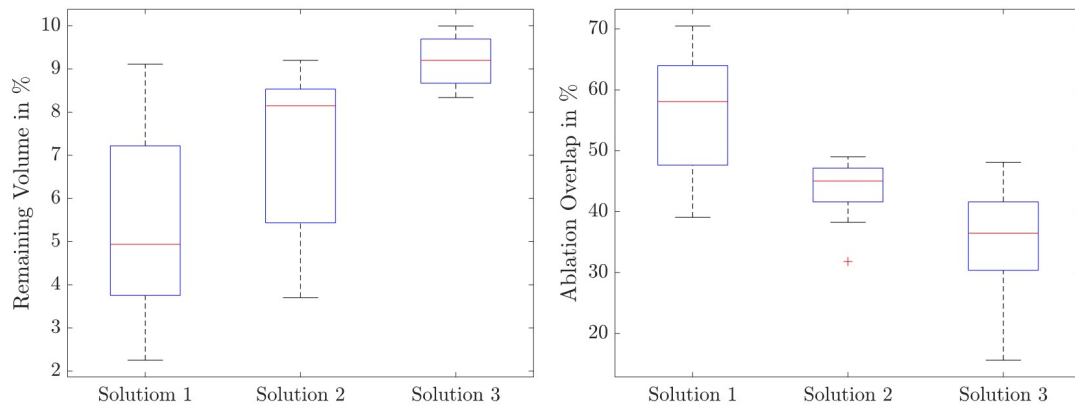
Figure 54: Box plots for the percentage of remaining tumor volume and ablation overlap for solutions 1, 2, and 3 across all patient trials. The red line indicates the median, the box upper and lower quartiles, the whiskers indicate the minimum and maximum values, and outliers are depicted in red.
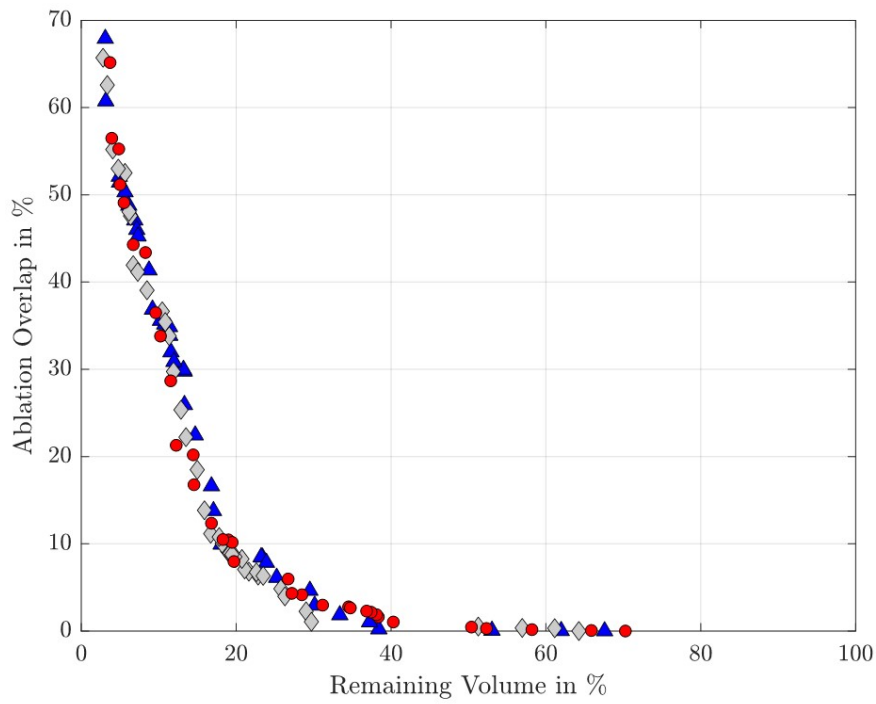
Figure 55: Pareto fronts for patient dataset 5 for three different trajectories.
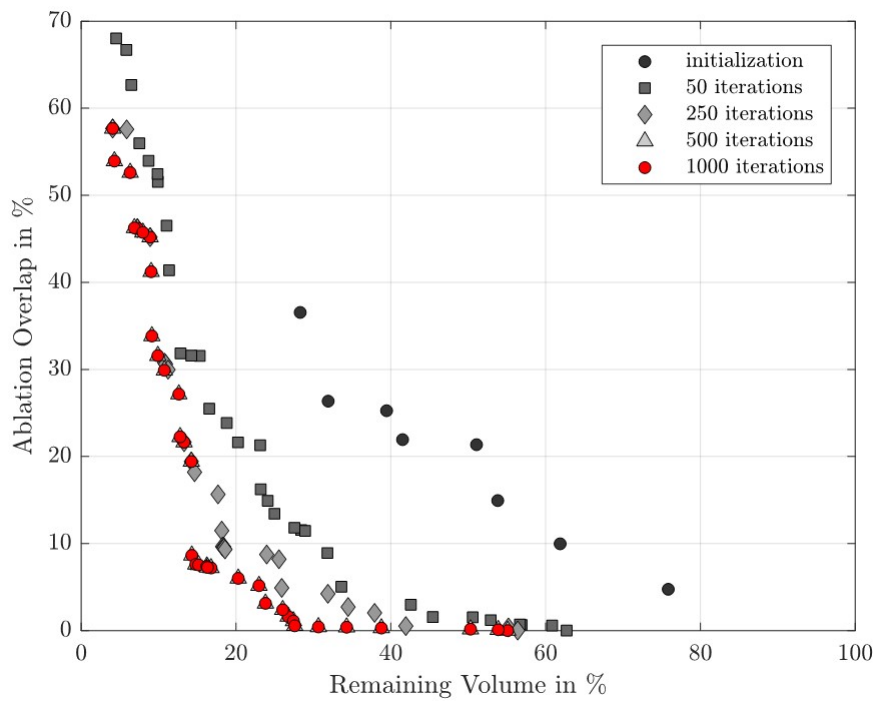
Figure 56: Distribution of the Pareto front for patient dataset 5 for a single trajectory. The Pareto optimal set is depicted after initialization, and after 50, 250, 500, and 1000 iterations.

8.5.1.1 *Discussion*

The expertise of two neurosurgeons proves reasonable results of the algorithm, considering that a remaining tumor volume of 10 % is acceptable and can be treated with chemotherapy. Solution 3, with a compromise between ablation overlap and coverage, is selected most of the time so that an automatic solution selection from the Pareto front can be performed for future simulations.

The manual ablation distribution inspection by the two neurosurgeons indicates that the maximum number of ablation objects can be lowered. This would constrain the optimization problem to generate fewer solutions with high overlap. Further, the results indicate that sequential use of tubes is not necessary, as multiple solutions with a single curved tube exist with reasonable coverage and low overlap.

Additionally, the convergence behavior of the Pareto optimal set indicates that future evaluations should use more function evaluations for an improved outcome but are limited here due to computational power.

8.5.2 *Separate Optimization Approach*

As the previous method optimizes for a specifically defined number of trajectories (which are generated by the help of a neurosurgeon), this evaluation takes a different approach. The aim is to evaluate the effectiveness of the algorithm and to determine, whether multiple trajectories from various directions into the tumor volume can be taken to execute the optimized ablation plan. The separate optimization approach is evaluated considering three patient datasets (patients 3-5) and 50 randomly generated trajectories. This subset is selected to be smaller, as the consideration of additional trajectories is the focus of this evaluation.

8.5.2.1 *Application-Specific*

The particle swarm algorithm with variable dimension is executed with the two objective functions f_1 and f_2 using $P = 50$ particles, $T = 1000$ generations, inertia coefficient $\eta = 0.9$, and $c_1 = c_2 = 2$. All parameters are selected based on performance and convergence behavior. Further, application-specific optimization requires less computation time, such that population size and function evaluations can be increased. The position of a particle is initialized based on the following constraints of the parameters: the number of ablation objects to $n_a \in [3, 10]$ and their size to $s_a \in [3\,\text{mm}, 10\,\text{mm}]$. The initial center point $\mathbf{p}_{a_i} = [x_i, y_i, z_i]$ of an ablation object is randomly placed within the tumor volume. These intervals are defined by the surgeon. The number of ablation objects is set to a lower value, as previous results show that neurosurgeons generally prefer fewer ablation objects.

The Pareto optimal solutions represent the outcome of the application-specific parameter optimization using the multi-objective particle swarm algorithm with variable dimension. These are depicted in Figure 57 for patients 3-5. The solutions distribute from the objective function f_1 (remaining tumor volume) to f_2 (overlapping volume), where all solutions are depicted in percent. Figure 58 illustrates one solution from the front for patient 3, 4 and 5 from different view angles. The solutions
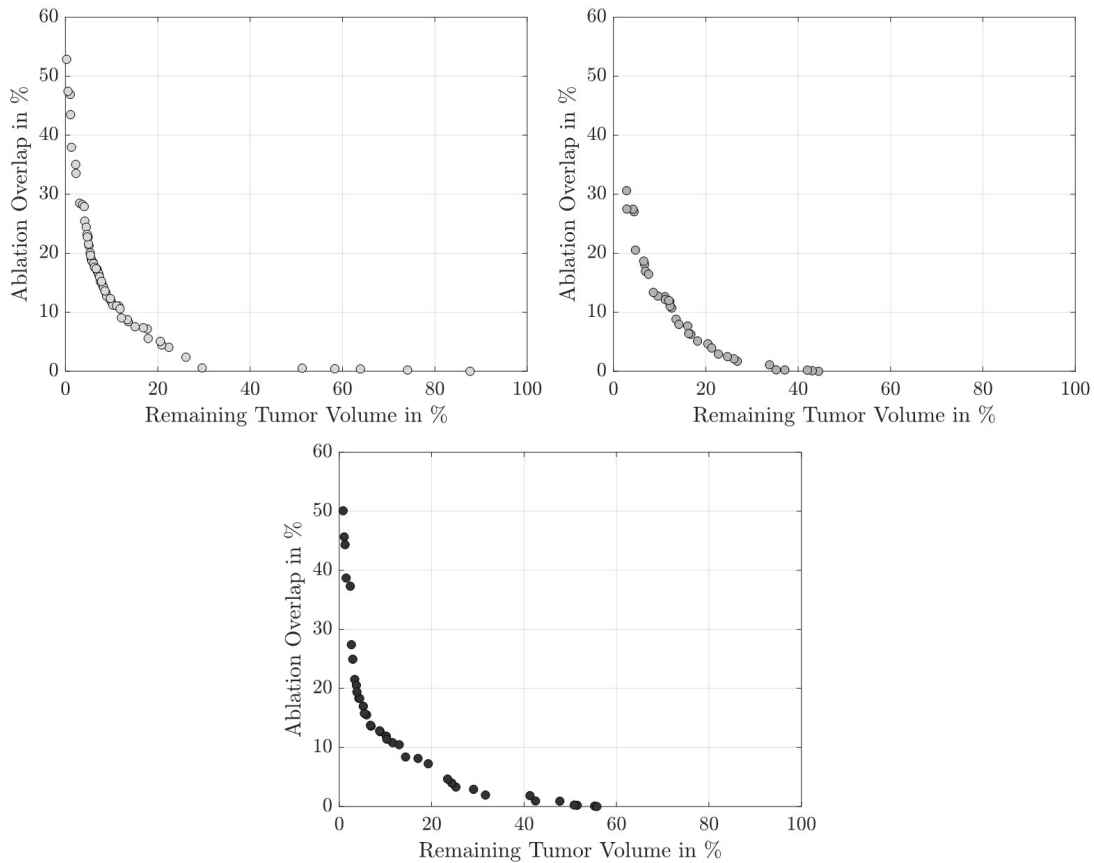
Figure 57: Pareto front with optimal solutions with remaining and overlapping tumor volume for patients 3, 4 and 5.

from the front are selected based on the previous results with approximately 10% remaining tumor volume. Solution 1 exhibits 7 spherical ablation objects, solution 2 has 5, and solution 3 is defined by 8 spherical ablation objects. All spheres are of different size with a range between 3 mm and 10 mm radius.

The mean run time on an Intel Core i7-4790 3.60 GHz was 169 min across all patient trials using parallelization. The following computation times are determined for patient 4. The mean run time for one generation is 28.23 s and 10.16 s in parallel. The mean computation time over one generation for enforcing constraints is 0.21 s and 0.22 s for objective function evaluation.

Figure 59 illustrates the development of the Pareto front for patient dataset 4 after initialization, and 50, 250, 500, and 1000 iterations. The archive size is 7, 31, 35, and 52 respectively and shows a large increase from 500 to 1000 iterations.

To prove the performance of the algorithm, the optimization is repeated for patient dataset 4. The Pareto fronts for all three optimizations are depicted in Figure 60. Results show that the algorithm results in the same Pareto fronts in two out of three cases. For the third optimization run, results are similar for low ablation overlap and low remaining tumor volume but spread further apart for extreme function values. This indicates that the selection of higher population size or an increase of the inertia weight could be appropriate to ensure sufficient exploration of the search

Patient 3
RTV 9.61 %
Overlap 11.83 %

Patient 4
RTV 9.63 %
Overlap 12.74 %

Patient 5
RTV 8.73 %
Overlap 12.82 %
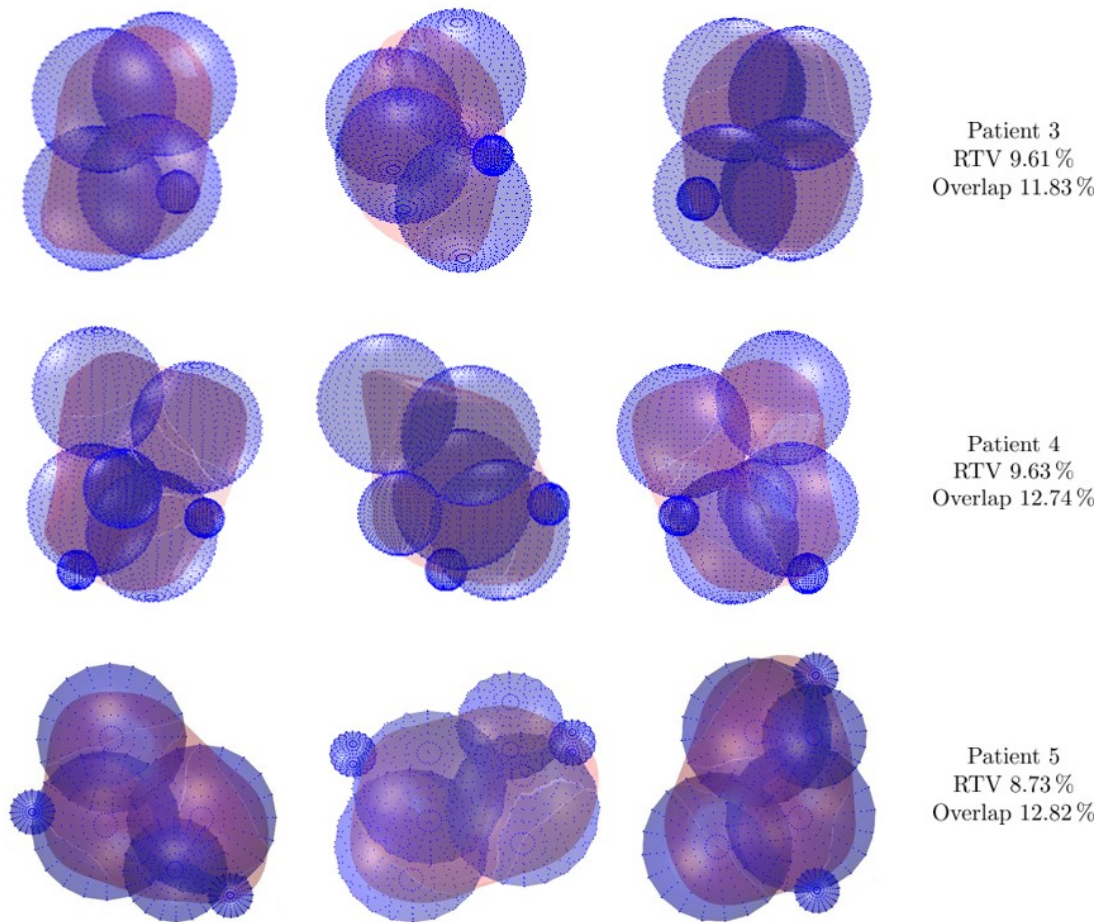
Figure 58: The selected solution (to have 10 % remaining tumor volume but less overlap) from the front from different view angles for patient 3, 4, and 5.

space. However, as the selected solution from the front represents a compromise between ablation overlap and remaining tumor volume, extreme function solutions are not a necessity and the algorithm can be executed with the selected parameters for this evaluation.

The performance of the algorithm is then tested using a larger population. Figure 61 illustrates the Pareto fronts for P = 50 particles for the three optimization runs for T = 1000 in gray and the Pareto front in yellow with P = 80 particles. Results show that performance can be improved with a larger population. Figure 62 illustrates the Pareto fronts for P = 50 particles for the three previous optimization runs for T = 1000 in gray and the Pareto front in yellow with P = 80 particles for T = 500. It is noticeable that the optimization with increased population size and T = 500 outperforms the optimization with fewer particles and T = 1000. This demonstrates the effectiveness of an increase in population size.
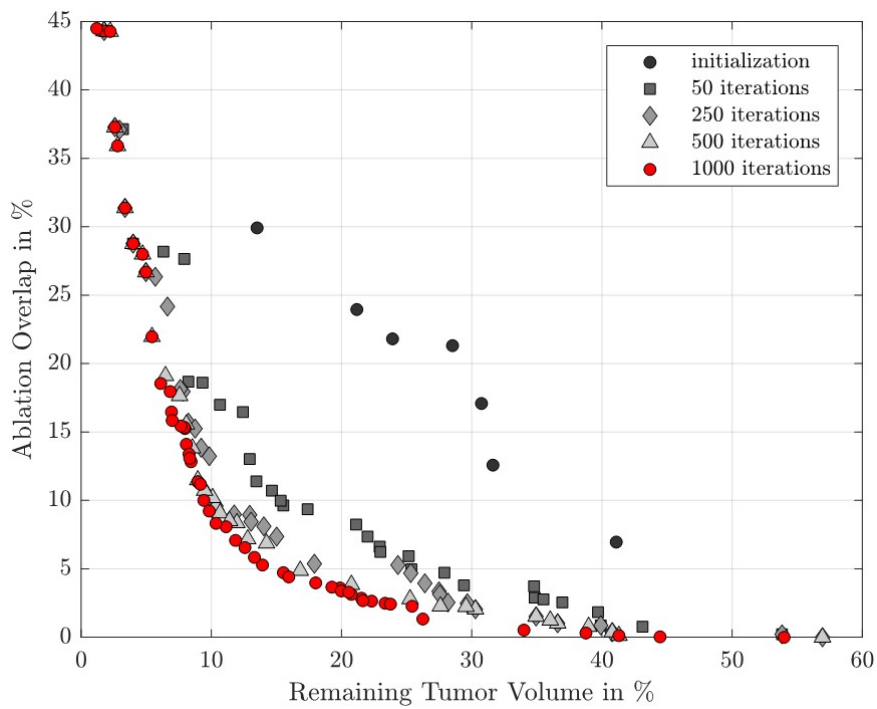
Figure 59: The development of the Pareto front for patient 4 after initialization, and 50, 250, 500, and 1000 iterations.
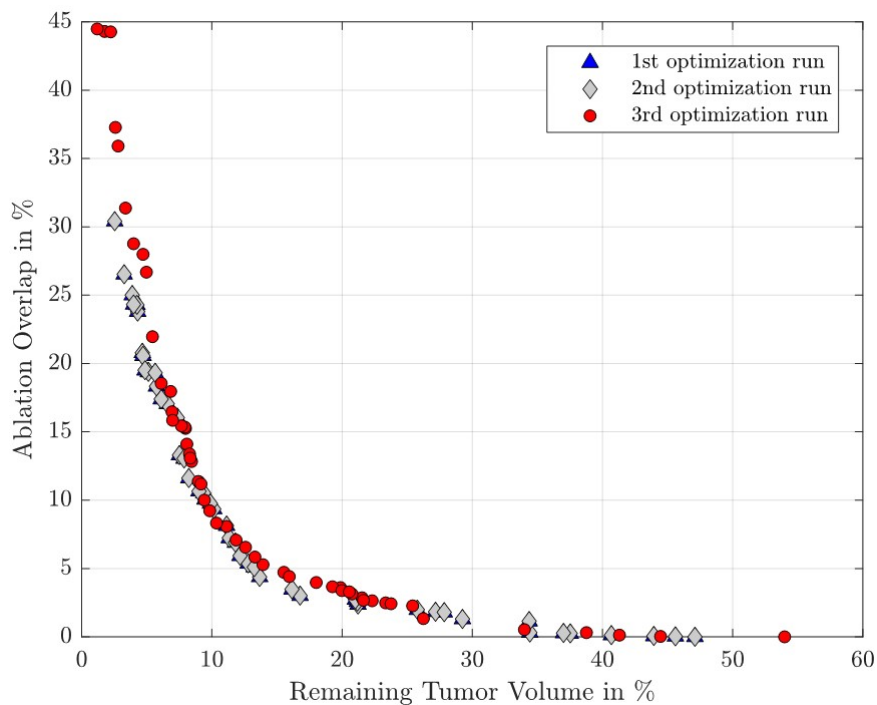
Figure 60: Pareto fronts for three optimization runs with respect to ablation overlap and remaining tumor volume for patient 4 and $T = 1000$.
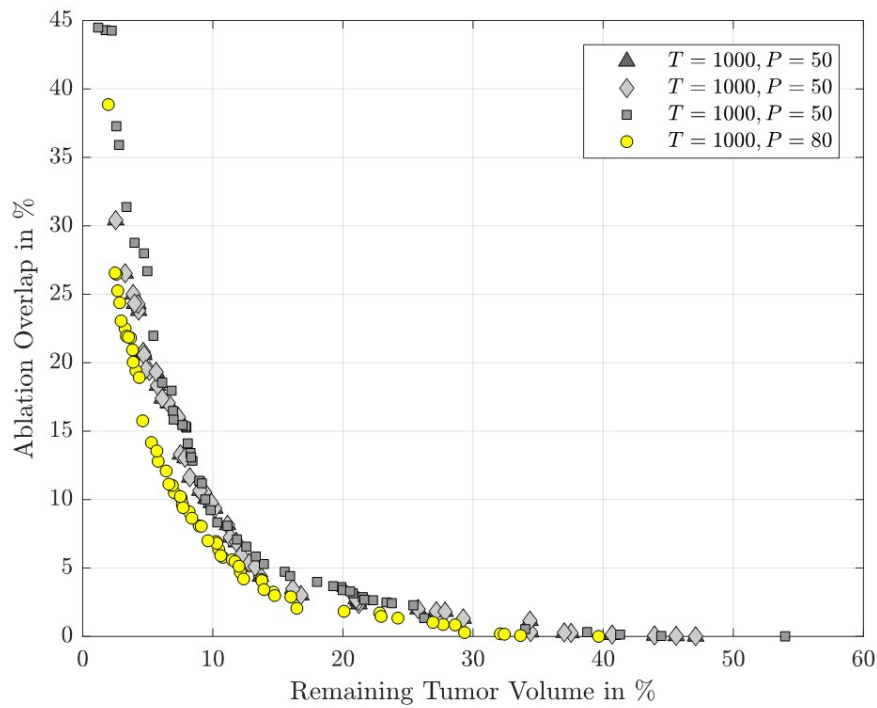
Figure 61: Pareto fronts for four optimization runs with respect to ablation overlap and remaining tumor volume for patient 4 and T = 1000. The Pareto optimal set for P = 50 particles (different shades of gray) and for P = 80 (yellow).
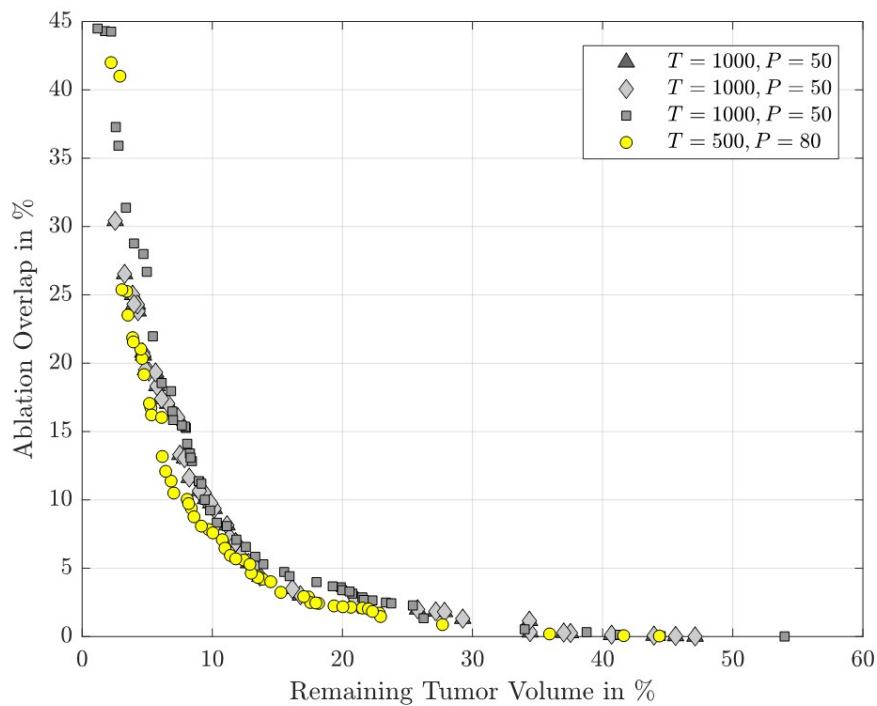
Figure 62: Pareto fronts for four optimization runs with respect to ablation overlap and remaining tumor volume for patient 4. The Pareto optimal set for P = 50 particles and T = 1000 (different shades of gray) and for P = 80 and T = 500 (yellow).

8.5.2.2 *Robot-Specific*

The particle swarm algorithm with one objective f_3 is then executed optimizing for ℓ_{c_1} and κ_1. d is set to 1, as previous results show that one sequentially utilized tube is sufficient to cover the overall tumor volume. The fixed lengths are again set to $\ell_{s_1} = \ell_{s_2} = 400\,\mathrm{mm}$, according to the mean skull dimensions. Each particle is defined by a certain insertion point on the skull $\mathbf{o}_k$ and trajectory vector $\mathbf{h}_k$. This leaves 50 different trajectories, as the algorithm is executed with 50 particles. All trajectories are initialized by selecting points from the set of tumor surface points randomly.

The following variables are again initialized based on performance: $P = 50$ particles, $T = 100$ generations, inertia coefficient $\eta = 0.9$ and $c_1 = c_2 = 2$. The number of function evaluations is reduced, as the complexity of the robot-specific optimization is lower compared to the previous optimization problems. The inner tube's diameter is set to 2 mm based on existing commercial laser probes. A particle is initialized on a uniform random distribution regarding: $\ell_{c_1} \in [10\,\mathrm{mm}, 15\,\mathrm{mm}]$ and $\kappa_1 \in [1/13\,\mathrm{mm}^{-1}, 1/20\,\mathrm{mm}^{-1}]$ (κ selected to be within the elastic strain region of NiTi.

Results show that it is possible to treat the tumor volume using various trajectories: out of $k = 50$ generated trajectories, 43 can be utilized to distribute the spherical ablation objects into the tumor volume of patient 3, 38 for patient 4, and 37 for patient 5. This implies that a successful CTCR design is found with an optimized length ℓ_{c_1} and curvature κ_1. The trajectories for patient 1 are depicted in Figure 63 from different view angles. It is noticeable that various directions into the tumor volume can be taken.

As a representative example case, a neurosurgeon selected an anatomically feasible trajectory (regarding anatomical constraints and surrounding structures) from the overall set of trajectories for patient 4. The corresponding insertion point on the skull and the tumor volume are illustrated within the MR-images for a representative 2D and 3D view in Figure 64. To visualize representative configurations of the CTCR, Figure 65 illustrates example configurations to position the spherical ablation objects within patient 4 considering one selected trajectory.
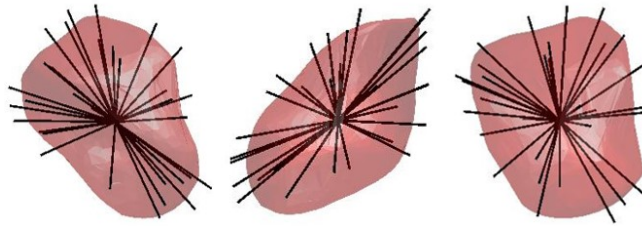
Figure 63: Optimized trajectories into the tumor volume for patient 4 from different view angles (reprinted from (Granna, Nabavi, and Burgner-Kahrs, 2018), © 2018, with kind permission from Springer Nature).

In this case, the extension of the laser fiber γ_3 is considered, such that the inverse kinematics had to be solved numerically using *fmincon* in MATLAB (i.e. numerical determination of the configuration $\mathbf{q}$ for a corresponding end-effector position $\mathbf{e}$). The mean run time across all three patient trials on an Intel Core i7-4790 3.60 GHz
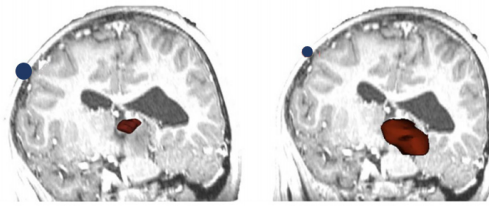
Figure 64: A manually selected insertion point with corresponding trajectory by the surgeon from the overall set. MRT slice and 3D view (left and right) (reprinted from (Granna, Nabavi, and Burgner-Kahrs, 2018), ©2018, with kind permission from Springer Nature).
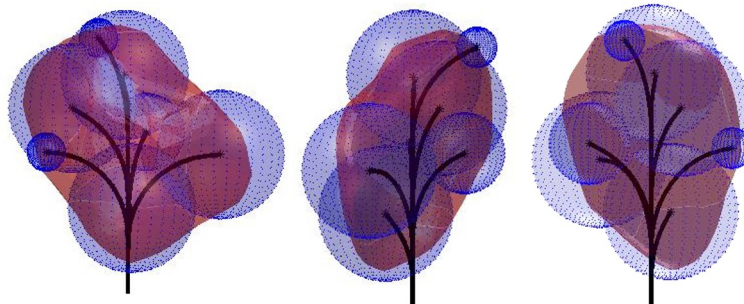
Figure 65: Different view angles of the optimized configurations of the CTCR for one example trajectory to reach all 7 sphere center points of patient 4 (reprinted from (Granna, Nabavi, and Burgner-Kahrs, 2018), ©2018, with kind permission from Springer Nature).

was 69 min. The mean run time on an Intel Core i7-4790 3.60 GHz was 169 min across all patient trials using parallelization. The following computation times are determined for patient 4. The mean run time for one generation is 59 s. The mean computation time over one generation for enforcing constraints is 0.08 ms, 1.29 s for objective function evaluation, and 57 ms for the numerical inverse kinematics (mean over 100 calls). Figure 66 depicts a box plot for the optimized curved lengths ℓ_{c_1} and curvature κ_1 across all trails, where the red line indicates the median values, the box upper and lower quartiles, the whiskers indicate the minimum and maximum values, and outliers are depicted in red.

The curved length ℓ_{c_1} is optimized with values between 10.3 mm and 13.8 mm, and the curvature κ_1 between 0.05 mm^{-1} and 0.077 mm^{-1} across all patients. Note, that the upper limit of $\ell_{c_1} = 13.8$ mm can be selected for future designs, assuming that the straight tube is much stiffer than the inner tube. This would imply that the curved part of the inner tube is retracted into the outer tube to remain straight. Further, the upper curvature limit of 0.077 mm^{-1} is selected by the algorithm in some cases. This characterizes the curvature where the maximum strain limit is reached for NiTi. Theoretically, if a different material with a higher strain limit would be selected, or tube patterning would be performed, more trajectories could be feasible.

8.5.2.3 *Discussion*

Results demonstrate that the separate optimization approach achieves reasonable solutions and less than <10% remaining tumor volume and sufficient coverage can be achieved. Automatic solution selection can be performed in the future, which might be a preferred option if time is limited before the intervention.

The Pareto fronts for some of the results indicated that solutions are sparse towards extreme function values. An increase of solutions close to extreme function values can be achieved by an increased exploration of the search space. This can be obtained by an increase of the inertia weight, more confidence of the personal best influence, or a larger population. However, solutions close to extreme function values are not always necessary. In the case of LITT, the preferred solution represents a compromise between both cost functions. Further, the convergence for the separate optimization approach and application-specific optimization can be improved by an increase in population size.

Various trajectories into the tumor volume can be taken to distribute the optimized ablation plan. Here, 50 trajectories have been tested for feasibility. Testing more trajectories would possibly result in even more feasible ones. As there exist multiple paths into the tumor volume, the surgeon could select the preferred trajectory vector in the future, or a planning tool can easily navigate around anatomical structures that have to be avoided.

Note, that the robot-specific optimization problem for the separate approach does not necessarily require the use of particle swarm optimization due to the low complexity of the problem. For generality, particle swarm optimization has been applied to both.

8.6 CONCLUSION AND FUTURE WORK

A multi-objective particle swarm optimization algorithm with variable dimension is applied to the design- and application-specific parameter optimization of CTCR. This is the first robotic application, where particle swarm optimization with variable dimension is utilized. Further, this chapter presents two optimization approaches (combined and separate application- and robot-specific optimization) to optimize the optimization parameters specific to LITT. The algorithm proves its effectiveness, as multiple solutions distribute on the Pareto front between the two objective functions and several optimizations for a single patient dataset result in a similar distribution. However, convergence behavior and an increase of the Pareto optimal set could potentially be achieved through larger population sizes or adaption of the inertia weight and global confidence within the swarm. Further, neurosurgeons investigated the planning distribution of spherical ablation objects within the tumor volume and multiple trajectories are feasible for task performance. This proves the feasibility of the concept for steerable LITT using a CTCR.

Other parameters can be included in the future to describe the optimization problem. From a clinical point of view, the optimization parameters could account e.g. for a specific set of ablation tubes (that are readily available within the OR), different ablation geometries (half-spheres, ellipsoids), effects from laser-tissue interaction, the
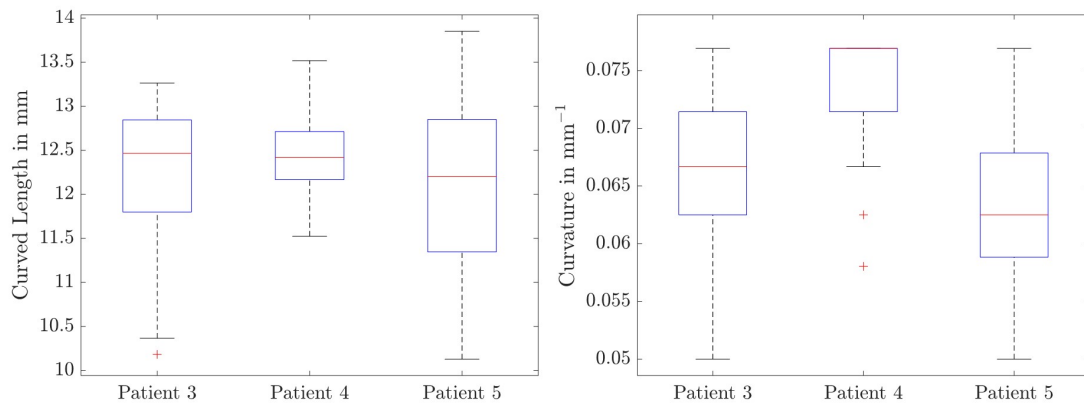
Figure 66: Optimized curved length ℓ_{c_1} and curvature κ_1 across all patients and trajectories. The red line indicates the median, the box upper and lower quartiles, the whiskers indicate the minimum and maximum values, and outliers are depicted in red (reprinted from (Granna, Nabavi, and Burgner-Kahrs, 2018), © 2018, with kind permission from Springer Nature).

non-homogeneous convection of ablative energy (due to heat sinks, or convection barriers through carbonization in multiple overlapping areas), or surrounding critical structures.

This application demonstrates that the proposed optimization method is capable to handle different parameters, objectives, and constraints, which can be adapted using the presented approach in Chapter 5. If further demonstrates the extensibility of the algorithm towards the optimization of application-specific parameters and bin packing.

Part IV

CONCLUSION

CONCLUSION

9

9.1 CONTRIBUTION

In summary, this thesis presents a methodology for the parameter optimization and structural synthesis of CTCR. The main contributions, considering the research questions of this doctoral thesis, are

1) Classification and Formulation of the Structural Design Optimization Problem of CTCR that can handle different problems and patients.

This work formulates the structural design optimization for CTCR and classifies the parameter space, objectives, and constraints that apply to example applications in minimally invasive surgery. Further, an optimization methodology and workflow to handle different patient datasets is presented. The applicability to different patient datasets is shown in the context of LITT.

This thesis proposes a multi-objective particle swarm optimization algorithm with variable dimension for the structural design optimization of CTCR. This work hypothesizes that the proposed algorithm has the potential to cope with the structural design optimization of CTCR. It has been successfully applied to three different scenarios and has proven its performance compared to a single-objective Nelder-Mead algorithm for the design optimization of two cooperative robotic arms. Further, it has been extended towards application-specific parameter optimization in the context of LITT (the bin packing of unequal spheres) and applied to a multidimensional structural design optimization problem for medical task performance. The extensibility to a variable dimension of decision vectors is a feature of the algorithm to handle problems where the dimension of the parameter optimization space is not known a priori.

2) Consideration of the Multidimensional Parameter Space that includes the length, diameter, wall thickness, curvature, and elasticity of the tubes. The general optimization methodology is formulated to account for various design parameters and does not limit its number. Further, the decision vector of the optimization problem can be of variable dimension approaching infinite options.

The CTCR design-specific parameters include the geometrical design (straight and curved section length, diameter, wall thickness, and curvature), as well as material parameters that consider the elastic modulus, the recoverable strain rate, the Poisson's ratio, and the shear modulus. The state of the art does not yet consider material parameters and tube diameters. Additionally, application-specific parameters can also be handled by the algorithm, as the application of laser-induced thermal therapy has shown, where design- as well as application-specific parameters are considered for optimization.

The inclusion of external forces into the optimization procedure and consideration of stiffness and material properties are targeted for the first time. It is a necessity to

bring CTCR closer to the real application.

3) Consideration of Heterogeneous and Conflicting objects.

This work defines homogeneous, heterogeneous, non-conflicting, and conflicting objectives and formulates key objective functions. The concept of Pareto optimality is applied that considers the dominance of some solutions over others to achieve a Pareto optimal front of solutions and a Pareto optimal set. This is an addition to the state of the art that mostly utilize scalar error metrics for optimization, non-conflicting objectives, and the application of weighting methods. Further, the combination of different objectives is described in the concept of parameter optimization for CTCR. Considering the applications in this thesis, two conflicting objectives are selected for the structural stiffness design optimization and laser-induced thermal therapy in the brain.

In summary, this thesis presents a parameter optimization methodology for the structural design optimization of CTCR with the application of a multi-objective particle swarm optimization algorithm with variable dimension.

9.2   FUTURE WORK

9.2.1   *Investigation of further CTCR-specific Characteristics*

To bring CTCR closer to real applications, further parameters require attention and need to be investigated in the future. This includes the consideration of kinematic measures into the design optimization procedure. These are singularities and manipulability, as well as other kinematic and dynamic performance measures that are considered as objectives in other robotic applications. As they are tied to motion planning strategies, they are not considered in the scope of this work but can be incorporated in the future (Baykal, Bowen, and Alterovitz, 2018; Baykal, Torres, and Alterovitz, 2015; Bergeles and P. E. Dupont, 2013; Fellmann and Burgner-Kahrs, 2015; Kuntz, Torres, et al., 2015; Leibrandt, Bergeles, and Yang, 2017; Torres and Alterovitz, 2011).

Further, the incorporation of stability measures could enable an advanced and safer performance of the CTCR during deployment (Gilbert, Rucker, and Webster III, 2016; Ha, Park, and Dupont, 2016; Hendrick, Gilbert, and Webster III, 2015b; Webster III, Okamura, and Cowan, 2006; R. Xu, Atashzar, and Patel, 2014). However, the inclusion of stability measures is not a necessity, as the control of CTCR could prevent snapping behavior.

The stiffness and elasticity behavior of CTCR based on patterning of the tubes is neglected in this thesis (J. S. Kim et al., 2014; D. Y. Lee et al., 2015). Specific patterns have the potential to increase stability and stiffness while remaining inherent flexibility. These characteristics can be included in the parameter optimization in the future to advance force or moment absorption. Further, this work investigates tubes with straight and curved sections. The utilization of helically shaped tubes can be ben-

eficial in some medical procedures (e.g. cochlear implant surgery, hippocampus in the brain), where the trajectory can be approximated by a helix. These tubes further allow for follow-the-leader behavior, which enables safe navigation through tight lumen (Gilbert, Neimat, and Webster III, 2015). Further, the optimization of non-constant curvature tubes can have potential benefits, as they have improved stability behavior. Thus, the sudden release of friction between the tubes can be reduced, which allows for safer navigation.

9.2.2 *Algorithm Improvement*

The computational efficiency of the algorithm requires improvement to enable real-time optimization of application-specific parameters during intervention or if time is limited before surgery and an optimal CTCR design set is instantly required. The optimization for specific sets of tubes that are ready for use in the hospital can also be incorporated in the future. The computational efficiency can be improved if performance criteria within the particle swarm optimization are optimally selected, as they influence the exploration and convergence of the algorithm. This requires extensive statistical analysis of the minimum number of generations, population size, inertia weight, and the influence of the personal versus global confidence within the swarm. The analysis would have to be performed based on multiple CTCR applications to determine if there exist rules on how to optimally select these performance criteria based on the number of parameters or objectives. Learning-based approaches utilizing large sets of medical data (different patient dataset) and statistical measures can further advance the parameter optimization of CTCR. Also, there exist different options to enforce the constraints of the parameter space. These include random repositioning of the particle, truncation at the boundary or reflection at the boundary. This implementation can affect the performance behavior of the algorithm and requires investigation in the future.

As sensing-based knowledge of the robot's pose is currently of research interest (B. Kim et al., 2014; Ryu and Dupont, 2014; Vandini et al., 2015; R. Xu, Yurkewich, and Patel, 2016), future optimization methods could include sensor data into the optimization to compute application-specific parameters during the intervention. Further, the incorporation of advanced motion planning strategies for obstacle avoidance would be beneficial to find feasible sets of tubes (Baykal, Bowen, and Alterovitz, 2018; Baykal, Torres, and Alterovitz, 2015; Bergeles and P. E. Dupont, 2013; Kuntz, Torres, et al., 2015; Torres and Alterovitz, 2011). One of the key aspects that would advance the optimization procedure, is the incorporation of an inverse kinematic approach (that still requires intensive research) to determine the reachability of the manipulation site.

In conclusion, this is the first work that presents a design optimization framework that helps to identify the key parameters, objectives, and constraints to solve the structural design problem of CTCR for various applications. It considers the overall parameter space, conflicting objectives, and external forces for the first time. Specifically, the applicability of a multi-objective particle swarm optimization algorithm is

investigated. The algorithm is successfully applied to three problems and has the potential to be utilized for other scenarios. Additionally, the methodology can handle different patient datasets. This work can be a future guideline for engineers to cope with multi-objective design problems of CTCR.

BIBLIOGRAPHY

Altrogge, I., T. Kröger, T. Preusser, C. Büskens, P. L. Pereira, D. Schmidt, A. Weihusen, and P. Heinz-Otto (2006). "Towards Optimization of Probe Placement for Radio-Frequency Ablation." In: *Lecture Notes in Computer Science* 9.1, pp. 486–493.

Alvarez-Benitez, J. E., R. M. Everson, and J. E. Fieldsend (2005). "A MOPSO Algorithm Based Exclusively on Pareto Dominance Concepts." In: *Springer-Verlag Berlin Heidelberg*, pp. 459–473.

Amanov, E., T.-D. Nguyen, and J. Burgner-Kahrs (2015). "Additive Manufacturing of Patient-Specific Tubular Continuum Manipulators." In: *Medical Imaging: Image-Guided Procedures, Robotic Interventions, and Modeling*. Vol. 9415, 94151P.

Anor, T., J. R. Madsen, and P. Dupont (2011). "Algorithms for Design of Continuum Robots Using the Concentric Tubes Approach: A Neurosurgical Example." In: *IEEE International Conference on Robotics and Automation*, pp. 667–673.

Antman, S. S. (2005). *Nonlinear problems in elasticity*. Springer Science & Business Media, Inc.

Antoniou, A. and W.-S. Lu (2007). *Practical Optimization*. Springer Science & Business Media, Inc.

Audigier, C. et al. (2017). "Comprehensive Preclinical Evaluation of a Multi-physics Model of Liver Tumor Radiofrequency Ablation." In: *International Journal of Computer Assisted Radiology and Surgery* 12.9, pp. 1543–1559.

Awad, M. and R. Khanna (2015). *Efficient Learning Machines*. Apress.

Azimian, H., P. Francis, T. Looi, and J. Drake (2014). "Structurally Redesigned Concentric Tube Manipulators with Improved Stability." In: *IEEE International Conference on Intelligent Robots and Systems*, pp. 2030–2035.

Baegert, C., C. Villard, P. Schreck, L. Soler, and A. Gangi (2007). "Trajectory optimization for the planning of percutaneous radiofrequency ablation on hepatic tumors." In: *Computer Aided Surgery* 12.2, pp. 82–90.

Bajo, A., R. E. Goldman, L. Wang, D. Fowler, and N. Simaan (2012). "Integration and Preliminary Evaluation of an Insertable Robotic Effectors Platform for Single Port Access Surgery." In: *IEEE International Conference on Robotics and Automation*, pp. 3381–3387.

Baykal, C., C. Bowen, and R. Alterovitz (2018). "Asymptotically optimal kinematic design of robots using motion planning." In: *Autonomous Robots* 43.2, pp. 345–357.

Baykal, C., L. G. Torres, and R. Alterovitz (2015). "Optimizing Design Parameters for Sets of Concentric Tube Robots using Sampling-based Motion Planning." In: *IEEE International Conference on Intelligent Robots and Systems*, pp. 4381–4387.

Bedell, C., J. Lock, A. Gosline, and P. E. Dupont (2011). "Design Optimization of Concentric Tube Robots Based on Task and Anatomical Constraints." In: *IEEE International Conference on Robotics and Automation*, pp. 398–403.

Bergeles, C. and P. E. Dupont (2013). "Planning Stable Paths for Concentric Tube Robots." In: *IEEE International Conference on Intelligent Robots and Systems*, pp. 3077–3082.

Bergeles, C., A. H. Gosline, N. V. Vasilyev, P. J. Codd, P. J. del Nido, and P. E. Dupont (2015). "Concentric Tube Robot Design and Optimization Based on Task and Anatomical Constraints." In: *IEEE Transactions on Robotics* 31.1, pp. 67–84. DOI: 10.1109/TRO.2014.2378431.

Bodily, D. M., T. F. Allen, and M. D. Killpack (2017). "Multi-Objective Design Optimization of a Soft, Pneumatic Robot." In: *IEEE International Conference on Robotics and Automation*, pp. 1864–1871. DOI: 10.1109/ICRA.2017.7989218.

Boushaki, M., C. Liu, B. Herman, V. Trevillot, M. Akkari, and P. Poignet (2016). "Optimization of Concentric-Tube Robot Design for Deep Anterior Brain Tumor Surgery." In: *International Conference on Control, Automation, Robotics & Vision*, pp. 1–6.

Burdette, E. C., D. C. Rucker, P. Prakash, C. J. Diederich, J. M. Croom, C. Clarke, P. Stolka, T. Juang, E. M. Boctor, and R. J. Webster III (2010). "The ACUSITT Ultrasonic Ablator: The First Steerable Needle with an Integrated Interventional Tool." In: *Proceedings of SPIE - The International Society for Optical Engineering 7629*, pp. 1–10.

Burgner-Kahrs, J., H. B. Gilbert, J. Granna, P. J. Swaney, and R. J. Webster III (2014). "Workspace Characterization for Concentric Tube Continuum Robots." In: *IEEE/RSJ International Conference on Intelligent Robots and Systems*, pp. 1269–1275.

Burgner-Kahrs, J., D. C. Rucker, and H. Choset (2015). "Continuum Robots for Medical Applications: A Survey." In: *IEEE Transactions on Robotics* 31.6, pp. 1261–1280.

Burgner, J., H. B. Gilbert, and R. J. Webster III (2013). "On the Computational Design of Concentric Tube Robots: Incorporating Volume-Based Objectives." In: *IEEE International Conference on Robotics and Automation*, pp. 1193–1198.

Burgner, J., D. C. Rucker, H. B. Gilbert, P. J. Swaney, P. T. Russell, K. D. Weaver, and R. J. Webster III (2014). "A Telerobotic System for Transnasal Surgery." In: *IEEE/ASME Transactions on Mechatronics* 9.3, pp. 996–1006.

Burgner, J., P. J. Swaney, R. A. Lathrop, K. D. Weaver, and R. J. Webster III (2013). "Debulking From Within: A Robotic Steerable Cannula for Intracerebral Hemorrhage Evacuation." In: *IEEE Transactions on Biomedical Engineering* 60.9, pp. 2567–2575.

Burgner, J., P. J. Swaney, D. C. Rucker, H. B. Gilbert, S. T. Nill, P. T. Russell, K. D. Weaver, and R. J. Webster III (2011). "A Bimanual Teleoperated System for Endonasal Skull Base Surgery." In: *IEEE/RSJ International Conference on Intelligent Robots and Systems*, pp. 2517–2523.

Chen, C.-C. R., M. I. Miga, and R. L. Galloway (2009). "Optimizing Electrode Placement Using Finite-Element Models in Radiofrequency Ablation Treatment Planning." In: *IEEE Transactions on Biomedical Engineering* 56.2, pp. 237–245.

Chirikjian, G. S. and J. W. Burdick (1994). "A Hyper-Redundant Manipulator." In: *IEEE Robotics and Automation Magazine* 1.4, pp. 22–29.

Chocron, O. (2008). "Evolutionary Design of Modular Robotic Arms." In: *Robotica* 26.3, pp. 323–330.

Chow, C.-k. and H.-t. Tsui (2004). "Autonomous Agent Response Learning by a Multi-Species Particle Swarm Optimization." In: *Congress on Evolutionary Computation*, pp. 778–785.

Ciocarlie, M. and P. Allen (2010). "Data-driven optimization for underactuated robotic hands." In: *IEEE International Conference on Robotics and Automation*, pp. 1292–1299.

Coello Coello, C. A., A. D. Christiansen, and A. Aguirre Hernándes (1998). "Using a new GA-based multiobjective optimization technique for the design of robot arms." In: *Robotica* 16.4, pp. 401–414.

Coello Coello, C. A. and M. Lechuga Salazar (2002). "MOPSO: A Proposal for Multiple Objective Particle Swarm." In: *Congress on Evolutionary Computation*, pp. 1051–1056.

Coello Coello, C. A., G. Toscano Pulido, and M. Salazar Lechuga (2004). "Handling Multiple Objectives With Particle Swarm Optimization." In: *IEEE Transactions on Evolutionary Computation* 8.3, pp. 256–279.

Comber, D. B., J. E. Slightam, V. R. Gervasi, J. S. Neimat, and E. J. Barth (2016). "Design, Additive Manufacture, and Control of a Pneumatic MR-Compatible Needle Driver." In: *IEEE Transactions on Robotics* 32.1, pp. 138–149.

Connolly, F., C. J. Walsh, and K. Bertoldi (2017). "Automatic design of fiber-reinforced soft actuators for trajectory matching." In: *National Academy of Sciences* 114.1, pp. 51–56.

Datta, R., S. Pradhan, and B. Bhattacharya (2016). "Analysis and Design Optimization of a Robotic Gripper Using Multiobjective Genetic Algorithm." In: *IEEE Transactions on Systems, Man, and Cybernetics: Systems* 46.1, pp. 16–26. DOI: 10.1109/TSMC.2015.2437847.

Deb, K., A. Pratap, S. Agarwal, and T. Meyarivan (2002). "A Fast and Elitist Multiobjective Genetic Algorithm: NSGA-II." In: *IEEE Transactions on Evolutionary Computation* 6.2, pp. 182–197.

Delorme, M., M. Iori, and S. Martello (2015). "Bin packing and cutting stock problems: Mathematical models and exact algorithms." In: *European Journal of Operational Research* 255.1, pp. 1–20.

Eiben, A. E. and J. E. Smith (2003). *Introduction to Evolutionary Algorithms*. Springer-Verlag Berlin Heidelberg.

Fellmann, C. and J. Burgner-Kahrs (2015). "Implications of Trajectory Generation Strategies for Tubular Continuum Robots." In: *IEEE International Conference on Intelligent Robots and Systems*, pp. 202–208.

Fleming, P. J., R. C. Purshouse, and R. J. Lygoe (2005). "Many-Objective Optimization: An Engineering Design Perspective." In: *Evolutionary Multi-Criterion Optimization: Third International Conference Proceedings*, pp. 14–32.

Fogel, L. J., A. J. Owens, and M. J. Walsh (1966). *Artificial Intelligence through Simulated Evolution*. John Wiley & Sons, Inc.

Gilbert, H. B., R. J. Hendrick, and R. J. Webster III (2016). "Elastic Stability of Concentric Tube Robots: A Stability Measure and Design Test." In: *IEEE Transactions on Robotics* 32.1, pp. 20–35.

Gilbert, H. B., J. Neimat, and R. J. Webster III (2015). "Concentric Tube Robots as Steerable Needles: Achieving Follow-the-Leader Deployment." In: *IEEE Transactions on Robotics* 31.2, pp. 246–258. DOI: 10.1109/TRO.2015.2394331.

Gilbert, H. B., D. C. Rucker, and R. J. Webster III (2016). "Concentric Tube Robots: The State of the Art and Future Directions." In: *Robotics Research. Springer Tracts in Advanced Robotics* 114, pp. 253–269.

Godage, I. S., A. A. Remirez, R. Wirz, K. D. Weaver, J. Burgner-Kahrs, and R. J. Webster III (2015). "Robotic Intracerebral Hemorrhage Evacuation: An In-Scanner Approach with Concentric Tube Robots." In: *IEEE/RSJ International Conference on Intelligent Robots and Systems*, pp. 1447–1452.

Goldberg, D. E. (1989). *Genetic Algorithms in Search, Optimization & Machine Learning*. Addison-Wesley Publishing Company, Inc.

Goldberg, D. E. and J. H. Holland (1988). "Genetic Algorithms and Machine Learning." In: *Machine Learning* 3.2, pp. 95–99.

Granna, J. and J. Burgner (2014). "Characterizing the Workspace of Concentric Tube Continuum Robots." In: *International Symposium on Robotics*, pp. 11–17.

Granna, J., T. S. Rau, T.-D. Nguyen, T. Lenarz, O. Majdani, and J. Burgner-Kahrs (2016). "Toward automated cochlear implant insertion using tubular manipulators." In: *SPIE 9786, Medical Imaging 2016: Image-Guided Procedures, Robotic Interventions, and Modeling*, 97861F.

Granna, J., A. Nabavi, and J. Burgner-Kahrs (2018). "Computer-assisted planning for a concentric tube robotic system in neurosurgery." In: *International Journal of Computer Assisted Radiology and Surgery* 14.2, pp. 335–344. URL: https://doi.org/10.1007/s11548-018-1890-8.

Grassmann, R., V. Modes, and J. Burgner-Kahrs (2018). "Learning the Forward and Inverse Kinematics of a 6-DOF Concentric Tube Continuum Robot in SE(3)." In: *IEEE International Conference on Intelligent Robots and Systems*, pp. 5125–5132.

Graves, C., A. Slocum, R. Gupta, and C. J. Walsh (2012). "Towards a Compact Robotically Steerable Thermal Ablation Probe." In: *IEEE International Conference on Robotics and Automation*, pp. 709–714.

Ha, J., F. C. Park, and P. E. Dupont (2016). "Elastic Stability of Concentric Tube Robots Subject to External Loads." In: *IEEE Transactions on Biomedical Engineering* 63.6, pp. 1116–1128.

Ha, J., F. C. Park, and P. E. Dupont (2017). "Optimizing Tube Precurvature to Enhance the Elastic Stability of Concentric Tube Robots." In: *IEEE Transactions on Robotics* 33.1, pp. 22–37.

Hao, F. and J. P. Merlet (2005). "Multi-criteria optimal design of parallel manipulators based on interval analysis." In: *Mechanism and Machine Theory* 40.2, pp. 157–171. URL: https://doi.org/10.1016/j.mechmachtheory.2004.07.002.

Hassan, R., B. Cohanim, O. de Weck, and G. Venter (2005). *A Comparison of Particle Swarm Optimization and the Genetic Algorithm*, pp. 1–13.

Hendrick, R. J., H. B. Gilbert, and R. J. Webster III (2015a). "Designing Snap-Free Concentric Tube Robots: A Local Bifurcation Approach." In: *IEEE International Conference on Robotics and Automation*, pp. 2256–2263.

Hendrick, R. J., H. B. Gilbert, and R. J. Webster III (2015b). "Designing Snap-Free Concentric Tube Robots: A Local Bifurcation Approach." In: *IEEE/RSJ International Conference on Robotics and Automation*, pp. 2256–2263.

Hendrick, R. J., S. D. Herrell, C. R. Mitchell, and R. J. Webster III (2016). "Experiments on the Simultaneous Hand-Held Control of Rigid Endoscopes and Robots Passing Through Them." In: *Springer International Publishing* 109, pp. 73–87.

Hendrick, R. J., S. D. Herrell, and R. J. Webster III (2014). "A Multi-Arm Hand-Held Robotic System for Transurethral Laser Prostate Surgery." In: *IEEE International Conference on Robotics and Automation*, pp. 2850–2855.

Hendrick, R. J., C. R. Mitchell, S. D. Herrell, and R. J. Webster III (2015). "Hand-held transendoscopic robotic manipulators: A transurethral laser prostate surgery case study." In: *The International Journal of Robotics Research* 34.13, pp. 1559–1572.

Hiller, J. and H. Lipson (2012). "Automatic Design and Manufacture of Soft Robots." In: *IEEE Transactions on Robotics* 28.2, pp. 457–466.

Holland, J. H. (1962). "Outline for a Logical Theory of Adaptive Systems." In: *Journal of the ACM* 9.3, pp. 297–314.

Huang, W. (2002). "On the selection of shape memory alloys for actuators." In: *Materials & Design* 23.1, pp. 11–19.

Jamwal, P. K., S. Xie, and K. C. Aw (2009). "Kinematic design optimization of a parallel ankle rehabilitation robot using modified genetic algorithm." In: *Robotics and Autonomous Systems* 57.10, pp. 1018–1027. URL: https://doi.org/10.1016/j.robot.2009.07.017.

Jani, J. M., M. Leary, A. Subic, and M. A. Gibson (2014). "A review of shape memory alloy research, applications and opportunities." In: *Materials and Design* 56.1, pp. 1078–1113.

Kadlec, P. and V. Šeděnka (2018). "Particle swarm optimization for problems with variable number of dimensions." In: *Engineering Optimization* 50.3, pp. 382–399.

Kapoor, A., M. Li, and B. Wood (2011). "Mixed variable optimization for radio frequency ablation planning." In: *Proc. SPIE 7964, Medical Imaging 2011: Visualization, Image-Guided Procedures, and Modeling*. 796420, pp. 1–7.

Kelaiaia, R., O. Company, and A. Zaatri (2012). "Multiobjective optimization of a linear Delta parallel robot." In: *Mechanism and Machine Theory* 50.2012, pp. 159–178.

Kennedy, J. and R. C. Eberhart (1995). "Particle Swarm Optimization." In: *IEEE International Conference on Neural Networks*, pp. 1942–1948.

Khatami, S. and F. Sassani (2002). "Isotropic Design Optimization of Robotic Manipulators Using a Genetic Algorithm Method." In: *IEEE International Symposium on Intelligent Control*, pp. 562–567.

Kim, B., J. Ha, F. C. Park, and P. E. Dupont (2014). "Optimizing Curvature Sensor Placement for Fast, Accurate Shape Sensing of Continuum Robots." In: *IEEE International Conference on Robotics and Automation*, pp. 5374–5379.

Kim, H. S. and L.-W. Tsai (2003). "Design Optimization of a Cartesian Parallel Manipulator." In: *Journal of Mechanical Design* 125.1, p. 43.

Kim, J. S., D. Y. Lee, K. Kim, S. Kang, and K. J. Cho (2014). "Toward a Solution to the Snapping Problem in a Concentric-Tube Continuum Robot: Grooved Tubes with

Anisotropy." In: *IEEE International Conference on Robotics and Automation*. IEEE, pp. 5871–5876.

Kim, U., D. H. Lee, W. J. Yoon, B. Hannaford, and H. R. Choi (2015). "Force Sensor Integrated Surgical Forceps for Minimally Invasive Robotic Surgery." In: *IEEE Transactions on Robotics* 31.5, pp. 1214–1224.

Kumar, V., S. Sen, S. S. Roy, C. Har, and S. N. Shome (2014). "Design Optimization of Serial Link Redundant Manipulator: An Approach Using Global Performance Metric." In: *Procedia Technology* 14, pp. 43–50.

Kuntz, A., C. Bowen, C. Baykal, A. W. Mahoney, P. L. Anderson, F. Maldonado, R. J. Webster III, and R. Alterovitz (2018). "Kinematic Design Optimization of a Parallel Surgical Robot to Maximize Anatomical Visibility via Motion Planning." In: *IEEE International Conference on Robotics and Automation*, pp. 926–933.

Kuntz, A., L. G. Torres, R. H. Feins, R. J. Webster III, and R. Alterovitz (2015). "Motion Planning for a Three-Stage Multilumen Transoral Lung Access System." In: *IEEE/RSJ International Conference on Intelligent Robots and Systems*, pp. 3255–3261.

Kurtz, R. and V. Hayward (1992). "Multiple-Goal Kinematic Optimization of a Parallel Spherical Mechanism with Actuator Redundancy." In: *IEEE Transactions on Robotics and Automation* 8.5, pp. 644–651.

Lee, T.-C. and R. Kashyap (1994). "Building Skeleton Models via 3D Medical Surface/Axis Thinning Algorithms." In: *Graphical Models and Image Processing* 56.6, pp. 462–478.

Lee, D. Y., J. Kim, J. S. Kim, C. Baek, G. Noh, D. N. Kim, K. Kim, S. Kang, and K. J. Cho (2015). "Anisotropic Patterning to Reduce Instability of Concentric-Tube Robots." In: *IEEE Transactions on Robotics* 31.6, pp. 1311–1323.

Leibrandt, K., C. Bergeles, and G.-Z. Yang (2015). "On-Line Collision-Free Inverse Kinematics with Frictional Active Constraints for Effective Control of Unstable Concentric Tube Robots." In: *IEEE International Conference on Intelligent Robots and Systems*, pp. 3797–3804.

Leibrandt, K., C. Bergeles, and G.-Z. Yang (2017). "Implicit Active Constraints for Concentric Tube Robots Based on Analysis of the Safe and Dexterous Workspace." In: *IEEE International Conference on Intelligent Robots and Systems*, pp. 193–200.

Li, G., H. Su, G. A. Cole, W. Shang, K. Harrington, A. Camilo, J. G. Pilitsis, and G. S. Fischer (2015). "Robotic System for MRI-Guided Stereotactic Neurosurgery." In: *IEEE Transactions on Biomedical Engineering* 62.4, pp. 1077–1088.

Lock, J., G. Laing, M. Mahvash, and P. E. Dupont (2010). "Quasistatic Modeling of Concentric Tube Robots with External Loads." In: *IEEE/RSJ International Conference on Intelligent Robots and Systems*, pp. 2325–2332.

Lou, Y., Y. Zhang, R. Huang, X. Chen, and Z. Li (2014). "Optimization Algorithms for Kinematically Optimal Design of Parallel Manipulators." In: *IEEE Transactions on Automation Science and Engineering* 11.2, pp. 574–584.

McCreedy, E. S., R. Cheng, P. F. Hemler, A. Viswanathan, B. J. Wood, and M. J. McAuliffe (2006). "Radio Frequency Ablation Registration, Segmentation, and Fusion Tool." In: *IEEE Transactions on Information Technology in Biomedicine* 10.3, pp. 490–496.

Mensel, B., C. Weigel, and N. Hosten (2006). "Laser-Induced Thermotherapy." In: *Recent Results in Cancer Research* 167, pp. 69–75.

Moore, J. and R. Chapman (1999). "Application Of Particle Swarm To Multiobjective Optimization Jacqueline." In: *Department of Computer Science and Software Engineering Department, Auburn University*, pp. 1–4.

Morimoto, T. K. and A. M. Okamura (2016). "Design of 3-D Printed Concentric Tube Robots." In: *IEEE Transactions on Robotics* 32.6, pp. 1419–1430.

Motkoski, J. W., F. W. Yang, S. H. H. Lwu, and G. R. Sutherland (2013). "Toward Robot-Assisted Neurosurgical Lasers." In: *Transactions on Biomedical Engineering* 60.4, pp. 892–898.

Mukhopadhyay, A. and M. Mandal (2014). "Identifying Non-Redundant Gene Markers from Microarray Data: A Multiobjective Variable Length PSO-Based Approach." In: *IEEE Transactions on Computational Biology and Bioinformatics* 11.6, pp. 1545–5963.

Nelles, O. (2001). *Nonlinear System Identification*. Springer-Verlag Berlin Heidelberg.

Noh, G., S. Y. Yoon, S. Yoon, K. Kim, W. Lee, S. Kang, and D. Lee (2016). "Expeditious Design Optimization of a Concentric Tube Robot with a Heat-shrink Plastic Tube." In: *IEEE International Conference on Intelligent Robots and Systems*, pp. 3671–3676.

Ouyang, B., Y. Liu, and D. Sun (2016). "Design and Shape Control of a Three-section Continuum Robot." In: *IEEE/ASME International Conference on Advanced Intelligent Mechatronics, AIM*, pp. 1151–1156. DOI: 10.1109/AIM.2016.7576925.

Paredis, C. J. J. and P. K. Khosla (1993). "Kinematic Design of Serial Link Manipulators From Task Specifications." In: *The International Journal of Robotics Research* 12.3, pp. 274–287.

Pareto, V. (1896). *Cours D'Économie Politique*. Vol. I and II.

Parsopoulos, K. E., D. K. Tasoulis, and M. N. Vrahatis (2004). "Multiobjective Optimization Using Parallel Vector Evaluated Particle Swarm Optimization." In: *International Conference on Artificial Intelligence and Applications*, pp. 823–828.

Parsopoulos, K. E. and M. N. Vrahatis (2002). "Particle Swarm Optimization Method in Multiobjective Problems." In: *ACM Symposium on Applied Computing*, pp. 603–607.

Parsopoulos, K. E. and M. N. Vrahatis (2005). "Unified Particle Swarm Optimization for Solving Constrained Engineering Optimization Problems." In: *Advances in Natural Computation* 3612, pp. 582–591.

Ramezan Shirazi, A., M. M. Seyyed Fakhrabadi, and A. Ghanbari (2014). "Analysis and optimization of the 5-RPUR parallel manipulator." In: *Advanced Robotics* 28.15, pp. 1021–1031.

Rao, R. V. and G. Waghmare (2015). "Design optimization of robot grippers using teaching-learning-based optimization algorithm." In: *Advanced Robotics* 29.6, pp. 431–447.

Rechenberg, I. (1973). *Evolutionsstrategie - Optimierung technischer Systeme nach Prinzipien der biologischen Evolution*.

Ren, H., E. Campos-Nanez, Z. Yaniv, F. Banovac, H. Abeledo, N. Hata, and K. Cleary (2014). "Treatment Planning and Image Guidance for Radiofrequency Ablation of Large Tumors." In: *IEEE Journal of Biomedical and Health Informatics* 18.3, pp. 920–928.

Ren, H., W. Guo, S. S. Ge, and W. Lim (2014). "Coverage planning in computer-assisted ablation based on Genetic Algorithm." In: *Computers in Biology and Medicine* 49.1, pp. 36–45.

Reyes-Sierra, M. and C. A. Coello Coello (2006). "Multi-Objective Particle Swarm Optimizers: A Survey of the State-of-the-Art." In: *International Journal of Computational Intelligence Research* 2.3, pp. 287–308.

Rezapour, M., E. C. Leuthardt, and J. L. Gorlewicz (2016). "Design of a Steerable Guide for Laser Interstitial Thermal Therapy of Brain Tumors." In: *Journal of Medical Devices* 10.3, pp. 030909–1–030909–2.

Robinson, G. and J. B. C. Davies (1999). "Continuum Robots - A State of the Art." In: *IEEE International Conference on Robotics and Automation* 4, pp. 2849–2854.

Rucker, D. C., B. A. Jones, and R. J. Webster III (2010a). "A Geometrically Exact Model for Externally Loaded Concentric-Tube Continuum Robots." In: *IEEE Transactions on Robotics* 26.5, pp. 769–780.

Rucker, D. C., B. A. Jones, and R. J. Webster III (2010b). "A Model for Concentric Tube Continuum Robots Under Applied Wrenches." In: *IEEE International Conference on Robotics and Automation*, pp. 1047–1052.

Rucker, D. C. and R. J. Webster III (2008). "Mechanics-Based Modeling of Bending and Torsion in Active Cannulas." In: *IEEE/RAS-EMBS International Conference on Biomedical Robotics and Biomechatronics*, pp. 704–709.

Runge, G., J. Peters, and A. Raatz (2017). "Design Optimization of Soft Pneumatic Actuators Using Genetic Algorithms." In: *IEEE International Conference on Robotics and Biomimetics*, pp. 393–400. DOI: 10.1109/ROBIO.2017.8324449.

Ryu, S. C. and P. E. Dupont (2014). "FBG-based Shape Sensing Tubes for Continuum Robots." In: *IEEE International Conference on Robotics and Automation*, pp. 3531–3537.

Sears, P. and P. Dupont (2006). "A Steerable Needle Technology Using Curved Concentric Tubes." In: *IEEE/RSJ International Conference on Intelligent Robots and Systems*, pp. 2850–2856.

Sears, P. and P. E. Dupont (2007). "Inverse Kinematics of Concentric Tube Steerable Needles." In: *IEEE International Conference on Robotics and Automation*, pp. 1887–1892.

Shi, Y. and R. C. Eberhart (1999). "Empirical Study of Particle Swarm Optimization." In: *Congress on Evolutionary Computation*, pp. 1942–1948.

Shin, H., S. Lee, J. I. Jeong, and J. Kim (2013). "Antagonistic Stiffness Optimization of Redundantly Actuated Parallel Manipulators in a Predefined Workspace." In: *IEEE/ASME Transactions on Mechatronics* 18.3, pp. 1161–1169. DOI: 10.1109/TMECH.2012.2198224.

Siciliano, B. and O. Khatib (2008). *Handbook of Robotics*. Springer-Verlag Berlin Heidelberg.

Simon, D. (2013). *Evolutionary Optimization Algorithms*. John Wiley & Sons, Inc.

Song, Z., H. Huang, X. Yang, and B. Li (2017). "An Integrated Optimization Design with Structural Parameters and Clearance Allocation for A Planar 3-RRR Parallel Robot." In: *IEEE International Conference on Information and Automation*, pp. 569–573.

Srinivas, N. and K. Deb (1994). "Multiobjective Optimization Using Nondo-minated Sorting in Genetic Algorithms." In: *Evolutionary Computation* 2.3, pp. 221–248.

Stocco, L., S. Salcudean, and F. Sassani (1998). "Fast constrained global minimax optimization of robot parameters." In: *Robotica* 16.6, pp. 595–605.

Stock, M. and K. Miller (2003). "Optimal Kinematic Design of Spatial Parallel Manipulators: Application to Linear Delta Robot." In: *Journal of Mechanical Design* 125.2, p. 292.

Su, B., J. Tang, and H. Liao (2015). "Automatic Laser Ablation Control Algorithm for an Novel Endoscopic Laser Ablation End Effector for Precision Neurosurgery." In: *IEEE International Conference on Intelligent Robots and Systems*, pp. 4362–4367.

Swaney, P. J., J. Burgner, T. S. Pheiffer, D. C. Rucker, H. B. Gilbert, J. E. Ondrake, A. L. Simpson, E. C. Burdette, M. I. Miga, and R. J. Webster III (2012). "Tracked 3D Ultrasound Targeting with an Active Cannula." In: *Proceedings of SPIE - The International Society for Optical Engineering 8316*, pp. 1–9.

Tan, K. C., E. F. Khor, and T. H. Lee (2005). *Multiobjective Evolutionary Algorithms and Applications*. Springer-Verlag London.

Tani, S., S. Tatli, N. Hata, X. Garcia-Rojas, O. I. Olubiyi, S. G. Silverman, and J. Tokuda (2016). "Three-dimensional quantitative assessment of ablation margins based on registration of pre- and post-procedural MRI and distance map." In: *International Journal of Computer Assisted Radiology and Surgery* 11.6, pp. 1133–1142.

Tesch, M., J. Schneider, and H. Choset (2013). "Expensive Multiobjective Optimization for Robotics." In: *IEEE International Conference on Robotics and Automation*, pp. 973–980. DOI: 10.1109/ICRA.2013.6630691.

Torres, L. G. and R. Alterovitz (2011). "Motion Planning for Concentric Tube Robots Using Mechanics-based Models." In: *IEEE International Conference on Intelligent Robots and Systems*. IEEE, pp. 5153–5159.

Torres, L. G., R. J. Webster III, and R. Alterovitz (2012). "Task-oriented Design of Concentric Tube Robots using Mechanics-based Models." In: *IEEE International Conference on Intelligent Robots and Systems*, pp. 4449–4455. DOI: 10.1109/IROS.2012.6386041.

Trelea, I. C. (2003). "The particle swarm optimization algorithm: convergence analysis and parameter selection." In: *Information Processing Letters* 85, pp. 317–325.

Trivedi, D., D. Dienno, and C. D. Rahn (2008). "Optimal, Model-Based Design of Soft Robotic Manipulators." In: *Journal of Mechanical Design* 130.9, pp. 091402–1–091402–9. URL: https://doi.org/10.1115/1.2943300.

Unal, R., G. Kiziltas, and V. Patoglu (2008). "Multi-criteria Design Optimization of Parallel Robots." In: *Conference on Robotics, Automation and Mechatronics*, pp. 112–118.

Vandini, A., C. Bergeles, F. Y. Lin, and G.-Z. Yang (2015). "Vision-Based Intraoperative Shape Sensing of Concentric Tube Robots." In: *IEEE International Conference on Intelligent Robots and Systems*, pp. 2603–2610.

Webster III, R. J., A. M. Okamura, and N. J. Cowan (2006). "Toward Active Cannulas: Miniature Snake-Like Surgical Robots." In: *IEEE/RSJ International Conference on Intelligent Robots and Systems*, pp. 2857–2863.

Webster III, R. J., J. M. Romano, and N. J. Cowan (2009). "Mechanics of Precurved-Tube Continuum Robots." In: *IEEE Transactions on Robotics* 25.1, pp. 67–78.

Weicker, K. (2015). *Evolutionäre Algorithmen*. Springer Fachmedien Wiesbaden.

Xu, K., J. Zhao, and M. Fu (2014). "Development of the SJTU Unfoldable Robotic System (SURS) for Single Port Laparoscopy." In: *IEEE/ASME Transactions on Mechatronics* 20.5, pp. 2133–2145.

Xu, R., S. F. Atashzar, and R. V. Patel (2014). "Kinematic Instability in Concentric-tube Robots: Modeling and Analysis." In: *IEEE RAS/EMBS International Conference on Biomedical Robotics and Biomechatronics*. 1, pp. 163–168.

Xu, R., A. Yurkewich, and R. V. Patel (2016). "Curvature, Torsion and Force Sensing in Continuum Robots Using Helically-Wrapped FBG Sensors." In: *IEEE Robotics and Automation Letters* 1.2, pp. 1052–1059.

Xu, S. and Y. Rahmat-Samii (2007). "Boundary Conditions in Particle Swarm Optimization Revisited." In: *IEEE Transactions on Antennas and Propagation* 55.3, pp. 760–765.

Xue, B., X. Ma, H. Wang, J. Gu, and Y. Li (2014). "Improved Variable-Length Particle Swarm Optimization for Structure-Adjustable Extreme Learning Machine." In: *Control and Intelligent Systems* 42.4.

Yao, R., X. Tang, J. Wang, and P. Huang (2010). "Dimensional Optimization Design of the Four-Cable-Driven Parallel Manipulator in FAST." In: *IEEE/ ASME Transactions on Mechatronics* 15.6, pp. 932–941. DOI: 10.1109/TMECH.2009.2035922.

Yu, X. and M. Gen (2010). *Introduction to Evolutionary Algorithms*. Springer-Verlag London.

Zhang, Z., G. Yang, S. H. Yeo, W. B. Lim, and S. K. Mustafa (2010). "Design Optimization of a Cable-Driven Two-DOF Joint Module with a Flexible Backbone." In: *IEEE/ASME International Conference on Advanced Intelligent Mechatronics*, pp. 385–390.

Zitzler, E. (1999). *Evolutionary Algorithms for Multiobjective Optimization: Methods and Applications*. Swiss Federal Institute of Technology Zurich.

Zitzler, E., M. Laumanns, and L. Thiele (2001). "SPEA2: Improving the Strength Pareto Evolutionary Algorithm." In: *Evolutionary Methods for Design, Optimization and Control with Applications to Industrial Problems*, pp. 95–100.

REPRINT PERMISSIONS

Table 7 lists all figures in this work that have been reproduced from third-party publications. Corresponding licenses from the Copyright Clearance Center Inc., if applicable, are provided.

Table 7: Figures reproduced from third-party publications, corresponding publishers, and licenses, if applicable.

Figure	Publication	Publisher	License
1	Gilbert, Neimat, and Webster III, 2015	IEEE	–
11 (left)	Coello Coello, Christiansen, and Aguirre Hernándes, 1998	Cambridge University Press	4716581077030
11 (right)	Datta, Pradhan, and Bhattacharya, 2016	IEEE	–
12 (left)	Shin et al., 2013	IEEE	–
12 (right)	Hao and Merlet, 2005	Elsevier	4702031168520
13 (left)	Yao et al., 2010	IEEE	–
13 (right)	Jamwal, Xie, and Aw, 2009	Elsevier	34702040048022
14 (left)	Trivedi, Dienno, and Rahn, 2008	ASME	1007533-1
14 (middle)	Bodily, Allen, and Killpack, 2017	IEEE	–
14 (right)	Tesch, Schneider, and Choset, 2013	IEEE	–
15 (left)	Runge, Peters, and Raatz, 2017	IEEE	–
15 (right)	Ouyang, Liu, and Sun, 2016	IEEE	–
16 (left)	Torres, Webster III, and Alterovitz, 2012	IEEE	–
16 (middle)	Bergeles, Gosline, et al., 2015	IEEE	–
16 (right)	Gilbert, Neimat, and Webster III, 2015	IEEE	–

Table 8 lists all figures in this work that originated from the listed publication below, with kind permission from the associated publisher.

Table 8: Reproduced figures with kind permission from the associated publisher and corresponding license.

Figure	Publication	Publisher	License
43, 46, 63, 64, 65, 66	Granna, Nabavi, and Burgner-Kahrs, 2018	Springer Nature	4702041391369

CURRICULUM VITAE

PERSONAL DATA

name: Josephine Granna

date of birth: February 7, 1989

place of birth: Hannover, Germany

email address: josephinegranna@gmail.com

WORK EXPERIENCE

since 11/2019   **Postdoctoral Research Assistant**, *Medical Engineering and Discovery Lab, Mechanical Engineering*, Vanderbilt University, TN, USA

03/2015 - 03/2019   **Research Assistant**, *Laboratory for Continuum Robotics, Mechanical Engineering*, Leibniz Universität Hannover, Germany

01/2014 - 04/2014   **Intern**, *Department for Flexible Assembly Concepts*, Daimler AG, Untertürkheim, Germany

12/2010 - 09/2012   **Student Research Assistant**, *Institute for Multiphase Processes*, Leibniz Universität Hannover, Germany

EDUCATION

10/2008 - 02/2015   **Diploma in Mechanical Engineering**, *Dipl.-Ing., Leibniz Universität Hannover*, Germany

06/2008   **Abitur**, *Geschwister-Scholl Gymnasium*, Berenbostel, Germany

AWARDS

10/2017   **KUKA Best Paper Award, 3rd Place**, *Annual Conference of the German Society for Computer- and Robot-Assisted Surgery e.V.*

10/2017   **Travel Award**, *Annual Conference of the German Society for Computer- and Robot-Assisted Surgery e.V.*, Top 30% of the Paper Ranking

07/2017	**Travel Award**, *Graduate Academy Leibniz University of Hannover*, Conference Trip to the Medical Image Computing and Computer Assisted Intervention 2017
09/2016	**Travel Award**, *Annual Conference of the German Society for Computer- and Robot-Assisted Surgery e.V.*, Top 30% of the Paper Ranking
03/2016	**Caroline Herschel Program**, *Leibniz Universität Hannover*, Promotion of Young Scientific Talents
11/2015	**DAAD Travel Award**, *Conference Trip to the SPIE Medical Imaging 2016*
10/2015	**Best Poster Award**, *Workshop: Navigation and Actuation of Flexible Instruments in Medical Applications*, IEEE/RSJ International Conference on Intelligent Robots and Systems 2015
09/2015	**Travel Award**, *Annual Conference of the German Society for Computer- and Robot-Assisted Surgery e.V.*, Top 30% of the Paper Ranking
09/2014	**Finalist Best Application Paper Award (Top 2%)**, *IEEE/RSJ International Conference on Intelligent Robots and Systems* Acceptance Rate: 47%
09/2012	**International Travel Scholarship**, *Dr. Jürgen und Irmgard Ulderup Stiftung*

TEACHING

Lecture Teaching Assistant

| 2016 - 2018 | **Continuum Robotics**, Hands-On Exercise, Leibniz Universität Hannover |
| 2016 - 2018 | **Journal Club Continuum Robotics**, Leibniz Universität Hannover |

INTERNATIONAL EXPERIENCE

| 09/2012 - 03/2013 | **University of California, Berkeley, USA**, *Student Project*, Vehicle Dynamics and Control Laboratory, Prof. Dr. K. Hedrick |
| 09/2005 - 06/2006 | **Clear Lake High School**, Houston, Texas, *Exchange student* |

PUBLICATIONS

Patents

09/2015   DE 102015115525.7, Cochlea Implant Electrode Assembly, Automated Actuation Device and Use of a Tubular Manipulator, T. S. Rau, J. Granna, O. Majdani, J. Burgner-Kahrs

Journal Papers

Granna, J., M. T. Chikhaoui, J. Starke, and J. Burgner-Kahrs (2018). "Towards Motion Coordination Control and Design Optimization for Dual-Arm Concentric Tube Continuum Robots." In: *IEEE Robotics and Automation Letters* 3.3, pp. 1793–1800.

Granna, J., I. S. Godage, R. Wirz, K. D. Weaver, R. J. Webster III, and J. Burgner-Kahrs (2016). "A 3-D Volume Coverage Path Planning Algorithm with Application to Intracerebral Hemorrhage Evacuation." In: *IEEE Robotics and Automation Letters* 1.2, pp. 876–883.

Granna, J., Y. Guo, K. D. Weaver, and J. Burgner-Kahrs (2017). "Comparison of Optimization Algorithms for a Tubular Aspiration Robot for Maximum Coverage in Intracerebral Hemorrhage Evacuation." In: *Journal of Medical Robotics Research* 02.01, pp. 1–9.

Granna, J., A. Nabavi, and J. Burgner-Kahrs (2018). "Computer-Assisted Planning for a Concentric Tube Robotic System in Neurosurgery." In: *International Journal of Computer Assisted Radiology and Surgery* 14.2, pp. 335–344.

Rau, T. S., J. Granna, T. Lenarz, O. Majdani, and J. Burgner-Kahrs (2015). "Tubular Manipulators: A New Concept for Intracochlear Positioning of an Auditory Prosthesis." In: *Current Directions in Biomedical Engineering* 1.1, pp. 515–518.

Conference Papers

Amanov, E., J. Granna, and J. Burgner-Kahrs (2017). "Toward Improving Path Following Motion: Hybrid Continuum Robot Design." In: *IEEE/RSJ International Conference on Robotics and Automation*, pp. 4666–4672.

Bormann, M., J. Granna, F. Imkamp, and J. Burgner-Kahrs (2016). "Initial Feasibility Study for Transurethral Kidney Surgery using a Tubular Continuum Manipulator." In: *Annual Conference of the German Society for Computer- and Robot-Assisted Surgery e.V.,* pp. 81–86.

Burgner-Kahrs, J., H. B. Gilbert, J. Granna, P. J. Swaney, and R. J. Webster III (2014). "Workspace Characterization for Concentric Tube Continuum Robots." In: *IEEE/RSJ International Conference on Intelligent Robots and Systems*, pp. 1269–1275.

Granna, J. and J. Burgner (2014). "Characterizing the Workspace of Concentric Tube Continuum Robots." In: *International Symposium on Robotics*, pp. 11–17.

Granna, J., A. Graf, A. Nabavi, and J. Burgner-Kahrs (2017). "A Manual Actuation System for Laser Induced Thermal Therapy of Malignant Brain Tumors." In: *Annual Conference of the German Society for Computer- and Robot-Assisted Surgery e.V.*, pp. 125–130.

Granna, J., A. Nabavi, and J. Burgner-Kahrs (2017a). "Initial Proof-of-Concept of an Ablation Planning Algorithm for Laser-Induced Interstitial Thermotherapy in the Brain using a Tubular Continuum Robot." In: *Workshop Proceedings C4 Surgical Robots: Compliant, Continuum, Cognitive, and Collaborative, IEEE/RSJ International Conference on Robotics and Automation*.

Granna, J., A. Nabavi, and J. Burgner-Kahrs (2017b). "Toward Computer-Assisted Planning for Interstitial Laser Ablation of Malignant Brain Tumors using a Tubular Continuum Robot." In: *International Conference on Medical Image Computing and Computer Assisted Intervention*. Part II, LNCS 10434, pp. 557–565.

Granna, J., T. S. Rau, and O. Majdani (2015). "Konzept für die Elektrodeninsertion von Cochlea-Implantaten mit tubulären Manipulatoren." In: *Annual Conference of the German Society for Computer- and Robot-Assisted Surgery e.V.*, pp. 299–304.

Granna, J., T. S. Rau, O. Majdani, and J. Burgner-Kahrs (2015). "Toward Concentric Tube Manipulators for Cochlear Implant Positioning." In: *Workshop Proceedings Navigation and Actuation of Flexible Instruments in Medical Applications (NAFIMA), IEEE/RSJ International Conference on Intelligent Robots and Systems*, pp. 22–23.

Granna, J., T. S. Rau, T.-D. Nguyen, T. Lenarz, O. Majdani, and J. Burgner-Kahrs (2016). "Toward Automated Cochlear Implant Insertion using Tubular Manipulators." In: *Proceedings SPIE Medical Imaging*, 97861F.

Granna, J., Y. Vornehm, C. Fellmann, and J. Burgner-Kahrs (2016). "Rapid Motion Planning for Intracerebral Hemorrhage Evacuation using a Tubular Aspiration Robot." In: *DGR Days*.

Guo, Y., J. Granna, K. D. Weaver, R. J. Webster III, and J. Burgner-Kahrs (2015). "Comparison of Optimization Algorithms for a Tubular Aspiration Robot for Maximum Coverage in Intracerebral Hemorrhage Evacuation." In: pp. 11–12.

Imkamp, F., M. Bormann, J. Granna, and J. Burgner-Kahrs (2017). "Tubuläre Kontinuumsmanipulatoren – Erste Schritte für den Einsatz in der retrograden, intrarenalen Chirurgie." In: *Congress of the German Society of Urology e.V.*

Supervised Student Projects

Baumann, F. (2015). "Visual Representation of Kinematic Parameters for Robots." Master's Thesis. Leibniz Universität Hannover.

Bormann, M. (2016). "Concept for a Tubular Continuum Robot for Patient-Individual Transurethral Kidney Surgery." Diploma Thesis. Leibniz Universität Hannover.

Graf, A. (2016). "Design and Construction of a Manual MR-Compatible Actuation Unit for Tubular Continuum Manipulators for Neurosurgical Laser Ablations." Bachelor's Thesis. Leibniz Universität Hannover.

Hakim, S. (2019). "Modeling of a Flexible Endoport with Integrated Working Channels and Stiffening Mechanism." Master's Thesis. Leibniz Universität Hannover.

Hielscher, V. (2017). "Parameter Optimization of a Tendon-Driven Continuum Robot." Master's Thesis. Leibniz Universität Hannover.

Kriebel, B. (2018). "Design of Tubular Continuum Robots for the Application of Precise Forces." Master's Thesis. Leibniz Universität Hannover.

Pankratz, T. (2018). "Analysis of Kinematic Parameters for Cooperating Tubular Continuum Robots." Master's Thesis. Leibniz Universität Hannover.

Rao, P. (2019). "Towards Continuum Robots for Visual Inspections." Master's Thesis. Indian Institute of Technology.

Vornehm, Y. (2016). "Programming and Commissioning of a Robot System for Intracerebral Hemorrhage Evacuation." Project Work. Leibniz Universität Hannover.